

Title of Thesis

Investigation of Different Injection Strategies and Local Mixture
Concentration for Jet-guided Combustion in a Hydrogen Direct
Injection Spark-Ignition Engine

2013, 3

Mithun Kanti Roy

Graduate School of
Natural Science and Technology
(Doctor's Course)
OKAYAMA UNIVERSITY

Investigation of Different Injection Strategies and Local Mixture
Concentration for Jet-guided Combustion in a Hydrogen Direct
Injection Spark-Ignition Engine

by

Mithun Kanti Roy

A dissertation submitted to the Graduate School of Natural Science and
Technology in partial fulfillment of the requirements for the degree of

DOCTOR OF PHILOSOPHY

Major: Mechanical Engineering

Under the supervision of

Professor Dr. Eiji Tomita

Co-supervised by

Professor Dr. Shinichiro Yanase

Professor Dr. Akihiko Horibe

&

Professor Dr. Nobuyuki Kawahara

Graduate School of Natural Science and Technology
Okayama University, Japan

To Whom It May Concern:

This is to certify that the work entitled “Investigation of Different Injection Strategies and Local Mixture Concentration for Jet-guided Combustion in a Hydrogen Direct Injection Spark-Ignition Engine” is carried out by Mithun Kanti Roy in the Division of Industrial Innovation Sciences at Okayama University under my supervision.

Seal of Supervisor

Professor Dr. Eiji Tomita
Division of Industrial Innovation Sciences,
Graduate School of Natural Science and Technology,
Okayama University
JAPAN

Official Seal

Professor Dr. Toshiro Noritsugu
Dean of Graduate School of Natural Science
and Technology,
Okayama University
JAPAN

ABSTARCT

Spark-ignition (SI) hydrogen engines based on direct injection (DI) promise significant advantages in terms of thermal efficiency and power output, and present a means of overcoming problems related to knocking, backfiring, and preignition. A better understanding of the effects of hydrogen jets on the fuel concentration distribution and mixing process in a DISI engine should provide new and useful insights into combustion optimization. The objective of the present work was to gain a deeper comprehension of the characteristics of late-injection hydrogen combustion. An Ar-ion laser beam was used as a light source to visualize the hydrogen jet in a constant-volume chamber. This allowed us to study the structure of the jet in addition to other physical processes resulting from hydrogen gas injection. Combustion experiments were conducted in a single-cylinder SI optical research engine equipped with a DI system. An experimental combustion setup was applied to a fired, jet-guided DISI engine operated at 600 rpm in stratified mode. GDI injector with the jet directed toward the spark plug was used to develop the stratified combustion concept. A high-speed camera synchronized with the spark was focused on a 52-mm-diameter field of view through a window at the bottom of the piston crown. A series of single-shot images captured at different intervals was used to study the time evolution of the flame distribution. Variations in the fuel injection timing relative ignition timing were found to impact the development of the early flame, as well as the flame propagation. This research also employed spark-induced breakdown spectroscopy (SIBS) to measure the local fuel-air concentration in the spark gap at the time of ignition under stratified-charge conditions. GTT 3D-CFD simulations of transient gas injections are used in this thesis to examine various hypotheses and to answer some questions relevant to the use of hydrogen gas in DISI engines. Part of the objectives of this thesis is to also verify the impact of jet injection model and to establish the effects of injection pressure and chamber conditions on the fuel-air mixture formation in hydrogen a DISI engine.

Keywords: Hydrogen Direct-Injection Spark-Ignition Engine; Flame propagation; Spark-induced Breakdown Spectroscopy; Local fuel concentration measurement; Computational Fluids Dynamics.

ACKNOWLEDGEMENTS

I would like to express my sincere gratitude to several people who have contributed to this work. First of all I express my deep gratitude to my supervisor, Professor Dr. Eiji Tomita and co-supervisor Professor Dr. Nobuyuki Kawahara, for their enthusiastic encouragement of this research work, for the possibility to present my work around the globe, and for their trust in me. I would also like to thank Assistant Professor Dr. Kazuya Tsuboi for his valuable inputs work and Isao Yamane for his technical assistance regarding my research.

I would like to acknowledge the contributions of Ministry of Education, Culture, Sports, Science and Technology (MEXT), Japan in providing the financial support for my studies. I also thank Dr. Hidefumi Fujimoto at Mazda Motor Corporation, Japan for the help with the Gas Parcel method.

I thank the members of my Ph.D. jury for the enthusiasm in accepting the task, in particular the members Professor Dr. Shinichiro Yanase (Fluid Dynamics, Okayama University) and Professor Dr. Akihiko Horibe (Heat Transfer Engineering, Okayama University).

My co-workers in this project, Takashi Fujitani and Koshiro Yudai, have provided me with valuable support in many aspect of this work. Their suggestions and advice helped me solved many issues related to this project. I would also like to thank Dr. Ulugbek Azimov (Sr. Lecturer Curtin University, Sarawak, Malaysia) and Md. Tasyrif bin Abdul Rahman (PhD student at Okayama University) for their advice in this project.

Finally, my deepest appreciation goes to my parents and my wife Mridula Roy for their support, understanding, and encouragement throughout my study.

Contents

1	Introduction.....	1
1.1	Motivation	1
1.2	Objectives.....	4
1.3	Thesis outline	5
2	Modern concept for spark ignition IC engine.....	7
2.1	DISI engine	7
2.1.1	Fundamentals, benefits, and shortcomings of DISI engines....	7
2.1.2	Homogeneous and stratified operating regimes.....	8
2.2	Hydrogen engine development.....	9
2.2.1	Difference between hydrogen and hydrocarbon-fuelled engine 12	
2.2.2	Hydrogen mixture formation	14
2.2.2.1	External mixture formation	15
2.2.2.2	Internal mixture formation	16
2.3	Summary	17
3	Hydrogen jet analysis in a vessel.....	18
3.1	Introduction	18
3.2	Literature review on jets.....	18
3.2.1	Turbulent jets and its regions.....	19
3.2.1.1	Incompressible jets	19
3.2.1.2	Compressible jets	21
3.2.2	Comparisons of gaseous jets and sprays.....	23
3.3	Measurement method	24
3.3.1	Constant volume vessel	24
3.3.2	Injector	25
3.3.3	Jet visualization using a high-speed camera.....	25
3.4	Experimental method	26

Contents

3.4.1	Operating conditions.....	27
3.5	Flow visualization of hydrogen jet in a constant vessel.....	27
3.5.1	Effects of injection pressure	28
3.5.2	Jet penetration at different injection pressure	31
3.5.2.1	Penetration measurements method.....	31
3.5.2.2	Jet penetration rate.....	32
3.5.3	Jet cone angle at different injection pressure	33
3.5.3.1	Jet angle measurements method	33
3.5.3.2	Jet cone angle	34
3.6	Summary	35
4	Jet-guided combustion characteristics.....	36
4.1	Introduction	36
4.2	Literature review	36
4.3	Plume Ignition Combustion Concept (PCC).....	39
4.4	Factors that influence ignition.....	40
4.4.1	In-cylinder flow	40
4.4.2	Air-fuel mixture	41
4.5	Experimental method	42
4.5.1	DISI optical engine	42
4.5.2	Combustion chamber geometry	44
4.5.3	Pressure instrumentation.....	44
4.5.4	Average mass flow rate measurement	46
4.5.5	Combustion quality measurement	47
4.5.6	Optical Access	49
4.5.6.1	High-Speed combustion image acquisition.....	49
4.5.7	Operating conditions.....	51
4.6	Experimental results	52

Contents

4.6.1	Effect of injection timing relative to ignition timing	52
4.6.2	Mass fraction burn for different ignition modes	58
4.6.3	Combustion stability measurements	59
4.6.4	Combustion images analysis.....	62
4.7	Summary	65
5	Local fuel concentration measurement.....	66
5.1	Literature review	66
5.2	Background spark ignition physics	69
5.2.1	Phases of a spark discharge	69
5.3	Spark-induced Breakdown Spectroscopy (SIBS)	75
5.4	SIBS experimental set-up.....	77
5.4.1	Spark plug	78
5.4.2	Spectrometer	79
5.4.3	Optical fiber	82
5.5	SIBS calibration	83
5.5.1	Background estimation and subtraction.....	83
5.5.2	Intensity ratio with overall equivalence ratio.....	84
5.6	Local equivalence ration at different ignition timing.....	86
5.7	Summary	89
6	CFD analysis on mixture formation.....	90
6.1	Introduction	90
6.2	Literature reviews.....	90
6.3	GTT-CHEM	91
6.4	Basic Equation.....	93
6.4.1	Gas-Phase.....	93
6.4.2	Droplet	93
6.5	Method of Calculation.....	95
6.6	Gas-Phase solution	97

Contents

6.6.1	Gas Parcel Method.....	98
6.6.2	Wall boundary condition	101
6.6.3	Solution algorithm	101
6.6.4	Modification of GTT code.....	102
6.7	The Computing Mesh.....	103
6.8	Simulation case for constant volume vessel.....	104
6.8.1	Mesh for constant volume vessel.....	104
6.8.2	Grid dependency	105
6.8.3	Jets penetration in a constant volume vessel (non-reactive) 106	
6.8.4	Single jet validation	110
6.9	In-cylinder mixture formation in direct injection hydrogen engine 113	
6.9.1	Computational grid of the engine cylinder	113
6.9.2	Qualitative analysis of mixture formation	115
6.9.2.1	HI injection case.....	116
6.9.2.2	CI injection case	116
6.9.2.3	TI injection case	117
6.9.2.4	ATI injection case.....	117
6.9.3	Predicted local equivalence ratio	124
6.10	Summary	126
7	Conclusions.....	127
8	References.....	130

List of figures

Figure 2.1 Homogeneous and stratified charge-mode in DISI engine.....	11
Figure 2.2 The spray-guided, wall-guided and air-guided combustion system at stratified charge [38].	12
Figure 2.3 Laminar flame velocity for (—) hydrogen, oxygen and nitrogen mixtures [50] and (°, - -) gasoline and air mixtures [35] at room temperature and atmospheric pressure. The dashed line is a least squares fit polynomial. $[O_2]/[O_2 + N_2]$ is the oxygen mole fraction in the ambient.	16
Figure 2.4 Minimum ignition energies of hydrogen–air, methane–air and heptane-air mixtures in relation to equivalence ratio at atmospheric pressure [50]......	16
Figure 2.5 Quenching distances for hydrogen–oxygen-inert gas mixture at atmospheric pressure. [50]	17
Figure 3.1 Transient Jet [25].	23
Figure 3.2 Underexpanded gas jet. [23]	24
Figure 3.3 Constant volume vessel used in hydrogen jet visualization. ..	27
Figure 3.4 Mitsubishi DI injector.....	28
Figure 3.5 Experimental setup for hydrogen jet visualization.	29
Figure 3.6 High-speed direct images of a 3-MPa injection pressure hydrogen jet into three different ambient pressure N ₂ -filled chambers. The recording speed was 25,000 frames/s.	33
Figure 3.7 High-speed direct images of a 5-MPa injection pressure hydrogen jet into three different ambient pressure N ₂ -filled chambers. The recording speed was 25,000 frames/s.	33
Figure 3.8 Ambient entrainment pattern and vortex region.....	34
Figure 3.9 Jet penetration measurement, plot shows pixel intensity along centerline of jet.....	35

List of figures

Figure 3.10 Jet tip penetration for a) an injection pressure of 3 MPa and b) 5 MPa.....	36
Figure 3.11 Jet geometry to determination jet angle.....	37
Figure 3.12 Jet cone angle for a) an injection pressure of 3 MPa and b) 5 MPa	38
Figure 4.1 The influence of spark timing, a) Otto head configuration of the CFR engine , b) indicate efficiency, NO _x vs spark timing.[88].....	40
4.2 Engine performance and emission of a Hydrogen DISI engine.[8] ...	41
Figure 4.3 PCC combustion concepts	42
Figure 4.4 Schematic view of optical engine experimental setup.....	46
Figure 4.5 Geometric relationship between the injector and the spark plug	48
Figure 4.6 Kistler 6052C piezoelectric pressure sensor.....	48
Figure 4.7 Injection duration vs overall equivalence ratio.....	49
Figure 4.8 Viewable area through the piston window	53
Figure 4.9 Photron FASTCAM SA1.1 (12 bit) CMOS type camera.	53
Figure 4.10 Diagrams showing the fuel-injection timing relative to the ignition timing.....	54
Figure 4.11 Time-series combustion images and typical in-cylinder pressure history along with ROHR at different ignition modes. ($\Phi=0.1$)	57
Figure 4.12 Time-series combustion images and typical in-cylinder pressure history along with ROHR at different ignition modes.($\Phi=0.16$)	58
Figure 4.13Time-series combustion images and typical in-cylinder pressure history along with ROHR at different ignition modes.($\Phi=0.22$)	59

List of figures

Figure 4.14 Time-series combustion images and typical in-cylinder pressure history along with ROHR at different ignition modes. ($\Phi=0.28$)	60
Figure 4.15 MFB for different ignition modes under different overall equivalence ratio.	62
Figure 4.16 IMEP at different ignition modes combustion.....	64
Figure 4.17 COV of IMEP at different equivalence ratio.....	64
Figure 4.18 Average flame area at different ignition modes combustion.	66
Figure 4.19 Average flame area and early kernel growth rate (EKG) at an equivalence ratio of 0.22 under different injection modes. The open circle symbols indicate the area growth rates and the solid circle symbols show the double derivative of the flame area with respect to each crank angle (EKG rate).....	67
Figure 5.1 PLIF measurement (a) Experimental Set-up, (b) Local fuel concentration measurement at different injection timing. [54].....	68
Figure 5.2 TLIF Measurement (a) Experimental set-up (b) In-cylinder pressure histories (c) LIF and Flame intensity. [55]	71
Figure 5.3 Hydrogen concentration measurement in a constant vessel using LIBS. [58].....	69
Figure 5.4 Development of an electron avalanche in the direction of the anode. UV radiation emitted by highly excited ions is responsible for the progress of the avalanche origin towards the cathode. Once positive ions are formed close to the cathode, they are accelerated towards it and may liberate electrons from its surface.	73
Figure 5.5 Schematic diagrams of voltage and current of technical ignition systems as functions of discharge time. Typical values are given	

List of figures

in parentheses, circuit parameters responsible for discharge modes are indicate in brackets. [77].....	76
Figure 5.6 Minimum breakdown voltage for 1 mm electrode gap according to Paschen’s law.	77
Figure 5.7 Temporal evolution of spark emission.[65].....	79
Figure 5.8 Schematic view of the optical engine experimental setup with SIBS sensor.	80
Figure 5.9 Construction of a spark plug.....	81
Figure 5.10 Developed fiberoptic spark plug sensor.	82
Figure 5.11 Schematic optical path of the ocean optics USB2000+ spectrometer.	84
Figure 5.12 Guided rays of a step index (SI) optical fiber.....	85
Figure 5.13 Schematic diagram of the background subtraction by the Shirley method.	87
Figure 5.14 Plasma emitted spectra during near-homogeneous combustion at different equivalence ratios.	88
Figure 5.15 Correlation of the atomic line intensity ratio, $H\alpha/O$ with the overall equivalence ratio.	88
Figure 5.16 Correlation of the atomic line intensity ratio, $H\alpha/N$ with the overall equivalence ratio.	89
Figure 5.17 SIBS spectra for different ignition mode combustion	90
Figure 5.18 Local equivalence ratio measured with SIBS and initial combustion duration.....	91
Figure 6.1 GTT-CHEM flow chart	95
Figure 6.2 Coordinate system and control volume	99
Figure 6.3 Comparison of hydrogen jet between experiment and gas parcel method in GTT [104].	102
Figure 6.4 Nozzle interface in computational mesh.....	105

List of figures

Figure 6.5 Correspondence of data file and shape	107
Figure 6.6 3D mesh used in simulating hydrogen jet.....	108
Figure 6.7 Simulated hydrogen mass fraction contours in a constant volume chamber using different grid sizes along with experimental hydrogen jet image	109
Figure 6.8 Mass fraction distribution of a hydrogen gas jet injected into a constant volume chamber filled with nitrogen.....	111
Figure 6.9 Jet velocity vector during injection. (Injection velocity 300 m/s).....	112
Figure 6.10 Comparisons of experimental and numerical results of the hydrogen jet penetration.....	115
Figure 6.11 Comparisons of theoretical and experimental measured penetrations of a hydrogen jet	115
Figure 6.12 Computational grid (58×58×39) of the engine.....	118
Figure 6.13 Hydrogen mass fraction contours on injection planes during HI timing. Where SOI= 355 deg. CA and EOI =374.5 deg. CA. ($\phi=0.22$, $P_{inj}=5\text{MPa}$, $V_{inj}=200\text{m/s}$)	121
Figure 6.14 Hydrogen mass fraction contours on injection planes during CI timing. Where SOI= 350 deg. CA and EOI =369.5 deg. CA. ($\phi=0.22$, $P_{inj}=5\text{MPa}$, $V_{inj}=200\text{m/s}$)	122
Figure 6.15 Hydrogen mass fraction contours on injection planes during TI timing. Where SOI= 340.5 deg. CA and EOI =TDC. ($\phi=0.22$, $P_{inj}=5\text{MPa}$, $V_{inj}=200\text{m/s}$)	123
Figure 6.16 Hydrogen mass fraction contours on injection planes during ATI timing. Where SOI= 335.5 deg. CA and EOI =355 deg. CA. ($\phi=0.22$, $P_{inj}=5\text{MPa}$, $V_{inj}=500\text{ m/s}$)	124
Figure 6.17 Predicted iso-surface of hydrogen mass fraction at HI timing.	125

List of figures

Figure 6.18 Predicted iso-surface of hydrogen mass fraction at CI timing.	125
Figure 6.19 Predicted iso-surface of hydrogen mass fraction at TI timing.	126
Figure 6.20 Predicted iso-surface of hydrogen mass fraction at ATI timing.	126
Figure 6.21 Predicted local equivalence ratio at different ignition modes combustion	125

List of tables

Table 1 Fuel properties for different fuels.....	10
Table 2 Operating condition for constant volume experiments	30
Table 3 Engine specifications.....	46
Table 4 Optical fiber specifications.....	82
Table 5 Equations for ϕ , $\Gamma\phi$ and S_ϕ	98
Table 6 Constant in the k- ϵ model.....	98
Table 7 Condition in constant volume chamber case	107
Table 8 Engine specifications used in simulation.	114

List of symbols and abbreviations

ATI	After tail ignition
BDC	Bottom Dead Center
c	Sonic velocity, m/s
CA	Crank angle
CCD	Charge Couple Device
C_D	Drag coefficient
CFD	Computational Fluid Dynamics
CFR	Cooperative Fuel Research
CI	Compression Ignition
CIP	Cubic Interpolated Pseudo-Particle
CMOS	Complimentary metal-oxide semiconductor
CNG	Compact Natural Gas
COV	Coefficient of variance
Deg.	Degree
DDM	Discrete Droplet Model
DISI	Direct Injection Spark Ignition
GTT	Generalised Tank and Tube
HI	Head ignition
IC	Internal Combustion
k	Turbulence energy
LIBS	Laser Induced Breakdown Spectroscopy
LIRIAM	Late injection, rapid ignition and mixing scheme
mJ	Mili Joule
Ma	Mach Disk
NA	Numerical aperture
ODE	Ordinary differential equations
P	Pressure, MPa
P_{inj}	Injection pressure, MPa
P_{amb}	Ambient pressure, MPa
PCC	Plume Ignition Combustion Concept
PDE	Partial differential equations
PFI	Port Fuel Injection

PLIF	Planar laser-induced fluorescence
Pr	Prandtl number
ROHR	Rate of heat release
R_g	Gas constant
Re	Reynolds number
Sc	Schmidt number
SIBS	Spark Induced Breakdown Spectroscopy
SIMPLE	Semi-Implicit Method for Pressure Linked Equations
SIMPLEC	Semi-Implicit Method for Pressure Linked Equations Consistent
TDC	Top Dead Center
TI	Tail Ignition
T	Temperature, K
t	Time, sec
t_{turb}	Droplet turbulence correlation time
U_e	Nozzle exit velocity, m/s
UV	Ultra violet
V_{inj}	Injection velocity, m/s
Z_p	Jet penetration in experiment, mm
ϕ	Overall equivalence ratio
ϕ_{local}	Local equivalence ratio
γ	Ratio of specific heats
ε	Dissipation rate of turbulent energy
d_o	Orifice diameter
d_e	Equivalent diameter

1 Introduction

1.1 Motivation

Fossil fuels (i.e., petroleum, natural gas and coal), which meet most of the world's energy demand today, are being depleted rapidly. Also, their combustion products are causing global problems, such as the greenhouse effect, ozone layer depletion and pollution, which are posing great danger for our environment, and eventually, for the total life on our planet. Many engineers and scientists agree that the solution to all of these global problems would be to replace the existing fossil fuel system with the clean hydrogen energy system. Hydrogen is a very efficient and clean fuel. Its combustion will produce no greenhouse gases, no ozone layer depleting chemicals, and little pollution. Hydrogen, produced from renewable energy (solar, wind, etc.) sources, would result in a permanent energy system, which would never have to be changed.

Fossil fuels possess very useful properties not shared by non-conventional energy sources that have made them popular during the last century. Unfortunately, fossil fuels are not renewable. In addition, the pollutants emitted by fossil energy systems (e.g. CO, CO₂, C_nH_m, SO_x, NO_x, radioactivity, heavy metals, ashes, etc.) are greater and more damaging than those that might be produced by a renewable based hydrogen energy system [1]. Since the oil crisis of 1973, considerable progress has been made in the search for alternative energy sources. A long-term goal of energy research has been the seek for a method to produce hydrogen fuel economically by splitting water using sunlight as the primary energy source. Much fundamental research remains to be done.

Lowering of worldwide CO₂ emission to reduce the risk of climate change (greenhouse effect) requires a major restructuring of the energy system. The use of hydrogen as an energy carrier is a long-term option to reduce CO₂ emissions. However, at the present time, hydrogen is not competitive with other energy carriers. Global utilization of fossil fuels for energy needs is rapidly resulting in critical environmental problems throughout the world. Energy, economic and political crises, as well as the health of humans, animals and plant life, are all critical concerns. There is an urgent need of implementing the hydrogen technology. A worldwide conversion from fossil fuels to hydrogen would eliminate many of the problems

and their consequences. The production of hydrogen from non-polluting sources is the ideal way [2].

Hydrogen is one of the attractive candidates among the alternative fuels, and its advantages as an engine fuel has been reviewed [3][4][5]. USA, Japan, Germany has taken initiatives to shift towards a hydrogen-based transportation system. Whether hydrogen will be used in combustion engines or fuel cells in the future depends decisively on the extent to which both concepts meet the existing customer requirements with regard to driving performance, procurement and operating costs. It is believed that the utilization of hydrogen as a fuel for transportation is more likely to be expected in internal combustion engines than in fuel cells at least for some decades [6].

The advantages of using hydrogen as the combustion fuel are many. In contrast to the carbon-based fuels, hydrogen combustion does not produce carbon dioxide or any hydrocarbons. Hydrogen combustion in air is relatively clean as it results in only water vapor and traces of nitrogen oxides. Furthermore, hydrogen produced from renewable sources such as electrolysis using the off-peaked electricity generated by wind turbines can, in principle, avoid any carbon-related emissions. The high flame speed and low spark energy can make hydrogen combustion more efficient than the conventional fuels. Besides, it has wide flammability limits and the combustion can occur even in very lean mixtures. Other advantages that help hydrogen as a fuel are the higher auto ignition temperature and high diffusivity. These advantages of hydrogen over other fuels can pave the way to hydrogen-fueled internal combustion engines.

The research on hydrogen engines on ground vehicles can be traced back to 1979 when BMW developed the first generation of hydrogen vehicles powered by a hydrogen engine with a liquid hydrogen tank [7]. The combustion properties of hydrogen are very different from those of gasoline or diesel since it has a wide flammability range and high burning velocity. Its wide flammability range provides smooth engine operation at a very lean mixture with a low NO_x level [8]. In addition, its high burning velocity may contribute to a relatively high thermal efficiency with a shorter combustion period at the ignition timing close to top dead center (TDC) [9]. Experimental research of hydrogen engine combustion has been performed in numerous studies. Das et al. [10] evaluated the potential of using hydrogen for small horsepower spark-ignition (SI) engines and compared hydrogen fueling with compressed

natural gas (CNG). Das [11] determined the performance, emissions, and combustion characteristics of hydrogen-fueled SI and compression-ignition (CI) engines. Li and Karim [12] investigated the onset of knock in a hydrogen-fueled SI engine. Effects of compression ratio, equivalence ratio, and engine speed on the performance and combustion characteristics of a direct-injection SI engine using hydrogen were also investigated by Mohammadi et al. [8]. Moreover, effects of the injector location and nozzle design on the efficiency and emissions of a direct-injection hydrogen engine were studied by Wallner et al. [13].

Advanced hydrogen engine concepts based on DI fuel systems have shown that the performance potential of H₂-DI operation is approximately 17% higher than that of gasoline port injection [5]. Recently direct injection has been shown to significantly reduce or eliminate these combustion anomalies and is currently a primary focus in the development of the hydrogen engine [9]. Takagi et al. [14] proposed a plume ignition combustion concept (PCC) for hydrogen DISI engines in order to reduce NO_x emissions under high engine-load conditions. Hydrogen DI mixture formation techniques have been grouped in a similar manner as DI gasoline engines, and include jet-guided, wall-guided, and air-guided concepts [15]. Similar to the gasoline direct-injection engine, the injection timing strongly influences the ignitability of mixture. A major challenge to the use of H₂-DI is the in-cylinder hydrogen–air mixing. It is critical to understand the physical process of mixing between the injected fuel and the air within the cylinder in order to optimize the overall performance of the direct-injection engine. The high-pressure injector used for the direct-injection engines usually have multiple holes in the nozzle tip in order to provide an even distribution of fuel and promote proper mixing. This results in the formation of multiple underexpanded jets in the cylinder, which interact with each other and with the in-cylinder boundaries to form the fuel-air mixture before combustion. Almost in all cases, fluid fuel injection flow is three-dimensional and turbulent. This flow can be measured and calculated to some limited degree of accuracy using reasonable assumptions. In continuous system whose combustion chamber are usually large, fuel injection may be assumed to be represented by a turbulent free gas jet discharging into surrounding air. In internal combustion engine where fuel injection may be represented by a confined, turbulent wall impinging or swirling two-dimensional gas jet issuing into a thin disk of small finite thickness. Mixture formation in a direct-injection hydrogen engine was studied recently using chemiluminescence imaging [16]. The mixture formation of hydrogen jet was also studied using schlieren visualization by Peterson and Gandhi [17]. On the other hand, due to the difficulty in modeling the complex physical phenomena and the massive

computational need, numerical simulations of direct-injection hydrogen engines are relatively rare. There have been some studies on DI gas engines; however, better knowledge of the basic combustion characteristics is also necessary. Heywood et al. used schlieren images in an optical SI engine to compare the combustion flame thickness and flame propagation speed of hydrogen and propane [18]. However, very little work has been reported on hydrogen optical engines, and there is a need for high-resolution direct combustion images to measure the fuel distribution and flame propagation under a range of operating conditions, and varying parameters, including the injector size, fuel injection timing, ignition timing, and fuel-air equivalence ratio.

1.2 Objectives

Hydrogen DI engines offer a wide range of options for combustion design, such as fuel stratification. The complexity of hydrogen direct-injection operation, however, requires a fundamental knowledge about the in-cylinder processes. An analysis of global data may promote an overall understanding of hydrogen DI combustion. A view inside the phenomena of a hydrogen engine may be acquired by the application of advanced development methods such as optical experimental methods and numerical analysis in terms of three-dimensional Computational Fluid Dynamics (CFD).

The objective of this study is to investigate jet-guided hydrogen combustion using high-speed imaging and consequently, as a second objective of the present work, understanding of mixture formation using SIBS method under different injection conditions. The goal is also to establish a basis for recommendations regarding an optimization of the combustion concept. A need exists for high-resolution direct-combustion images to measure the fuel distribution and flame propagation under a range of operating conditions and varying parameters, including fuel injection timing, ignition timing, and fuel–air equivalence ratio. Therefore, two features are pertinent to the present study. First, high-resolution direct images of spark-ignited combustion are acquired to investigate the effect of fuel-injection timing in terms of the flame propagation and combustion rate. Second, the intensity ratio of the $H\alpha/O$ atomic emission lines is used to obtain quantitative measurements of the local equivalence ratio in the spark gap region. Simultaneously GTT 3D CFD is used to simulate hydrogen injection and compare the mixture formation inside an engine under different injection conditions. The gas parcel

method is used to generate the hydrogen jet. The outlet conditions from the jet model are used as the inlet for the computational domain. A coarse mesh is used to capture the hydrogen jet. The evolution of the hydrogen jet and fuel-air mixing process are modeled using a GTT-CHEM CFD code. In this study, the start of injection timing are varied, and the mixture distribution in the cylinder is analyzed. It is hope that an accurate and efficient computational model can be developed and used as a tool for the design and optimization of direct-injection hydrogen engine to reduce the use of hydrocarbon fuels. The work described in this thesis was conducted at the Heat Power Laboratory, Okayama University by a using constant-volume combustion vessel and a compression-expansion machine. This research facility has been specifically designed to study ignition and combustion characteristics for hydrogen fuels in a direct-injection (DI) Spark-Ignition Engine. The vessel and the compression-expansion machined both allowed full optical access for the visual investigation of jet penetration, mixture formation and flame propagation by using a high-speed CMOS video camera.

1.3 Thesis outline

The thesis outlines the steps taken in resolving the barriers prohibiting the implementation of jet-guided combustion strategy in a Hydrogen Direct Injection Engine. It is critical to understand the physical process of mixing between the injected fuel and the air within the cylinder in order to optimize the overall performance of the direct-injection engine. Among these key factors investigated are the effects of injection pressure, ignition timing with relative to jet injection timing and local fuel concentration measurement at spark plug gap before the initiation of ignition.

Chapter 1 outlines the background and motivation of the current research, the objective of research, and the research methodology. The advantages of using hydrogen as the combustion fuel are many. In contrast to the carbon-based fuels, hydrogen combustion does not produce carbon dioxide or any hydrocarbons. Hydrogen combustion in air is relatively clean as it results in only water vapor and traces of nitrogen oxides. Advanced hydrogen engine concepts based on DI fuel systems have shown that the performance potential of H₂-DI operation is approximately 17% higher than that of gasoline port injection.

Chapter 2 gives the modern concept for hydrogen direct injection spark ignition engine and their prospects and shortcoming. Hydrogen has unique fuel properties relative to typical gasoline and other popular fuels- wide flammability limits: (4-75% by volume– stoichiometric: 66% by volume) allow for hydrogen engines to run under very lean conditions, high flame speed: decreases losses due to non-ideal combustion processes and high octane number: (130) allows for increased efficiency due to a higher compression ratio. The DISI engine can operate fundamentally in two modes: the homogeneous (early injection) and the stratified-charge modes (late injection). Internal mixture formation, or direct injection, can eliminate many of the combustion abnormalities associated with external mixture formation strategies.

Chapter 3 describes the hydrogen jet visualization in a constant volume vessel. An Argon (Ar)-ion laser beam was used as a light source to visualize the hydrogen jet development at the nozzle exit in a constant-volume chamber. This allowed us to study the structure of the jet in addition to other physical processes resulting from hydrogen gas injection.

Chapter 4 describes the combustion characteristics of the hydrogen jets, which can be controlled by varying the fuel injection timing. Four injection timing combustion modes were studied in this experiment.

Chapter 5 measures the local fuel concentration at stratified charge combustion condition using spark-induced breakdown spectroscopy (SIBS) with a fiber-coupled CCD spectrometer. A fiber-optic spark plug sensor was developed for application to practical DISI engine.

Chapter 6 focuses on hydrogen jet injected into a nitrogen ambient which was simulated using gas parcel method in GTT. Moreover, numerical simulations of direct injection of hydrogen and mixture formation in engine case are performed using the GTT CFD solver.

Chapter 7 describes the conclusion arrived in this research work.

2 Modern concept for spark ignition IC engine

2.1 DISI engine

The DISI engine concept has been investigated for many years. Recently, technological advances have made difficult requirements more feasible, such as the control of fuel pressure, fuel injection, and ignition timing. Early results suggested fuel economy gains of 30% were possible for certain conditions [36]. Other benefits also appear promising, such as reduced cold-start emissions by the elimination of wall wetting and increased thermodynamic efficiency by charge cooling during early-injection operation.

2.1.1 Fundamentals, benefits, and shortcomings of DISI engines

Through the charge cooling effect, a DISI engine can attain higher power than a PFI engine from a given displacement. When fuel is injected directly into the engine cylinder as opposed to the intake plenum (PFI engines), the heat of vaporization for the fuel is drawn from the air charge in the cylinder. This reduces the in-cylinder air density, increasing the mass of intake air. This supercharges the engine slightly. The ability to increase the power-to-weight ratio of a four-stroke engine was, historically, a reason to consider direct injection technology. Additionally, the charge cooling effect reduces the knock constraint, allowing an increased thermodynamic efficiency from a higher compression ratio [36].

Recently, the benefit of improved fuel consumption and the potential reduction of certain pollutant emissions renewed interest in DISI engines. Unfortunately, the benefits were overshadowed by the increased amount of other pollutant emissions, high NO_x (nitrogen oxides) and HC (hydrocarbons). The former occurred because of the locally stoichiometric fuel combustion that occurs even in a overall lean stratified fuel charge, and the latter because of piston wall wetting and possible lean quench of the fuel-air mixture.

Unfortunately, any combustion strategy that achieves fuel economy gains by lean operation (thereby eliminating the pumping loss due to throttling) cannot use a conventional catalytic converter, because they cannot draw oxygen away from NO_x in the presence of excess air. Without effective lean-NO_x catalyst technology, DISI engines cannot meet current emission

standards. Storage and purge catalyst methods have achieved moderate success, but they are susceptible to catalyst poisoning from the high sulphur level in gasoline [36]. The emissions issue cannot be resolved until catalytic technology presents a robust strategy to reduce NO_x in the presence of excess air or the fundamental mechanisms of pollutant generation are better understood.

2.1.2 Homogeneous and stratified operating regimes

The DISI engine can operate fundamentally in two modes: one mode associated with high load conditions and the other with light load conditions. These two modes have different mixing requirements for charge preparation. For high load requirements, fuel is injected during the intake stroke and, at the time of spark, the mixture should be well distributed and fairly homogeneous. For light load conditions, fuel is injected late (during the compression stroke), and, at the time of spark, should form a stratified fuel cloud in the region of the spark plug. Therefore, the distribution of the fuel cloud should be consistent with an air-fuel profile such that it ignites rapidly and burns completely. During operation with homogeneous charge the adjustment of engine load is done by throttling while during operation with stratified charge the engine runs with unthrottled conditions and engine load is adjusted by fuel/air-equivalence ratio [37]. Fig. 2.1 shows the homogeneous (early injection) and the stratified-charge modes (late injection). The conflicting requirements of the homogeneous and stratified regimes make the optimization of mixing characteristics a complex issue.

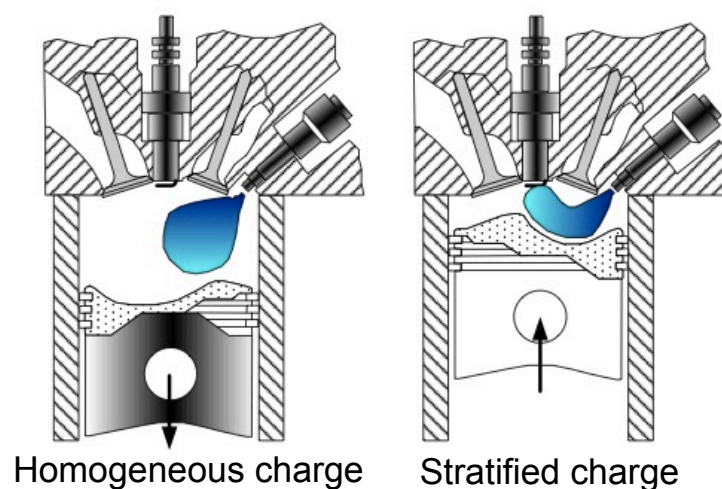


Figure 2.1 Homogeneous and stratified charge-mode in DISI engine.

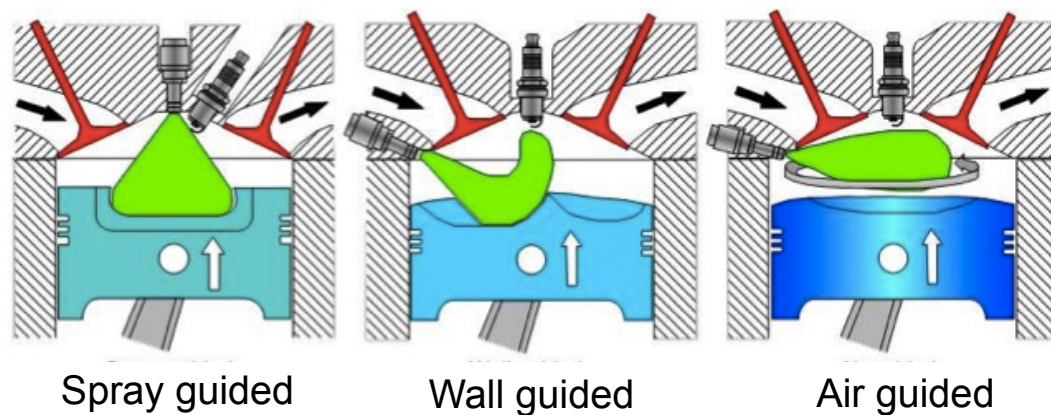


Figure 2.2 The spray-guided, wall-guided and air-guided combustion system at stratified charge [38].

In the stratified operation, three combustion systems are used to form an ignitable mixture near spark plug at the instant ignition. These are the wall-guided, air-guided and spray-guided combustion systems, Fig. 2.2. The distinction between the different concepts are depending on the relative position of the injector with respect to the spark plug and the way the mixture is transported inside the cylinder [39].

2.2 Hydrogen engine development

Internal combustion engine that utilize hydrogen as either a primary or supplementary fuel have been researched and developed extensively over many years; the main attraction being low total emission with absolutely no carbon-related emission. Studies dating back to 1820 by Rv. W Cecil were conducted to examine the properties of hydrogen as an alternative to petroleum-based fuels. In the 1930's thousand of vehicle were modified to run on hydrogen in Europe and during the World Wars hydrogen was seriously studied because of fear of a possible gasoline shortage. By the 1970's, increasing worries of gasoline shortages and initial fears of the effects of carbon-based pollution prompted increase efforts to develop the hydrogen engine [40]. Hydrogen has unique fuel properties relative to typical gasoline and other popular fuels. Table 1 shows the main fuel parameters for various fuels [9][40][41].

Table 1 Fuel properties for different fuels

Parameter	Diesel	Gasoline	Methane	Hydrogen
Density [kg/m ³]	830	730-780	0.72	0.089
Molecular Weight	~170	~110	16.043	2.016
Lower Heating Value [MJ/kg]	42.5	43.5	50	120
Boiling Temperature [C]	180-360	25-215	-162	-253
Ignition Limits [Vol-%]	0.6-5.5	1.0-7.6	5.3-15	4-76
Ignition Limits [λ]	0.5-1.3	0.4-1.4	0.7-2.1	0.2-10
Minimum Ignition Energy [mJ]	0.24	0.24	0.29	0.02
Self-Ignition Temperature [C]	~250	~350	595	585
Diffusion Coefficient [m ² /s]	-	-	1.9x10 ⁻⁶	8.5x10 ⁻⁶
Adiabatic Flame Temp. at Stoich.[C]	2000	1980	1851	2042
Quenching Distance [mm]	-	2	2.03	0.64
Laminar Flame Speed [cm/s]	40-80	40-80	40	200

Some of these fuel characteristics are advantageous for utilization in an engine.

- Wide flammability limits: (4-75% by volume– stoichiometric: 66% by volume) allow for hydrogen engines to run under very lean conditions.
- High flame speed: decreases losses due to non-ideal combustion processes.
- High octane number: (130) allows for increased efficiency due to a higher compression ratio.

While other characteristics present obstacles in the development of the hydrogen engine.

- Low minimum ignition energy: results in backfire and pre-ignition problems. For spark-ignition engines, three regimes of abnormal combustion exist: backfire (premature ignition during the intake stroke, which could be seen as an early form of pre-ignition), pre-ignition (uncontrolled ignition induced by a hot spot, premature to the spark ignition) and knock (auto-ignition of the end gas region). Backfire has been a particularly inflexible difficulty to the development of hydrogen engines. The causes cited for backfire are,
 - Hot spots in the combustion chamber: deposits and particulates, the spark plug, residual gas, exhaust valves etc. because of the low ignition energy of hydrogen and the wide flammability limits [42].

- Residual energy in the ignition circuit: due to the lower ion concentration of a hydrogen/air flame compared to a hydrocarbon/air flame, it is possible that the ignition energy is not completely deposited in the flame and remains in the ignition circuit until the cylinder conditions are such that a second, unwanted, ignition can occur, namely during the expansion or the intake stroke, when the pressure is low [43].
- Combustion in the piston top land persisting up to inlet valve opening time and igniting the fresh charge [44][45]. This is caused by the smaller quenching gap of hydrogen mixtures compared to typical hydrocarbons, which enables a hydrogen flame to propagate into the top land.

Pre-ignition is often encountered in hydrogen engines because of the low ignition energy and wide flammability limits of hydrogen. As a premature ignition causes the mixture to burn mostly during the compression stroke, the temperature in the combustion chamber rises, which causes the hot spot that led to the pre-ignition to increase in temperature, resulting in another, earlier, pre-ignition in the next cycle. This advancement of the pre-ignition continues until it occurs during the intake stroke and causes backfire [45], [46].

The knocking behaviour of hydrogen engines has been misunderstood more than the backfire phenomenon. At very high compression ratios (16 or above for chemically correct mixtures), spark knock may occur. Spark knock is caused by auto-ignition of the end mixture, after this mixture has been compressed and thereby heated as a result of combustion elsewhere in the cylinder, but before it has been reached by the flame front. The severity of spark knock depends on spark timing. There is some evidence that the causes of hydrogen engine knock could be different from gasoline knock, being caused by excessive flame speeds rather than an end-gas reaction [47]. Thus, reducing the rate of pressure rise might be more effective to control knock than limiting the combustion period. It is noteworthy that the experimental and theoretical work of Karim and co-workers [12],[48] reports very wide knocking regions, where stoichiometric mixtures are claimed to knock even at compression ratios as low as 6:1. Reviewing the experimental literature on hydrogen SI engines, pre-ignition seems to be the limiting factor concerning compression ratios, spark timings and mixture equivalence ratios, rather than knock.

- Low energy density: significant volumes of hydrogen are necessary to provide comparable energy levels relative to current fuels.

- High flame temperature: results in higher wall heat losses.

With these advantages and disadvantages, along with others not listed here, engine developers have begun building and testing hydrogen-fueled engines in the hope to provide cleaner more efficient engines and possibly develop a hydrogen infrastructure for future technologies such as the fuel cell[49].

2.2.1 Difference between hydrogen and hydrocarbon-fuelled engine

In the following lines, emphasis will be on the ways in which hydrogen engines are or should be different. The differences arise from properties of hydrogen such as high flame speed, very wide flammability limits, low ignition energy and low heat content per unit volume. Figure 2.3 shows the effects of the high flame speed of hydrogen-air mixtures. The backfiring tendency is enhanced by the low ignition energy of hydrogen (see Fig. 2.4) and by the small quenching distance (Fig. 2.5). It is possible to prevent backfiring by using lean mixtures, by using exhaust gas recirculation, or by using water injection. All of these measures reduce flame speed and increase ignition energy and quench distance. Of course, the entire problem does not arise if the hydrogen is injected directly into the cylinder. The wide flammability limits of hydrogen make it possible to use very lean or very rich mixtures. Flame propagation experiments in a tube yield a lean flammability limit for a mixture at room temperature and 1 atm. pressure of $\phi = 0.10$ for upward propagation of a noncoherent flame and of $\phi = 0.23$ for downward and upward propagation of a coherent flame [50]. The latter limit is the one most applicable to combustion in engines. However, a more practical lean limit for combustion in engines is about 0.30; below this limit, flame speed and hence thermal efficiency drop off drastically (see Fig. 2.3). The rich flammability limit is at $\phi = 7.0$. Rich mixtures are unattractive for engine operation. On the other hand, the use of lean mixtures is very attractive because it leads to high thermal efficiency. In addition, it provides the possibility of controlling the power output of an engine by changing the fuel flow rate, while keeping the airflow unthrottled. This is called “quality regulation,” as opposed to “quantity regulation” provided by throttling, and has the very important advantage of eliminating air-pumping losses.

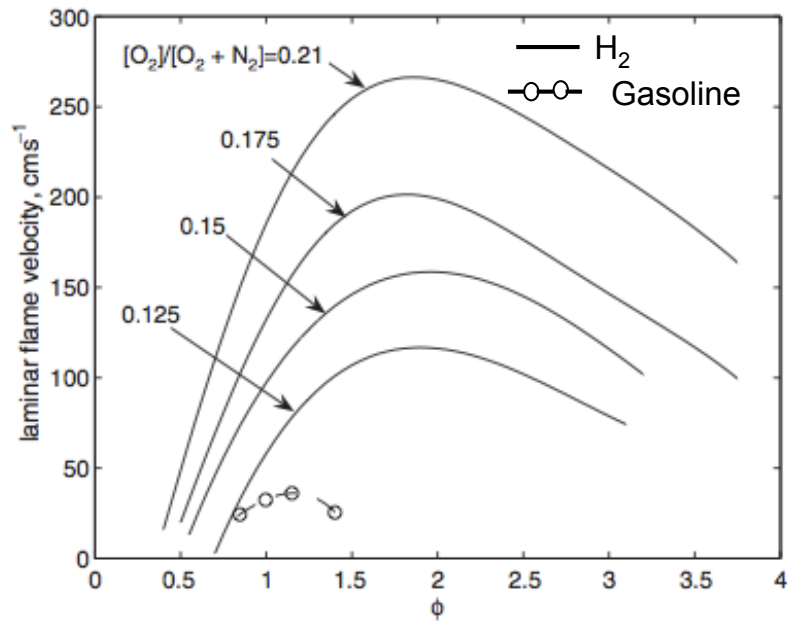


Figure 2.3 Laminar flame velocity for (—) hydrogen, oxygen and nitrogen mixtures [50] and (°, - -) gasoline and air mixtures [35] at room temperature and atmospheric pressure. The dashed line is a least squares fit polynomial. $[\text{O}_2]/[\text{O}_2 + \text{N}_2]$ is the oxygen mole fraction in the ambient.

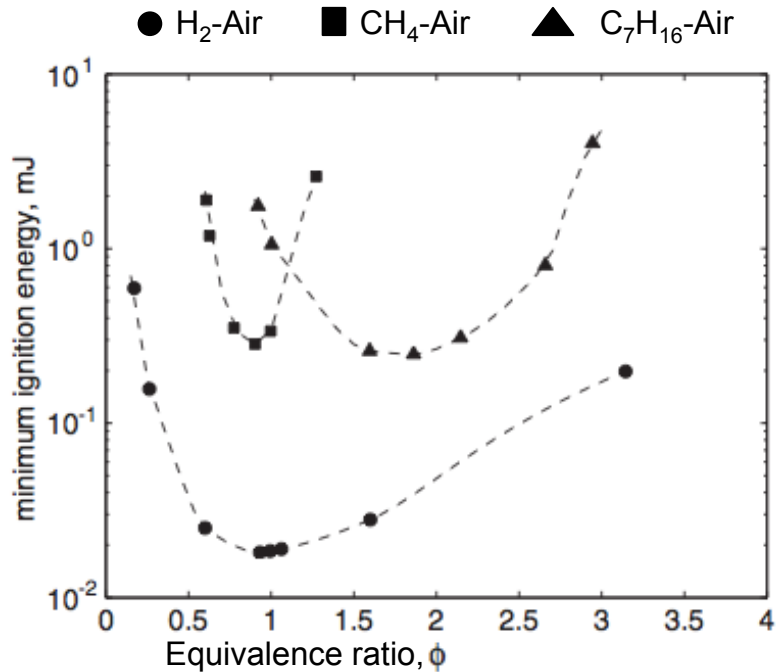


Figure 2.4 Minimum ignition energies of hydrogen-air, methane-air and heptane-air mixtures in relation to equivalence ratio at atmospheric pressure [50].

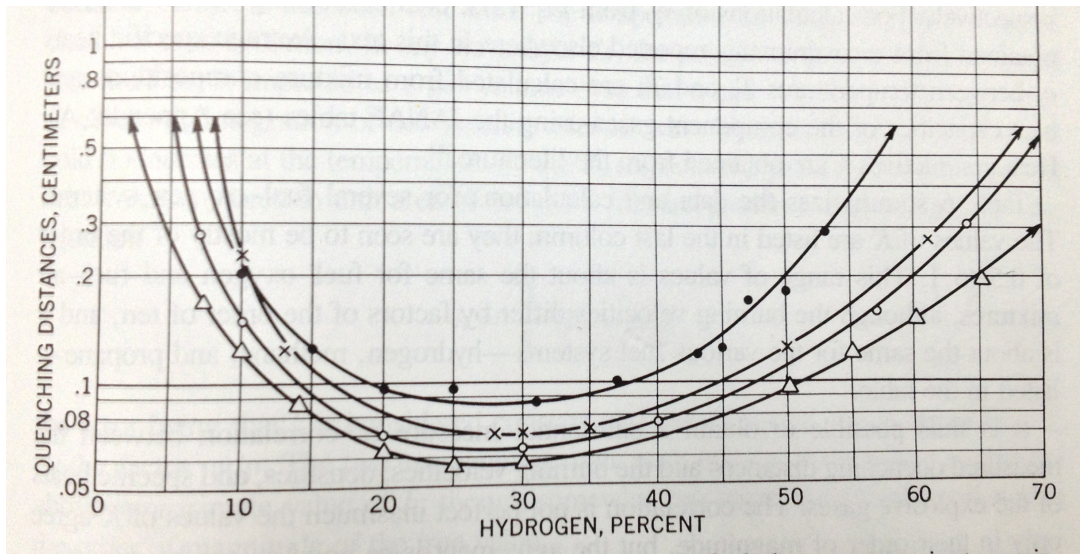


Figure 2.5 Quenching distances for hydrogen–oxygen–inert gas mixture at atmospheric pressure. [50]

The latter account for a significant fraction of engine power output under light load and idle conditions where many engines operate most of the time. Consequently, quality regulation has the potential of providing an overall engine efficiency, which is much higher than that of gasoline engines. Quality regulation is unsatisfactory for gasoline engines because the lean flammability limit of gasoline is at an equivalence ratio ϕ of about 0.75, at which point the indicated power output has dropped off only about 30% from its maximum. In contrast, Diesel engines often are quality regulated, as are gas turbines.

2.2.2 Hydrogen mixture formation

Hydrogen induction techniques play a very dominant and sensitive role in determining the performance characteristics of the hydrogen fuelled internal combustion engine (H₂ICE). Hydrogen fuel delivery system can be broken down into two main types including the port injection and the direct injection

2.2.2.1 External mixture formation

Initial implementation of hydrogen fuel technologies included the usage of external mixture formation by either injecting hydrogen into an intake manifold or near the intake valve with port fuel injection (PFI)[7], [49]. It can be easily installed only with simple modification and its cost is low. The flow rate of hydrogen supplied can also be controlled conveniently[51]. External mixture formation by means of port fuel injection also has been demonstrated to result in higher engine efficiencies, extended lean operation, lower cyclic variation and lower NO_x production[52]. However, the most serious problem with PFI is the high possibility of pre-ignition and backfire, especially with rich mixtures.

First, backfire or backflash occurs when the fresh charge is ignited before the intake valve is closed and results from the hydrogen mixing with hot residual gases that remain in the cylinder after combustion. The early literature mentions causes of backfire and counter-measures as it so frequently occurs in hydrogen engines with external mixture formation. Since the minimum ignition energy of hydrogen, 0.02 mJ, is relatively small (10% of normal gasoline), hydrogen shows a large propensity to backfire, especially when using manifold fuel injection at stoichiometric conditions. Port fuel injection can be properly timed so that a very rich, non-ignitable mixture is introduced to residual that has already been cooled by fresh intake air and thus reduces or eliminates backfire.

The second combustion anomaly is pre-ignition and occurs when the new charge is ignited after the intake is closed but before the spark plug is fired. This occurs during compression and is a result of the hydrogen mixing with hot residual or contacting hot spots such as the spark plug or exhaust valves. It causes very large peak pressures and acoustic oscillations that can cause significant damage to the engine hardware. Again, pre-ignition is a result of the low ignition requirement of hydrogen. Pre-ignition is the main drawback of using port fuel injection because it reduces the maximum compression ratio and torque output of the engine. It has been reported that a port-injected hydrogen engine produces 35% less torque at low speeds and peak power is reduced by as much as 50% at high speeds relative to gasoline engines, mainly due to the inability to optimize engine parameters because of pre-ignition [41].

A problem with external mixture formation not directly related to combustion is that it causes an inherently low volumetric efficiency. The low density of hydrogen causes the intake hydrogen to consume 30% of the aspirated air volume. This causes a reduction in the maximum mean effective pressure and energy density inside the engine, reducing power output. The only option is to increase the intake pressure, but pre-ignition limits the possible amount of boosting [53].

2.2.2.2 Internal mixture formation

Internal mixture formation, or direct injection, can eliminate many of the combustion abnormalities associated with external mixture formation strategies. DI injection can be classified as early DI and late DI based on the start of injection. Early injection generally refers to any hydrogen DI during the early compression stroke, shortly after the closing of the intake valve, whereas late DI refers to strategies with the injection late in the compression stroke, generally ending just before spark timing [54]. This is accomplished by appropriately timing the injection event. Injecting the hydrogen after the intake valve has closed effectively eliminates the possibility of backfire. Also, the hot residual gases are more easily mixed with cool air with direct injection, reducing pre-ignition. At a stoichiometric ratio, 30% more air can be delivered to the cylinder when hydrogen is injected after the intake valve is closed, resulting in much higher energy density capabilities and a better volumetric efficiency [53]. Parameters such as start of injection and injection duration also play an important role in performance and emissions and can be optimized with direct injection.

The injector performance is critical to the overall performance of a direct-injection hydrogen engine. It must be able to cover a wide range of flow rates under varying load conditions and also promote proper mixing between the injected hydrogen and air. Wallner et al. demonstrated that optimization of efficiency with injection configurations in hydrogen DI strategy at low- and part-load conditions as well as at high engine loads led to an increase in the production of NO_x [55]. The injector must provide small amounts of hydrogen at idling conditions, but also very large amounts in very small time periods at high loads and speeds. These facts combined with the low density and low lubricity of hydrogen put a huge demand on the injector. Although, direct injection has been proven to be a better option than external mixture formation, current injector designs limit the engine to low to medium speeds.

2.3 Summary

Chapter 2 reviewed the modern concept for hydrogen direct injection spark ignition engine and their prospects and shortcoming. Hydrogen has unique fuel properties relative to typical gasoline and other popular fuels- wide flammability limits: (4-75% by volume– stoichiometric: 66% by volume) allow for hydrogen engines to run under very lean conditions, high flame speed: decreases losses due to non-ideal combustion processes and high octane number: (130) allows for increased efficiency due to a higher compression ratio. The DISI engine can operate fundamentally in two modes: the homogeneous (early injection) and the stratified-charge modes (late injection). Internal mixture formation, or direct injection, can eliminate many of the combustion abnormalities associated with external mixture formation strategies. Direct injection (DI) can be classified as early DI and late DI based on the start of injection.

3 Hydrogen jet analysis in a vessel

3.1 Introduction

Jet flow occurs when a stream of one fluid mixes with a surrounding medium, at rest or in motion. Such flows occur in a wide variety of situations, and the geometries, sizes, and flow conditions cover a large range. Fuel gases are generally injected into still air at high speed, usually at Mach number, Ma , greater than 0.3, in order to enhance turbulence and so mixing with the oxidant like oxygen in surrounding air. This implies that generally, the hydrogen jet binary mixture flow would also most probably be expected to be turbulent and compressible. This means that during jet propulsion, the flow gas mixture densities vary greatly with time and space as a result of high injection velocity, temperature changes, intense mixing between fuel gas and air. In the case of hydrogen gas diffusing in air these density variations near the jet boundary mixture are quite large because of the large mass diffusivity of the hydrogen gas-air medium. In addition, the large initial density difference between that of the injected hydrogen gas and ambient surrounding air which can be as high as 1400 % contributes to these large density variations. This section discusses about the details of jet structure at different ambient pressure condition.

3.2 Literature review on jets

A brief review of some contemporary experiment and analytical work done by some researcher on fluid jets in general and turbulent gas jets discharging into dissimilar surrounding gas in particular is perhaps appropriate and worth nothing at this stage. It has been noted that there has been more experimental and analytical work done on steady state jets than on unsteady jets. In addition, it seems from literature that more attention has been given to gas jets discharging into identical surrounding gas. In a direct-injection engine, the fuel injector issues fuel jets, which propagate across the combustion chamber. Understanding the physics of the gas jet is necessary to model the fuel jet injected into an engine cylinder. Although the main concern with automotive injection is the transient behaviour, steady jets provide a basis for understanding the structure and scaling of the transient jet. The behaviours of steady state jets are discussed in this section.

3.2.1 Turbulent jets and its regions

3.2.1.1 Incompressible jets

A steady, incompressible turbulent jet may be defined as a region of finite thickness, formed between two neighbour flows, with a continuous distribution of velocity, temperature and species concentration which result from turbulent disorderly movement of eddies cause by the instability of the tangential separation surface and exchange of matter .The compressibility effects in a flow can be neglected if the maximum Mach number is below 0.3. Incompressible jets have been studied extensively in the past [19][20][21]. As one fluid is injected into another fluid with uniform pressure field, a mixing layer is formed between the two fluids. Mass from the surrounding fluid is entrained in the injected fluid. Experimental investigations by Ricou and Spalding [19] concluded that, the rate of entrainment is proportional to the distance from the nozzle and to the mass injection rate for incompressible air jets issued from the round nozzle into stagnant air. A steady-state jet can be divided into three regions[22]. In the initial region the velocity in the potential core of the jet remains constant and is equal to the initial velocity. The end of the initial region is marked by the disappearance of the potential core because of the thickening of jet boundary layer. The transition region may be defined as the region in which the jet viscosity distribution becomes fully developed. In the fully developed region, the velocity profile is self-similar.

The structure and properties of incompressible transient jets or impulsively started jets have been studied for a wide range of applications. Turner [25] described the structure of plumes when studying atmospheric mixing in buoyant plumes. A plume was described as consisting of a spherical cap, called a spherical head vortex, which is supplied with additional buoyancy and momentum from a plume below. It was shown that the plume displays self-similarity characteristics throughout its evolution. Figure 3.1 illustrates this initial description of a jet or plume. The jet consists of a spherical vortex flow interacting with a steady-state jet. The vortex of radius moves away from the nozzle at a bulk velocity that decays with the distance from the nozzle. The size of the vortex grows continuously due to the entrainment of mass from the steady-state jet, which pushes it from behind. In turn, the steady state jet continually entrains the surrounding gas fluid from its side so that entrainment mainly occurs around the steady jet in the rear part of the transient jet. The jet behind the vortex is considered to be in a steady state, which is confirmed by the work of Kuo and Bracco [29]. As the injector is

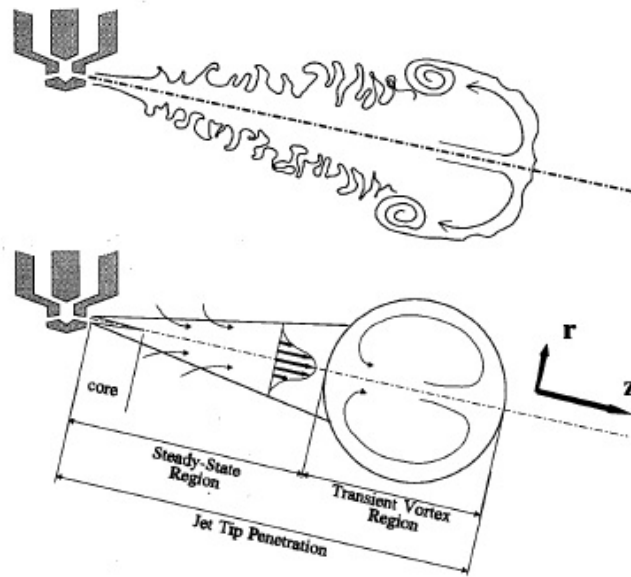


Figure 3.1 Transient Jet [25].

actuated, gas is injected through the nozzles and forms jets which propagate across the combustion chamber. Photographic evidence of impulsively started jets, such as those of Van Dyke [30] and Batchelor [31], shows that a vortex head is formed and propagates away from the nozzle, as depicted schematically in Fig. 3.1. In a so-called puff jet, the vortex head contains all of the injected fluid. In a transient jet, a quasi-steady jet is formed behind the vortex head. Abramovich and Solan [32] used this model to develop analytical expressions for the velocity of the spherical vortex in the near and far fields of a liquid jet under laminar conditions with low Reynolds number. It was observed that the velocity of the spherical vortex varies proportional to the distance similar to the axial velocity of a steady state jet only with differing constants. The velocity of the spherical vortex was found to be approximately half that of a fluid element in a steady jet. Abramovich and Solan [32] showed that the half width and maximum axial velocity show similarity characteristics, both making the jet appear to start from a virtual origin different from the geometric origin. The virtual origin was found to be proportional to the exit diameter and the square root of the Reynolds number. A previous study by Sato and Sakao [33] also found that an offset or virtual origin was needed to obtain agreement between experiment and theory with the origin moving downstream with increasing Reynolds number.

When the densities of the injected fluid and surrounding fluid are different, the entrainment rate is different. The centreline velocity is also different in this case. However, the similarity

of the profiles in the jet is still preserved at some distance from the nozzle. It is confirmed experimentally [19] that jets of different densities can be scaled when an equivalent diameter. The injected fluid and surrounding fluid densities respectively, taken at the same pressure. Thus, incompressible jets of different densities can be modelled by the equivalent diameter. This modification is directly obtainable from momentum conservation and similarity arguments. The difference in density may be the result of different molecular weights or of different temperature, or both.

3.2.1.2 Compressible jets

As the pressure ratio across the nozzle is increased, the velocity at the nozzle increases. As the Mach number increases above 0.3, compressibility effects have to be taken into account in establishing nozzle exit conditions. The similarity of profiles is still valid in the fully developed region where the local Mach numbers are low. However, the effect of compressibility on the nozzle density and velocity must be incorporated in the scaling. When the upstream to the chamber pressure ratio is greater than the critical pressure ratio for hydrogen jet, the exit plane pressure of the nozzle becomes higher than the chamber pressure, and an underexpansion occurs. An underexpanded jet consists of a complex structure of expansion waves and compression waves. Figure 2.1 shows a schematic of the expansion process outside the nozzle. The expansion waves reflect from the free boundary of the jet and become compression shocks that form a barrel shaped structure that is terminated by a normal shock also called the Mach disk [23]. The Mach disk form if the nozzle exits to chamber

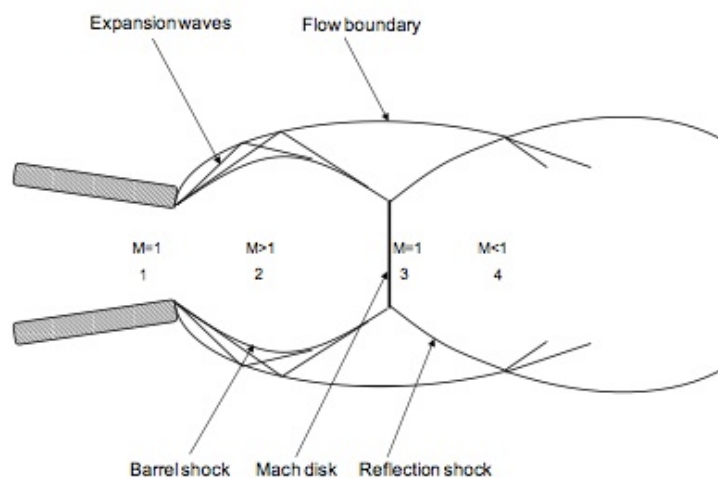


Figure 3.2 Underexpanded gas jet. [23]

pressure ratio is above 2.1 [24]. For steady subsonic flow of a perfect gas through a nozzle or an orifice, isentropic flow is assumed for which the following semi-empirical expressions apply,

$$\frac{T_2}{T_1} = \left(\frac{P_2}{P_1}\right)^{(\gamma-1)/\gamma} \quad (3.1)$$

$$\frac{P_2}{P_1} = \left[\frac{1+0.5(\gamma-1)Ma_1^2}{1+0.5(\gamma-1)Ma_2^2}\right]^{\gamma/(\gamma-1)} \quad (3.2)$$

where T , P and Ma are the static temperature, pressure and Mach number respectively. Subscripts 1 and 2 refer to the inlet and exit conditions; γ is the ratio of specific heats. According to Anderson [25], Abramovich [26] and Hinze [27], free jets can be assumed to be fully expanded so that pressure in the jets may be taken to equal to that of the surrounding fluid.

For flow from a nozzle or a large plenum (reservoir) through a small orifice, the following relation for the nozzle exit velocity, U_e , is obtained assuming steady, one-dimensional isentropic flow and applying the energy conservation principle,

$$U_e = \left\{ \frac{2\gamma P_s}{(1-\gamma)\rho_s} \left(1 - \left[\frac{P}{P_s} \right]^{(\gamma-1)/\gamma} \right) \right\}^{1/2} \quad (3.3)$$

where P_s and ρ_s are respectively the stagnation pressure and density in the reservoir or nozzle while P is the static pressure at the exit.

When the exit velocity reaches sonic level then an underexpanded jet is characterized by having an exit pressure higher than the ambient surroundings. The pressure, temperature, and density at the nozzle exit, assuming isentropic flow, are given in equations (3.4) through (3.6):

$$P_n = P_0 \left(\frac{2}{\gamma+1} \right)^{\gamma/(\gamma-1)} \quad (3.4)$$

$$T_n = T_0 \frac{2}{\gamma+1} \quad (3.5)$$

$$\rho_n = \rho_0 \left(\frac{2}{\gamma+1} \right)^{1/(\gamma-1)} \quad (3.6)$$

where γ is the ratio of specific heats, the subscript n denotes nozzle exit conditions and 0 denotes stagnation conditions. The sonic velocity, c is evaluated from,

$$c = \sqrt{\gamma R_g T_n} \quad (3.7)$$

where, R_g is the gas constant.

3.2.2 Comparisons of gaseous jets and sprays

There is much interest in knowing whether gaseous jets penetrate and mix with the same dependencies as sprays. Sprays have been the objects of continuous research, as efforts were made to reduce emissions from diesel engines. Consequently, diesel engines operate on optimized injection conditions, and it may be that these conditions can be transposed with success to gaseous jets. A first point of comparison is the penetration rate of sprays. Diesel engine researchers have used analogy to gas jets to establish the main dependency of spray penetration.

Flow visualization of both sprays and gaseous jets performed by Miyake [34] illustrates this point. His photographs show that when injected with the same momentum rate, gaseous jets and non-evaporating sprays have visually a similar spreading angle and very similar penetration rate. Kuo and Bracco [29] reviewed the difference between turbulent jets and sprays. They note from observation of flow visualization that both transient sprays and jets have a stem and a vortex head that scale in time in similar fashion. However they also point to a major difference between sprays and jets; whereas jets have little dependency on the geometry of the nozzle, sprays are very dependent on the nozzle geometry, as evidenced by a wealth of experimental observations [35]. In particular, the angle of spread of sprays is found to be dependent on the density ratio between the liquid and the chamber, and on the length-to-diameter (L/d) ratio of the nozzles. Typically, the spray cone angle is reduced by an increasing liquid-to-air density ratio and by an increasing U_d ratio. The reason for the nozzle influence is that the initial spreading of the liquid spray is an aerodynamic phenomenon, at least near the nozzle, whereas the spreading angle of jets is a shear-induced mass transfer.

3.3 Measurement method

3.3.1 Constant volume vessel

A constant volume vessel was used for the hydrogen jet visualization to eliminate the effect of air flow. The closed vessel was made from a 125-mm-long and 80-mm-diameter steel cylinder (Fig. 3.3). The three walls of the chamber were formed from circular quartz windows to permit full line-of-sight optical access to the chamber. The hydrogen injector was mounted at the upper end plate of the closed vessel so that the jet was directed axially into the cylinder. A pressure accumulating-type injector was used and actuated by an electromagnetic valve. The ambient gas was nitrogen, and was collected from an N₂ cylinder and introduced into the vessel by a pressure-regulated inlet valve. Hydrogen was supplied from an H₂ cylinder and a fuel accumulator (see Fig. 3.5) was used to maintain constant fuel feed pressure to the injector.

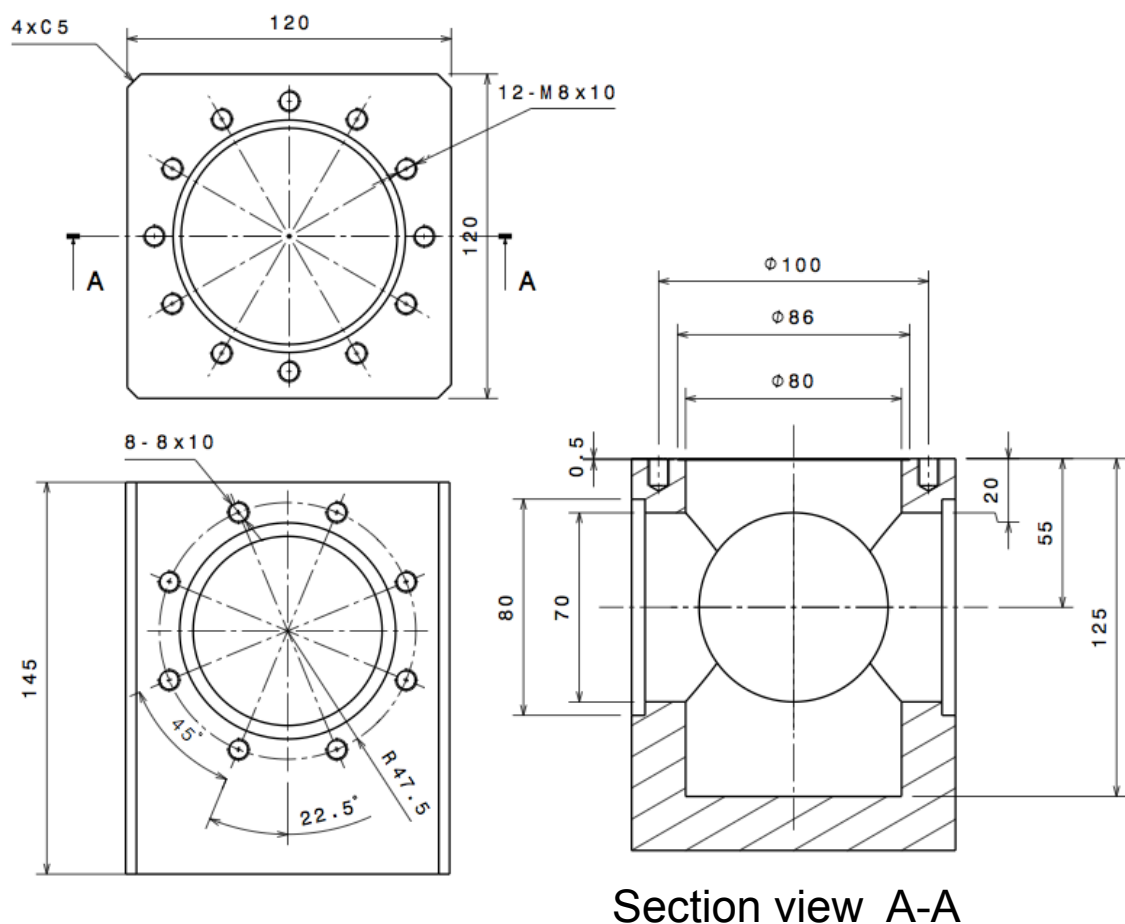


Figure 3.3 Constant volume vessel used in hydrogen jet visualization.

3.3.2 Injector

A solenoid-driven gasoline direct injection (GDI) injector used as a fuel injector developed by Mitsubishi Electric Co. Ltd is shown in Fig. 3.4. The fuel injector was a swirl-type DI injector and the H₂ was introduced through a single orifice. The injector had a nominal cone angle of 60° and an orifice diameter of 1.0 mm. The injection signal was controlled by an electric injector driver requiring a high-voltage power source and external trigger input to control the pulse width.

3.3.3 Jet visualization using a high-speed camera

A high-speed CMOS (complimentary metal-oxide semiconductor) video camera (NAC GX1) was used to visualize the hydrogen jet in the constant volume vessel. The frame resolution was 256×256 pixels and the capture rate was 25,000 frames per second. The onset of the high-speed camera recording was synchronized to the H₂ injection. Figure 3.5 shows the optical system used to image the jet flow.

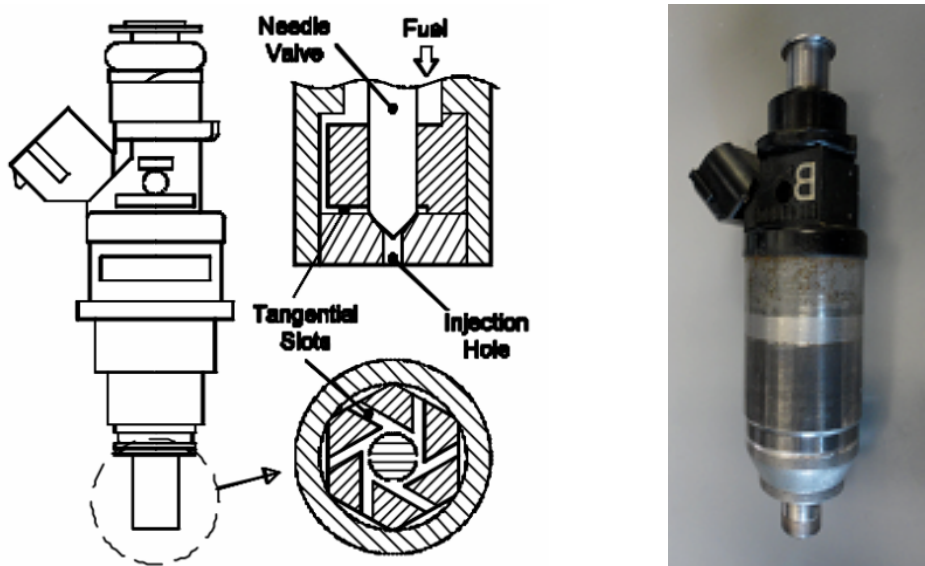


Figure 3.4 Mitsubishi DI injector

3.4 Experimental method

The constant-volume chamber was filled with nitrogen gas and the hydrogen jet was injected into the chamber. An Argon-ion laser beam (Spectra-physics, Stabilite 2017) with an output power of 6W was used as the light source. The thickness of the laser light sheet was approximately 2 mm. The laser beam was focused on the hydrogen jet, and the visualization region was approximately $20 \times 20 \text{ mm}^2$ near the nozzle tip. A fine particle of spherical porous silica (God Ball B-6C, Suzuki Yushi Co. Ltd.) with a nominal diameter of $2.5 \mu\text{m}$ was seeded into the intake flow (choosing the appropriate size of the flow field visualization tracer was very important to accurately track the airflow). The origin of the jet image is located at the centerline of the jet exit. The Z_p and r denotes the jet axis direction and radial direction, respectively. The high-speed images provided qualitative information of the jet structure, as well as quantitative information of the jet penetration and cone angle.

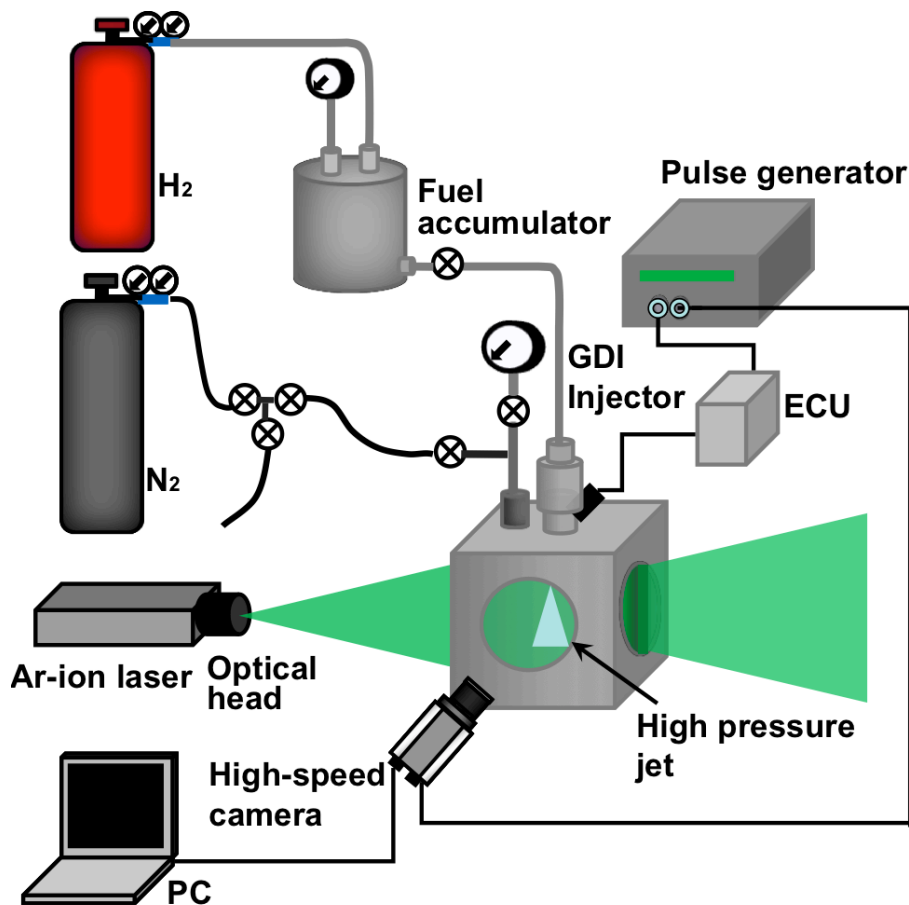


Figure 3.5 Experimental setup for hydrogen jet visualization.

3.4.1 Operating conditions

The characteristics and operating conditions of the constant-volume chamber and the injector are summarized in Table 2.

Table 2 Operating condition for constant volume experiments

Chamber volume (cm ³)		628.31			
Chamber wall temperature (K)		298			
Orifice diameter (mm)		1.0			
Injection duration (ms)		4			
Mass of H ₂ injected at 5MPa (mg)		2.07			
Fuel injection pressure with ambient condition					
Fuel	Fuel injection pressure, MPa	Ambient pressure, MPa (Ambient density, kg/m ³)			
		N ₂	N ₂	N ₂	N ₂
H ₂	3	0.1 (1.15)	0.5 (5.611)	1.0 (11.22)	1.5 (16.83)
H ₂	5	0.1 (1.15)	0.5 (5.611)	1.0 (11.22)	1.5 (16.83)

3.5 Flow visualization of hydrogen jet in a constant vessel

There are two main objectives to the experimental investigation presented in this chapter. First, the experiments are to substantiate the proposed scaling for transient hydrogen jets. Second, the experiments are to validate the multidimensional simulations of transient hydrogen jet. In both these objectives, an accurate description of the nozzle condition is required, since both require the nozzle gas density and the nozzle gas velocity. The hydrogen jets are experimentally characterized by measuring the tip penetration as a function of time. In particular, the transient needle lift information and more accurate pressure measurements were required and obtained for the establishment of more accurate boundary conditions for the numerical modelling. The experimental apparatus and method are presented in chapter 3.3.1.

3.5.1 Effects of injection pressure

This section concerns the hydrogen jet in the constant-volume vessel. In ICEs, the mixing rate of the injected fuel with air is important because it affects the combustion rate. Gas injection at high pressure can increase the momentum injected into the cylinder, the mixture turbulence level, and the overall amount of fuel-air mixture. The penetration depth and jet cone angle are important factors. Unlike gasoline fuel, there is no droplet formation or evaporation during the injection process. In Figure 3.6 a) - c) show the development of the hydrogen jet for an injection pressure of 3 MPa and various ambient pressures. The constant-volume chamber was filled with N₂ at different pressures. The ambient pressure was varied from atmospheric pressure to 1.5 MPa, changing the ambient density from 1.15 to 16.83 kg/m³. The image shows that the jet diameter expands rapidly just downstream from the nozzle exit. The fuel jet dispersed slightly more in low ambient density than in high ambient density. The intensities of the image can be related to the gas concentration. Although the jet penetration of each single shot image is in the same range, the jet pattern and local concentration fields are significantly different from each other. The border of each single shot image is also quite irregular, especially little bit far away from the injector. The variation of injection-to-injection and intensity turbulence flow of gas jet would be the major reason. It might be another reason that the low momentum of gas jet could be easily and randomly distributed by surrounding air. This type of behaviours is also seen in liquid sprays.

Figure 3.6 a) shows a jet plume which appears to penetrate faster than the plumes in Figure 3.6 b) and c). At $t = 0.24$ ms, and at the increased ambient pressure corresponding to Figure 3.6 c), a vortex ring formed around the jet tip and this vortex, which grew upwards over time. Figure 3.7 a) - c) along with Figure 3.6 a) - c) show sequential images of the 5-MPa injection pressure jet injected into environments of high and low ambient density. The higher injection pressure in Figure 3.7 a) - c) resulted in faster growth of the hydrogen plume than for the lower injection pressure. Comparison of Figure 3.5 and Figure 3.6 shows that increasing the injection pressure resulted in a significant difference in the jet structure in the initial part of the injection for all the different ambient pressures.

The air-entrainment which is caused by the shear induced turbulence and momentum exchange between fuel and air is the dominant factor for gas jet mixing process. The main

mechanism for entrainment is through engulfment of ambient air along the upstream edge of the large-scale structures. Subsequent mixing occurs as the interface formed between the entrained ambient air and the jet gas is stretched, and both jet and entrained air come into contact at ever smaller scales until the fluid from the two streams becomes molecularly mixed at the Kolmogorov scale. Figure 3.8(a) displays the conceptual profile for the entrainment and mixing process of axisymmetric gas jet. Based on the concentration distribution, the vortex regions (white circle as shown in figure 3.8(b) could be seen at the sides but near the tip of jet. During the gas injection, the jet tip pushes out the still ambient nitrogen, and then the vortex structure is formed by the interaction between the jet and the ambient nitrogen. This kind of vortex structure could also easily happen in flash boiling spray and swirl injector spray . The more basic reason for vortex structure should be also seen in liquid sprays or flash boiling sprays tip. Actually, both the vortex formation and vortex broken are quite useful for fuel-air mixing and the mixture diffusion. The flow induced by the vortex was squeezed out the fuel from the jet tip, which is thought to cause the entrainment of the fuel to the surrounding nitrogen. The symmetry of the vortex may account for the slower spreading of the jet.

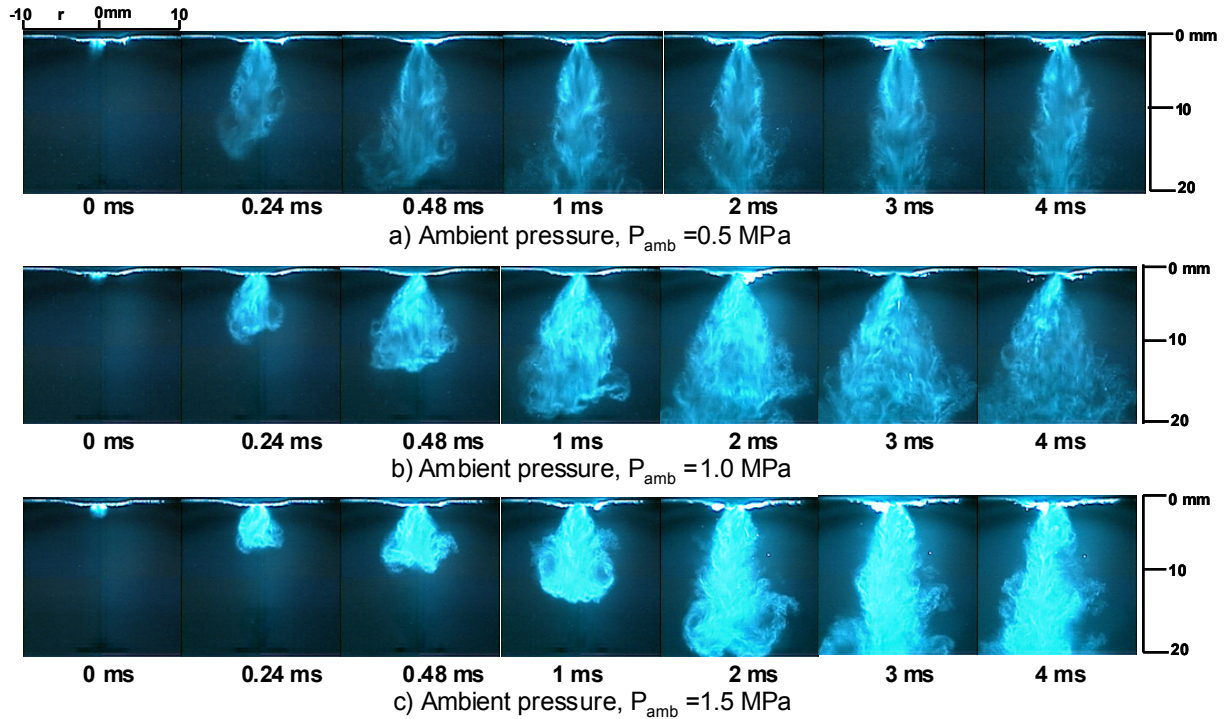


Figure 3.6 High-speed direct images of a 3-MPa injection pressure hydrogen jet into three different ambient pressure N_2 -filled chambers. The recording speed was 25,000 frames/s.

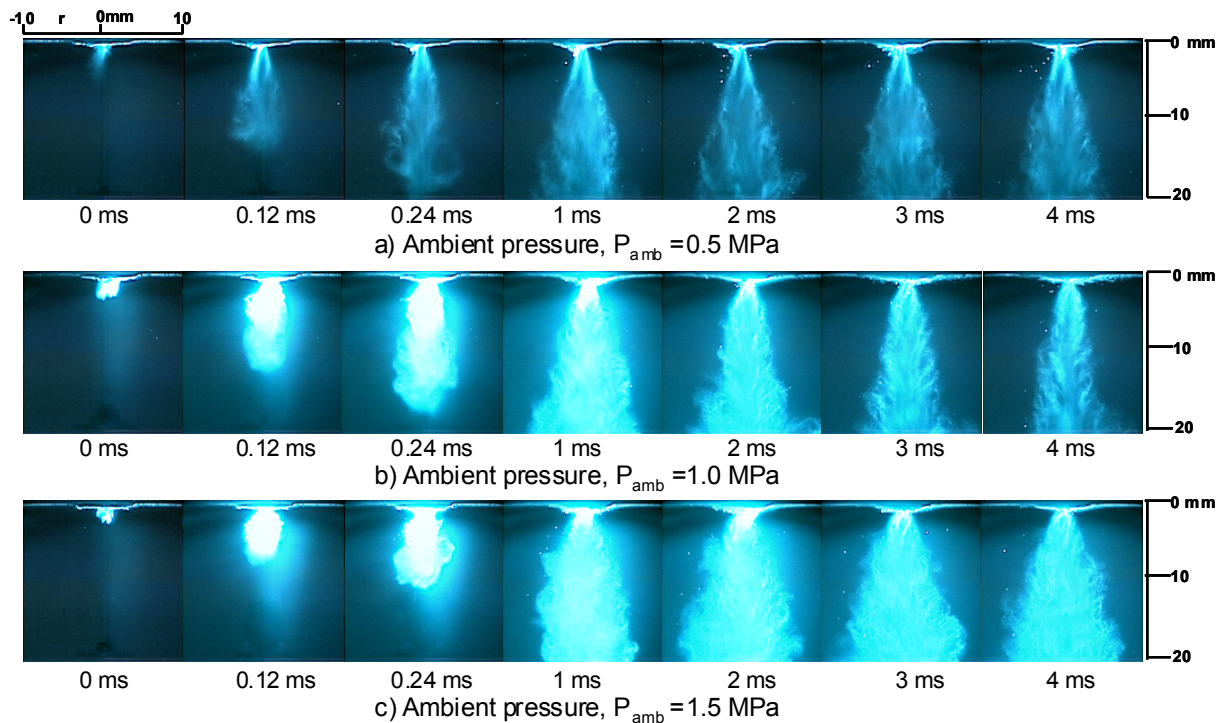


Figure 3.7 High-speed direct images of a 5-MPa injection pressure hydrogen jet into three different ambient pressure N_2 -filled chambers. The recording speed was 25,000 frames/s.

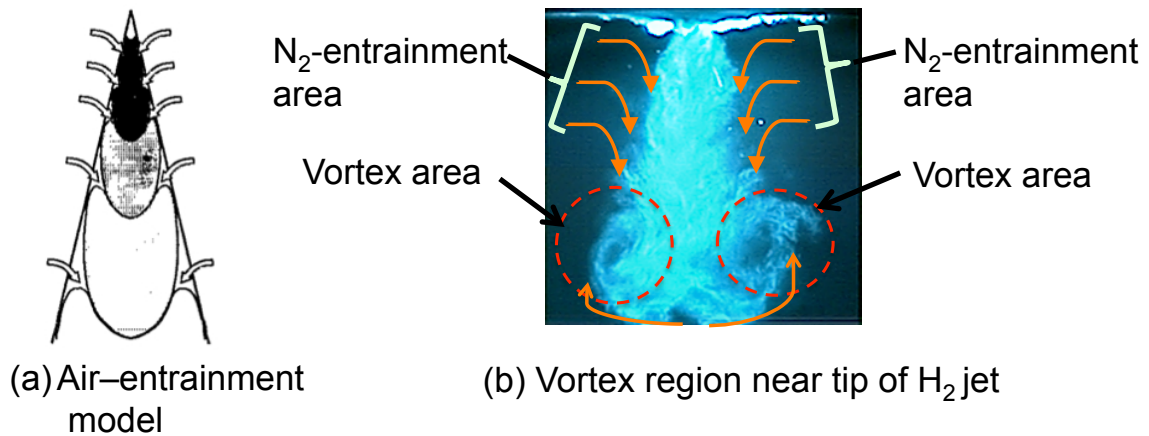


Figure 3.8 Ambient entrainment pattern and vortex region.

3.5.2 Jet penetration at different injection pressure

3.5.2.1 Penetration measurements method

A typical high-speed direct photograph of the H_2 jet is shown in Fig. 3.9. It is seen that upstream the jet flow, the flow is very smooth possibly due to the very small eddies produced near the jet flow in this region of the jet. However, further downstream the roughness of the jet boundary is clearly visible and the existence of much larger eddies which are also visible is verified by the photograph to a good extent. The photograph also shows that the jet flow is actually not symmetrical about the jet axis. The experimental jet penetration was determined using axial distance. In this method axial penetration distances were obtained from high-speed direct photographs taken at different times during jet flow development. The pixel intensity was measured along the centerline of an jet. The vertical penetration was then defined as the location where the centerline intensity fell below a certain value, starting from the bottom of an image. Figure 3.9 further illustrates this technique.

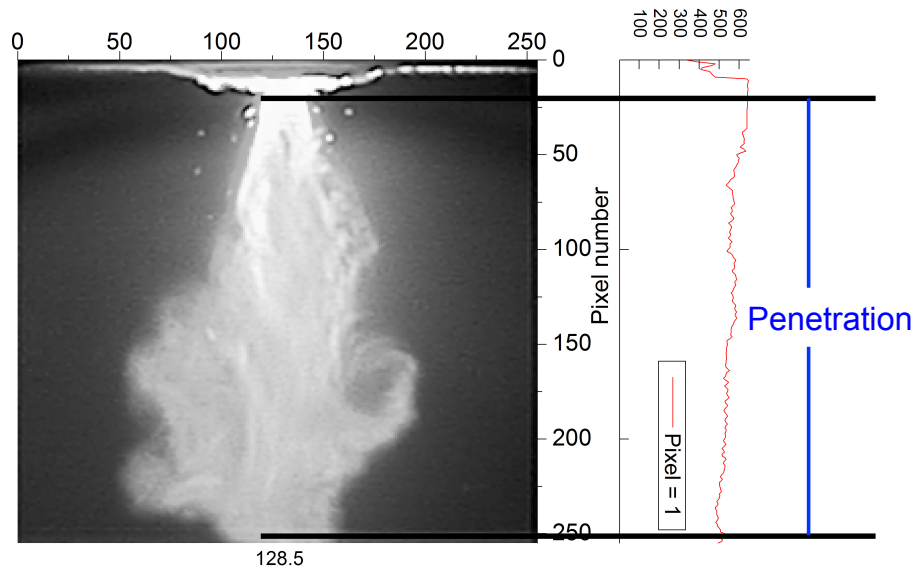


Figure 3.9 Jet penetration measurement, plot shows pixel intensity along centerline of jet.

3.5.2.2 Jet penetration rate

Figure 3.10 a) - b) show the jet penetration as a function of time for a range of injection and ambient pressures. The graph shows the hydrogen penetration depth, Z_p , as a function of time, t , in from the onset of injection. The penetration of the jets was determined from the axial distance from the nozzle tip to 20 mm from the tip of the jet. The penetration lengths indicate that sufficient distance would be travelled by the gas jet for satisfactory air-fuel mixing in the combustion chamber of an ICE. Figure 3.10 a) shows the jet penetration rate into different ambient pressure levels with an injection pressure of 3 MPa. Different penetration rates were obtained depending on the ambient pressure in the chamber. Figure 3.10 b) shows that, at an injection pressure $P_{inj}=5$ MPa, the jet penetration increased with increasing injection pressure; however, it also decreased due to the higher ambient pressure. In all cases, the tip penetration rate increased in the near-nozzle region and then decreased downstream, which may be due to N_2 entrainment. Similar trends were observed in diesel engine spray patterns, where, at constant injection pressure, an increase in the ambient pressure caused a reduction in the penetration rate, which is equivalent to a reduction of the jet exit momentum [82].

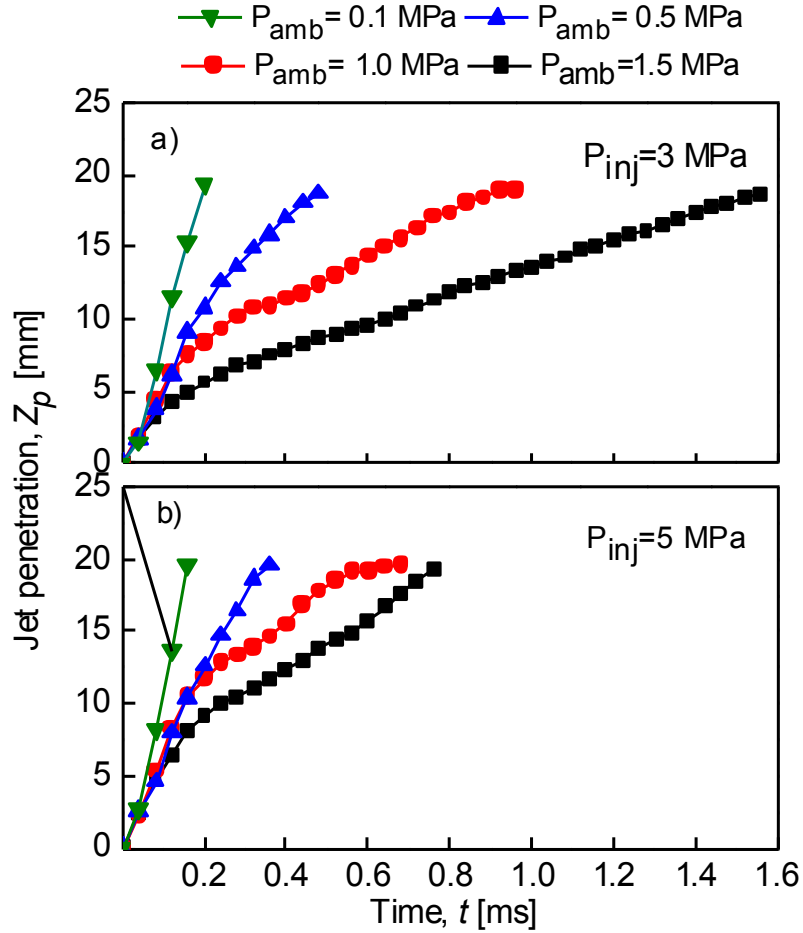


Figure 3.10 Jet tip penetration for a) an injection pressure of 3 MPa and b) 5 MPa

3.5.3 Jet cone angle at different injection pressure

3.5.3.1 Jet angle measurements method

The jet angle, θ , is calculated by measuring the projected area, A_{p,Z_p} , contained within the jet taken at different times during jet flow development and approximating the jet as a triangle in this initial region before the head vortex. The relation for calculating θ is illustrated in Figure 3.11 and is given in equation 3.8.

$$\frac{\theta}{2} = \tan^{-1} \left(\frac{A_{p,Z_p}}{Z_p} \right) \quad (3.8)$$

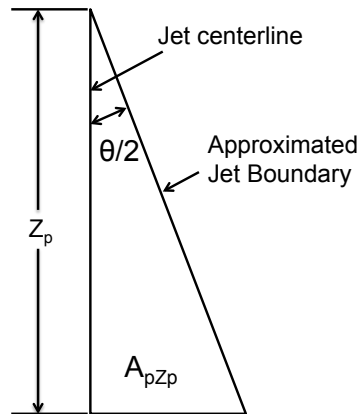


Figure 3.11 Jet geometry to determination jet angle.

3.5.3.2 Jet cone angle

Figure 3.12 a) - b) show the effect of the injection pressure on the jet angle as a function of time after the onset of injection. The cone angle was characterized by measuring the angle generated by a triangle connecting the center of the nozzle tip and the widest horizontal span of the gas jet. The jet cone angle was measured 20-mm from the nozzle tip. The jet cone angle is the parameter, which is most commonly used to describe spray distribution, and is important because it affects the axial and radial distribution of the fuel. At $t = 1$ ms, Figure 3.12 a) shows that an increase in the ambient pressure results in a maximum jet angle. An increase in the jet angle results in slower penetration of the fuel jet in the downstream region. Slower penetration occurs because the larger cone angle reflects greater N_2 entrainment, and also because the density of hydrogen is much lower than that of nitrogen. From conservation of momentum, a greater mass of air in the fuel jet results in lower overall jet velocities at any axial location, and thus slower tips penetration [83]. Moreover, the ambient air moves nearly perpendicular to the jet boundary and is entrained into the jet, and a change in the direction of the jet axis in the upstream region has been reported [55]. Figure 3.12 b) shows that increasing the injection pressure results in a lower initial jet angle because the total fuel mass increased with increasing the injection pressure. The relatively low injection pressure of 3 MPa resulted in jets with a larger initial jet angle than the higher injection pressure of 5 MPa.

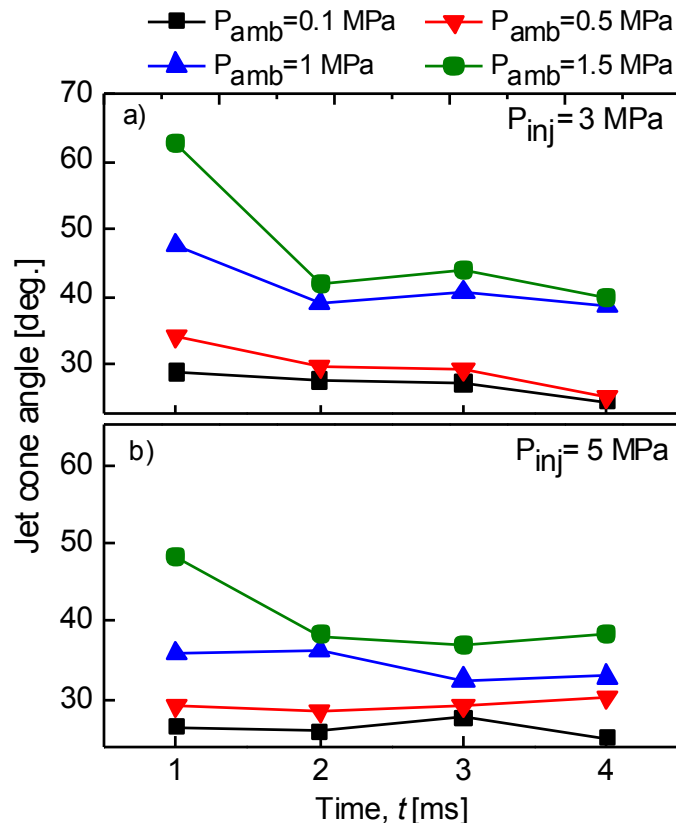


Figure 3.12 Jet cone angle for a) an injection pressure of 3 MPa and b) 5 MPa

3.6 Summary

An Argon (Ar)-ion laser beam was used as a light source to visualize the hydrogen jet development at the nozzle exit in a constant-volume chamber. This allowed us to study the structure of the jet in addition to other physical processes resulting from hydrogen gas injection. The penetration depth and jet cone angle are important factors. The experimental results showed that the jet penetration rate increased with increasing injection pressure, and decreased with increasing ambient pressure. Moreover, the effect of injection pressure at 3 MPa resulted in larger initial jet angle than the injection pressure of 5 MPa. Varying the ambient density from 1.15 to 16.83 kg/m³ changed the structure of the fuel jet. Direct visualization of hydrogen jet gives the useful information where the jet tip pushes out the still ambient nitrogen, and then the vortex structure is formed by the interaction between the jet and the ambient nitrogen. Gas injection at high pressure can increase the momentum injected into the cylinder, the mixture turbulence level, and the overall amount of fuel-air mixture.

4 Jet-guided combustion characteristics

4.1 Introduction

Very little work has been reported on hydrogen DISI engines in the late stages of the compression stroke, especially under stratified charge operating conditions. A need exists for high-resolution direct-combustion images to measure the fuel distribution and flame propagation under a range of operating conditions and varying parameters, including fuel injection timing, ignition timing, and fuel–air equivalence ratio. Therefore, two features are pertinent to the present study. High-resolution direct images of spark-ignited combustion are acquired to investigate the effect of fuel-injection timing in terms of the flame propagation and combustion rate. The experimental apparatus and method are presented in chapter 4.4.

4.2 Literature review

Hydrogen has been the subject of numerous studies with internal combustion engines. Although its wide flammability limits provide important advantages, such as the possibility of using quality control, its easy ignitability by external sources and its rapid burning rate can lead to serious operational problems. In contrast, the same combustion characteristics impose technical challenges at high engine-loads due to an increased propensity to preignite the hydrogen–air mixture and increased NO_x production. Therefore, many research studies determining the practical operational limits, and advanced control strategies include intake charge cooling [84], variable valve timing for effective scavenging of exhaust residuals [85], advanced ignition systems[86], and hydrogen direct injection (DI) [87][88]. Furuhashi et al. [89] and Knorr et al. [94] report that preignition can be eliminated without too much effort simply due to the cooling effect of the cold hydrogen. Kondo et al. [86] used an ignition system specifically designed to prevent residual energy and water cooled spark plug. Recent work indicates that direct cylinder injection is a promising way to circumvent these problems. The views is based on the high volumetric efficiency, (since hydrogen is injected after intake valve closing) and the potential to avoid preignition. The latter effect is controlled by timing injection to both minimize the residence time that a combustible mixture is exposed to in-cylinder hot-spots (i.e., late injection) and allow for improved mixing of the intake air with the residual gases. Homan et al. [88] used DI late in the compression stroke and near-simultaneous spark to eliminate preignition events. However, to prevent misfires, the hydrogen jet had to be directed towards the spark. For convenience, this scheme will be called the late injection, rapid ignition and mixing (LIRIAM) scheme to differentiate it from other

direct injection schemes for which all or most of the hydrogen is injected prior to ignition. In principle Homan et al. termed this operating scheme the LIRIAM scheme offers a successful method for avoiding undesirable combustion. The experiments were performed on a Waukesha Motor Company single-cylinder Cooperative Fuel Research (CFR) piston engine, with an engine displacement of 612 cm³. Cylinder heads were used is the Otto head configuration shown in Fig. 4.1 a); it was modified for this study by the placement of a spark plug, with a cylinder pressure sensor, in the top opening. A specially built hydrogen injector was mounted in the cylinder wall opening normally occupied by the spark plug. As shown in Fig. 4.1 a) the hydrogen could be injected radially or tangentially into the Otto head cylinder. Indicated efficiency and the specific NO_x emissions are presented as functions of spark timing for the Otto head in Fig. 4.1 b). The spark timing for maximum indicated efficiency was 5° BTC for the equivalence ratio 0.43 and indicated efficiency dropped by 6% with a change in spark timing of ±10° crank angle. Moreover NO_x emission was decreasing with advance spark timing.

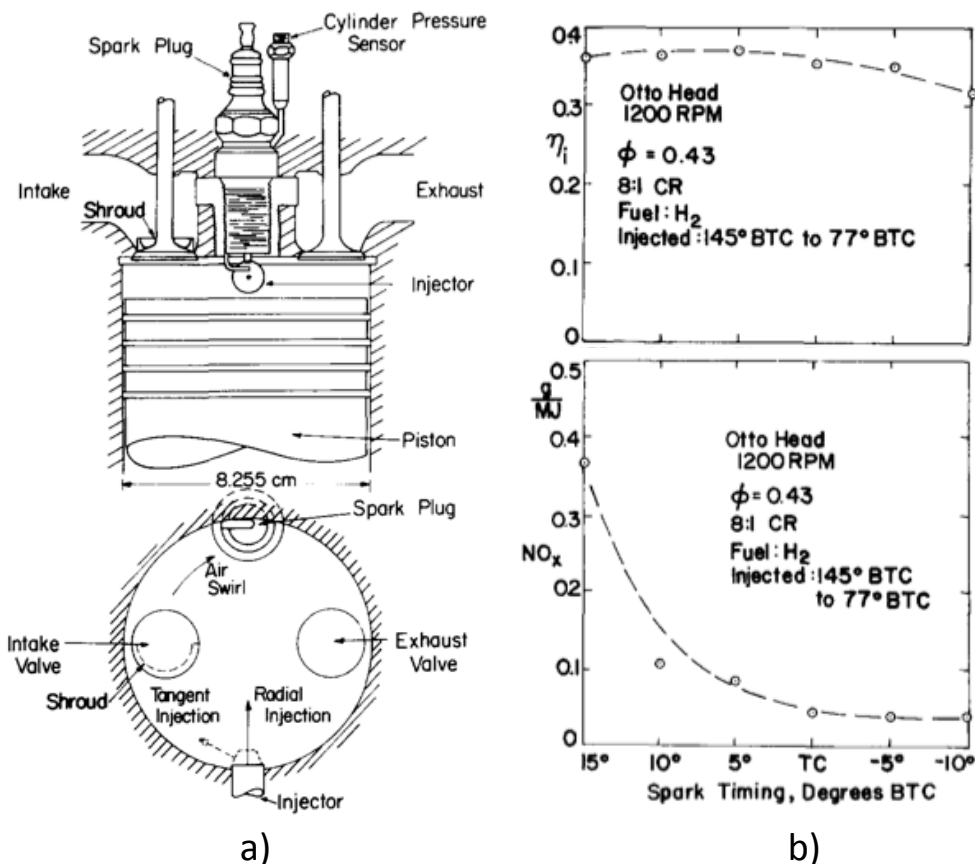
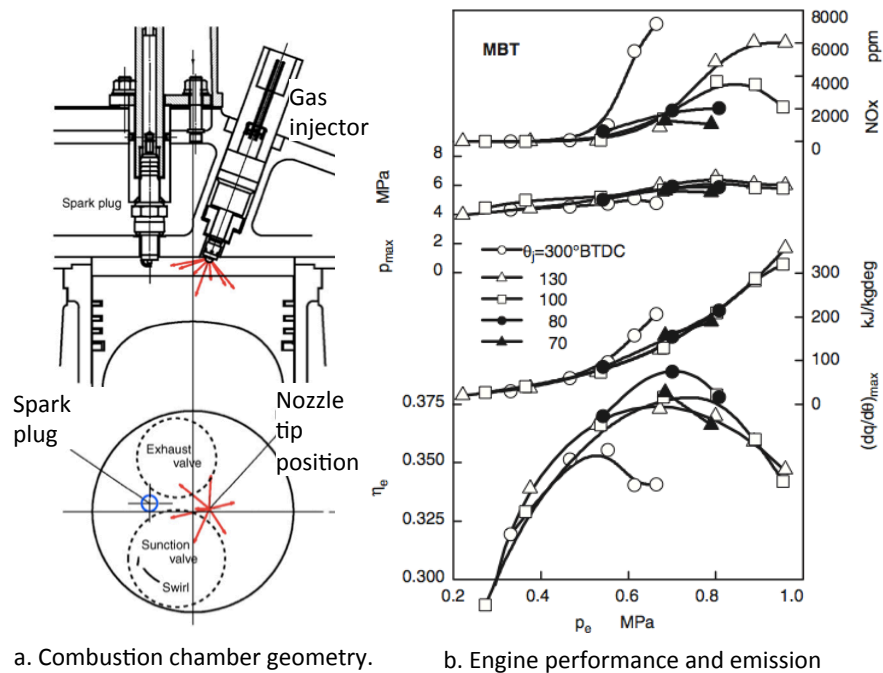


Figure 4.1 The influence of spark timing, a) Otto head configuration of the CFR engine , b) indicate efficiency, NO_x vs spark timing.[88]

Effects of the injector location and nozzle design on the efficiency and emissions of a direct-injection hydrogen engine were studied by Wallner et al. [13]. Effects of compression ratio, equivalence ratio, and engine speed on the performance and combustion characteristics of a direct-injection SI engine using hydrogen was also investigated by Mohammadi et al. [8]. Fig. 4.2 shows the engine performance, combustion characteristics and NOx emissions against brake mean effective pressure p_e when injection timing was varied in the range of $\theta_j = 70^\circ, 80^\circ, 100^\circ, 300^\circ$ BTDC. For injection timing of $\theta_j = 300^\circ$ BTDC, when fuel injection is carried out during the intake stroke, maximum engine output is limited to $p_e = 0.65$. As described already, this is due to a decrease in volumetric efficiency, which finally results in knock. Injection timing of 100° and 130° BTDC extends the engine operation toward lower and higher p_e , where 130° BTDC gives slightly higher thermal efficiency at $p_e = 0.7, 0.8$. Further delay in injection timing to 80° BTDC improves the thermal efficiency η_e at $p_e = 0.55-0.8$. However, in this condition, engine operation under low engine load was difficult due to an increase in the combustion fluctuation. In this study, maximum thermal efficiency η_e was achieved for 80° BTDC that is 38.9%. As can be seen in the NOx results, NOx emissions for 80° BTDC at $p_e = 0.8$ MPa is 60% lower than that for 130° BTDC. This would be due to increase in heterogeneity of fuel-air mixture caused by retard in the injection timing. Above results reveal that optimization of injection timing is an effective method to obtain high thermal efficiency and low NOx emissions for a given engine load.



4.2 Engine performance and emission of a Hydrogen DISI engine.[8]

4.3 Plume Ignition Combustion Concept (PCC)

A new ignition-combustion concept named PCC (Plumed Ignition Combustion Concept) in which with an optimal in which with an optimal combination of hydrogen injection timing and ignition timing, the plume tail of the hydrogen jet is spark-ignited upon the completion of fuel injection to accomplish combustion of a rich mixture. PCC combustion are similar to Homan et al. [88] developed LIRIAM combustion. This PCC combustion process markedly reduces NO_x emissions in the high-output region while maintaining high levels of thermal efficiency and power. Moreover, test results confirm the potential of PCC combustion for reducing NO_x emissions to a level complying with Japan's 2009 exhaust emission regulations for heavy-duty vehicle engines by using exhaust gas recirculation (EGR) alone without applying any exhaust after treatment system [14]. However, the details of the conditions required for viable PCC combustion leading to a substantial reduction in NO_x emissions are still not clear.

Figure 4.3 shows the combustion chamber configuration, arrangement of the injector nozzle and the spark plug. The combustion chamber had a bowl that was formed in the piston. The injector nozzle machined in a nozzle cap was oriented such that the hydrogen jet was aimed at the piston bowl when the piston was at top dead center. Seven single-hole nozzles having hole diameters of 1.7, 2.0, 2.3, 2.9, 4.0, 4.5 and 5.0 mm and one multi-hole nozzle with nine holes of 1.3mm in diameter were used in the experiments. Spark plug was positioned 20 mm from the injector nozzle hole.

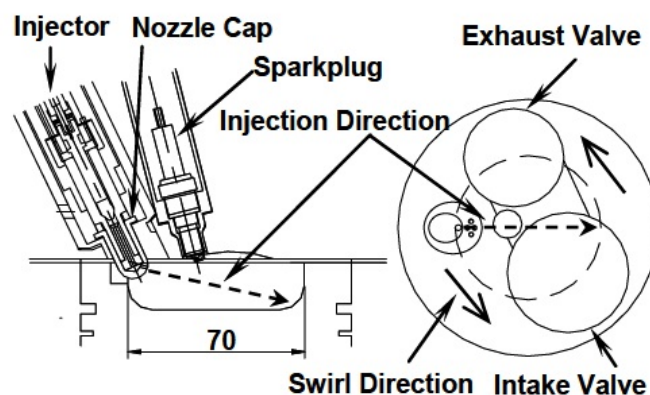


Figure 4.3 PCC combustion concepts

4.4 Factors that influence ignition

Since combustion initiation and hence, spark ignition, is primordial to the subsequent combustion of the fuel in the combustion chamber, it is essential to review the main factors that influence ignition and how we can quantify the benefit of an ignition system on the engine operation. The repeatability of the combustion process is a measure of the stability of the combustion of engines and is one of the reasons to study advanced ignition systems. The variance of the stability in combustion between cycles is measured with the coefficient of variance (standard deviation divided by mean) of the indicated mean effective pressure (COV of IMEP). As the COV of IMEP decreases, it implies that the variance of the produced work is also reduced when compared to the mean produced work. The cyclic variability is a limit for DISI engine with lean mixtures because the COV of IMEP can reduce driveability when its value reaches 10%. Other factors that affect the COV of IMEP are the mixture composition, the cyclic variation of the cylinder charging and the in-cylinder flow. The air/fuel ratio of the mixture and the intensity of the in-cylinder flow motion will influence the energy required to sustain early flame growth

4.4.1 In-cylinder flow

As stated previously, the combustion process inside the DISI engine and the COV of IMEP are dependent on the kind of in-cylinder flow and the injection timing. All commercial DISI engines use swirl or tumble as in-cylinder flow. As reported by Hill and co-worker's [89], the main reason is that both flows increase the burning rate and can extend the stability limit. Tumble motion as an in-cylinder flow has been chosen more often than swirl in the first generation of commercial DISI engines. One possible reason is that tumble might be easier to obtain than swirl, which needs a more complex geometry of the intake port near the valve to generate a rotating flow. Swirl generation has a tendency to reduce the volumetric efficiency of the engine.

Tumble or swirl generates controlled turbulence. The increase of turbulence is normally associated with an acceleration of the combustion. In his review of engine rotating flows, Hill [89] reported that tumble reduces cyclic variability and can be an effective technique to improve the thermal efficiency of lean burn engines. However, as the tumble motion increases, heat loss becomes more significant and the effectiveness of the tumble might be more dependent on the ignition process, like spark current intensity and duration. The

turbulence generated by the tumble flow near the end of compression has a direct effect on the minimum ignition energy. Tabaczynski [90] reported that, for a fixed air-fuel ratio, the required minimum energy to ignite a mixture increased with the intensity of the turbulence. The minimum energy requirement increased when the mixture departed from the stoichiometric value. This increase of energy with the intensity of the turbulence can be explained as follows:

1. Turbulence stretches the spark channel length which increases the volume into which the ignition energy must be deposited;
2. Turbulence increases heat loss that translates to a decrease of energy available for ignition;

Hence, turbulence increases combustion propagation speed on one hand but also increases the energy requirement for successful ignition on the other.

4.4.2 Air-fuel mixture

DISI engines have one principal advantage over PFI engines in that the mixture formation can be controlled. In PFI engines, the fuel is injected in the intake manifold near the valve while in DISI, the fuel is injected in the combustion chamber and can benefit from the in-cylinder motion. That is how one can explain why DISI engines can sustain leaner mixture combustion than PFI. There are two kinds of injection strategies in DISI engines, homogeneous and stratified. The first one concerns injection during the intake stroke while the later during the compression stroke. Stratified injection permits injection of a small amount of fuel near the end of compression, which is directed, with the help of the in-cylinder flow, piston geometry and injector orientation, to the spark plug. One can, hence, achieve a local rich mixture that is ignitable while the overall fuel/air mixture is lean.

One effect of the mixture air-fuel ratio is on the exhaust gas emissions. The stratification of the fuel and the associated overall lean mixture is associated with slower flame propagation. Also as the mixture becomes leaner, the energy requirement to ignite is augmented. In the case of fuel stratification, the energy requirement increases also because of the fuel does not have sufficient time to oxidize. Another effect of the air-fuel mixture is related to the fuel concentration near the spark plug at the time of ignition. Williams and co-workers [91] used a direct-injection engine where both, the injector and spark plug are centrally mounted. They

studied the effect of injection timing during the intake stroke (homogeneous injection) for a stoichiometric mixture. They found that when the injection was taking place after 150 degrees ATDC in the intake stroke, it resulted with an increase of inhomogeneity of the mixture, which is responsible to cyclic variation of the combustion. Alger and co-worker's [91] studied the effect of in-cylinder motion and injection timing in a DISI optical engine on the fuel concentration near the spark plug. From their data, the fuel concentration in the vicinity of the spark plug experienced increased fluctuations as the injection timing was retarded from homogeneous injection (90 ATDC degrees intake stroke) to stratified injection (90 degrees BTDC compression stroke).

4.5 Experimental method

4.5.1 DISI optical engine

A specially designed single-cylinder compression-expansion engine that could only be fired once was used for the experiments. This engine can observe only single cycle combustion phenomena in one experimental run. A summary of engine specifications is provided in Table 3. A custom head was built specifically for the DISI application. A schematic diagram of the engine with the optical diagnostic geometry is shown in Figure 4.4. This engine had only one intake valve. The in-cylinder exhaust gas was drawn out by a vacuum pump through the inlet valve. The engine was driven by an electric motor when the piston was set at TDC position.

Table 3 Engine specifications

Bore	78 mm
Stroke	67 mm
Displacement	310.59 cm ³
Compression ratio	9.0
Fuel	Hydrogen
Fuel overall equivalence ratio, Φ	0.3;0.5;0.7;0.9
Fuel Injection pressure	5 MPa
Intake valve close (IVC) timing	BDC
Engine speed	600 rpm
Ignition timing	TDC
Initial temperature	298 K

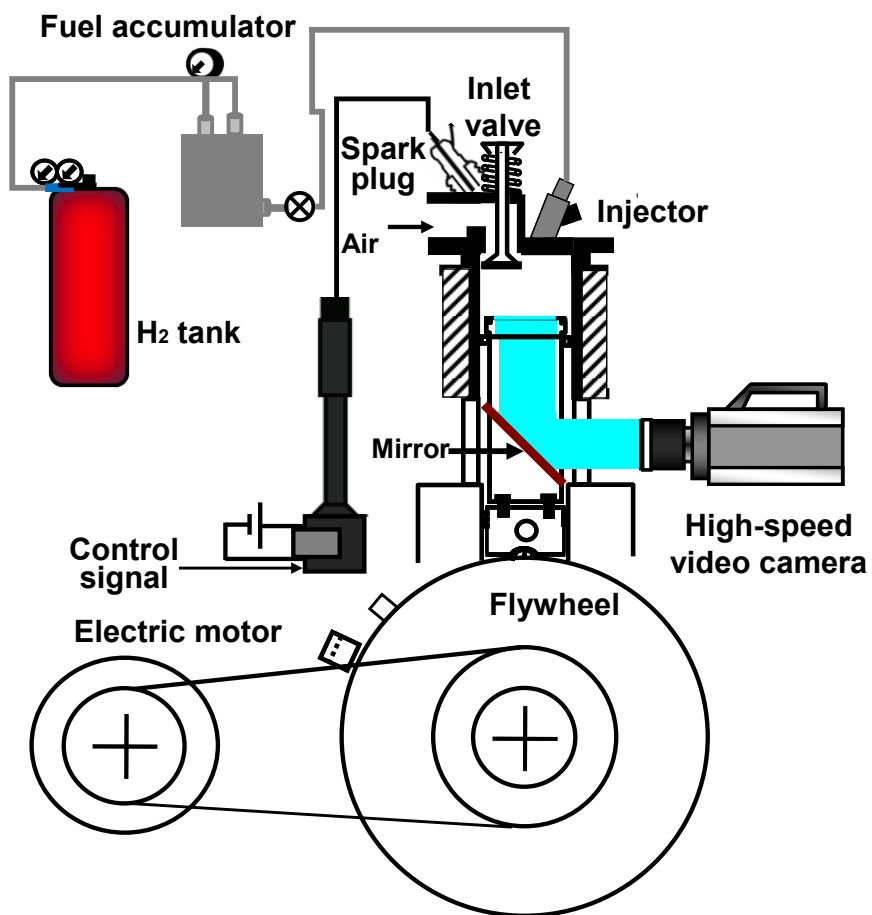
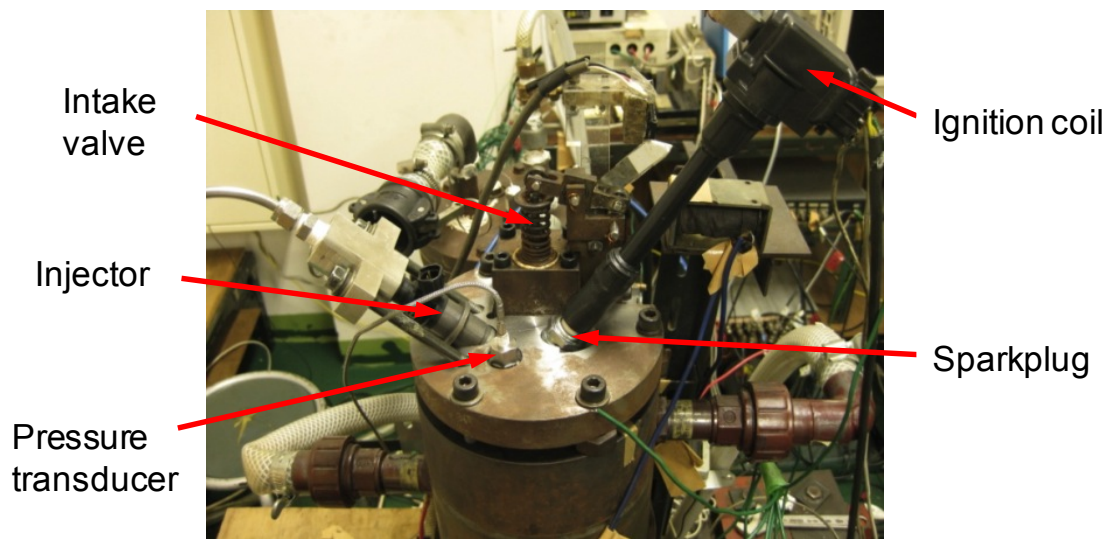


Figure 4.4 Schematic view of optical engine experimental setup

Air was initially introduced into the cylinder through an inlet valve at a pressure of 101 kPa and a temperature of 300 K. After a given amount of time, the valve was closed when the piston was located at bottom dead center (BDC). A GDI injector was used in DI engines. Fuel was supplied to the injectors from an accumulator-based system. Hydrogen was supplied from a H₂ cylinder and a fuel accumulator was used to maintain the constant fuel feed pressure to the injector. A time card ensured synchronization of the various trigger signals with the images and the data acquisition system.

4.5.2 Combustion chamber geometry

The engine configuration was designed to operate as a jet-guided system with the fuel spray targeted towards the spark plug. The piston used in this study was flat-topped. The injector was located close to the spark plug (see Figure 4.5) on the central part of the cylinder head based on the narrow-spacing concept. The inclined injector geometry directed the injected gas toward the spark plug. The distance between the injector nozzle tip and the spark plug was 15 mm.

4.5.3 Pressure instrumentation

The in-cylinder pressure was recorded using a Kistler 6052C piezoelectric transducer installed on the cylinder head. Figure 4.6 shows the Kistler pressure sensor. Type 6052C uses a piezoelectric crystal which achieves high sensitivity in conjunction with an extremely small sensor structure. This sensitivity varies by not more than $\pm 1,0\%$ in the operating temperature range. The passive acceleration compensation patented by Kistler keeps the influence of engine vibrations to a minimum. The injector was carefully cleaned and then calibrated with a dead weight tester (yielding $R^2 = 0.999998$). The heat release rate and the coefficient of variation (COV) of the indicated mean effective pressure (IMEP) were determined from the measured pressures.

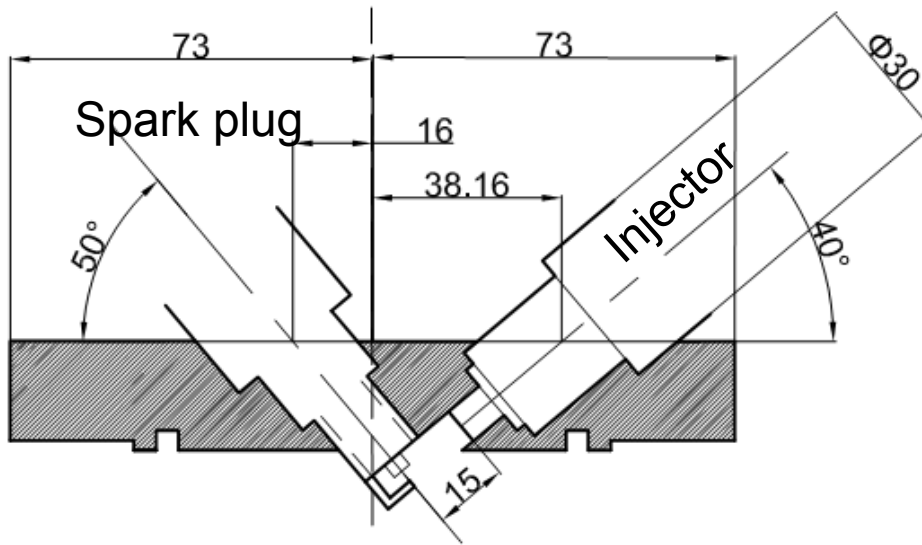


Figure 4.5 Geometric relationship between the injector and the spark plug

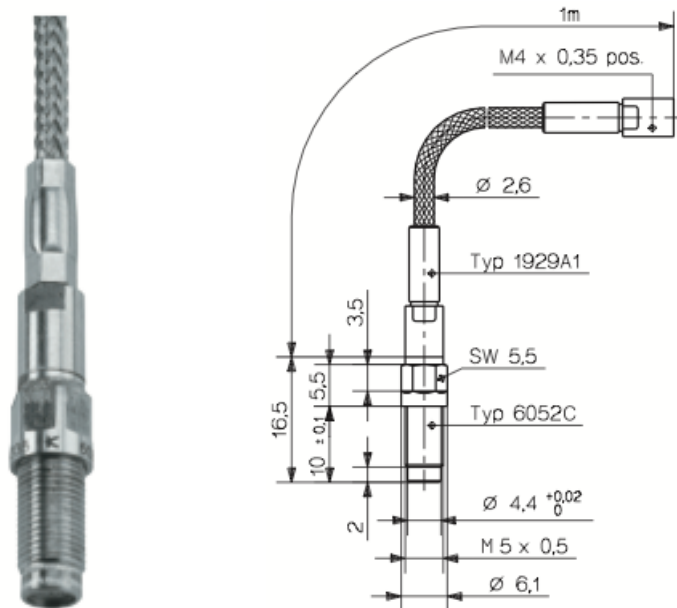


Figure 4.6 Kistler 6052C piezoelectric pressure sensor.

4.5.4 Average mass flow rate measurement

The ideal gas law was used to calculate the amount of mass injected into the chamber. The mass injected into the chamber, Δm in a single injection is given by:

$$\Delta m = \frac{(P_2 - P_1)V}{RT} \quad (4.1)$$

Where P_2 is the pressure after injection and P_1 is the initial pressure. The approximated average mass flow rate is then calculated by dividing the injected mass, Δm , by the injection duration. The fuel injector was a GDI swirl injector and the injection pressure was maintained at 5 MPa. The relationship between the fuel injection duration and the overall equivalence ratio, Φ , is shown in Fig. 4.7.

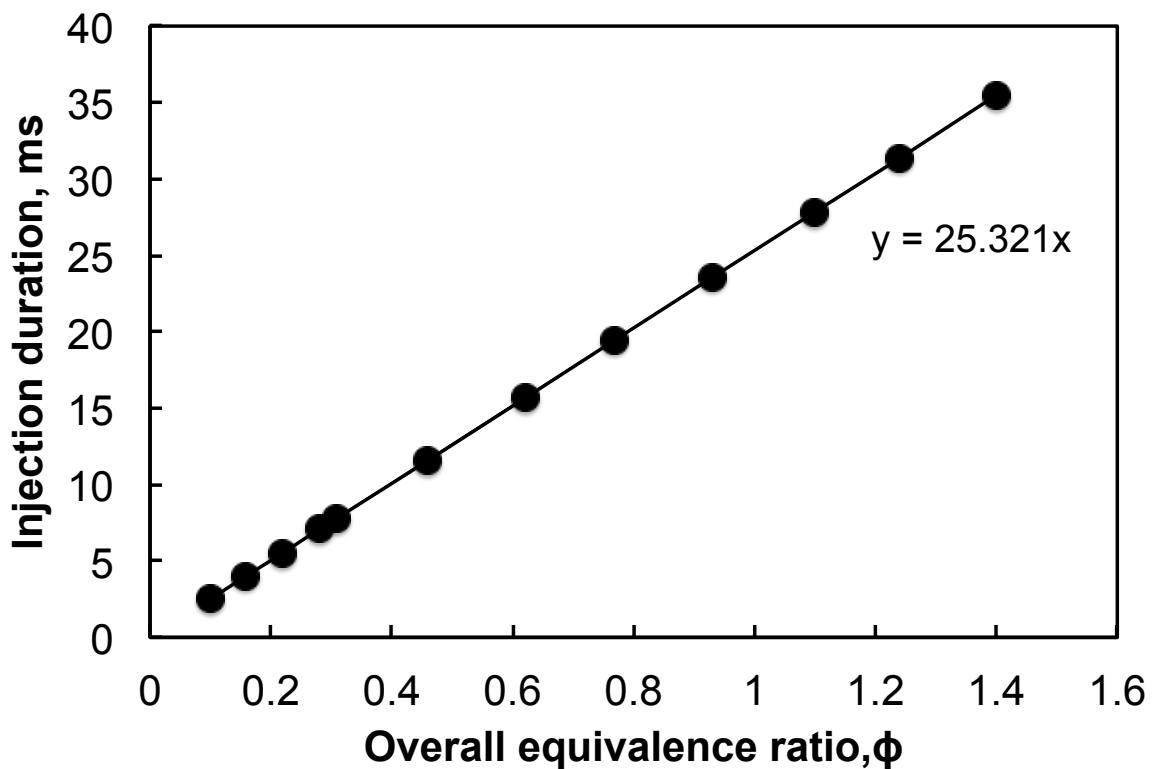


Figure 4.7 Injection duration vs overall equivalence ratio.

4.5.5 Combustion quality measurement

For decades researchers have been using in-cylinder pressure information to investigate the combustion processes in internal combustion engines. The in-cylinder pressure data provides an effective and easy way to monitor and analyze the combustion process on a cycle-to-cycle basis. Current piezo-electric transducer technology offers fast response sensors that easily withstand the harsh environment within the combustion chamber of an internal combustion engine. Voltage signals from the piezo-electric transducer and associated charge amplifier can be sampled and recorded by high speed digital data acquisition systems that are triggered by a crankshaft mounted encoder.

The development of the cylinder pressure in an internal combustion engine is a complex process that involves the heat release from the combustion, heat transfer due to convection, conduction, and radiation, as well as the changing combustion chamber volume. Parameters such as the peak or maximum combustion pressure, the crank angle where the maximum pressure occurs, ($\theta_{P_{max}}$) and the indicated mean effective pressure (IMEP) can be directly inferred from the in-cylinder pressure data. These combustion parameters are based on the combination of the cylinder pressure data with thermodynamic models. Quantitative measures of the combustion quality can be developed from the use of the in-cylinder pressure data with the cylinder volume and the derivatives of these thermodynamic models. The combustion data that can be extracted from the measured parameters include the heat release rate, ignition delay, and the combustion duration.

The mean effective pressure (MEP) is an important measure of engine performance, because it is relatively invariant with respect to engine size, and it is an excellent measure of the overall performance of the engine. By definition the mean effective pressure is the work produced per unit displaced engine combustion cylinder and is shown in Equation,

$$MEP = \frac{W_c}{V_d} \quad (4.2)$$

Where W_c is the work per cycle and V_d is the displaced volume of the engine. The IMEP is derived from the in-cylinder pressure data and is defined as the work delivered to the piston by the combustion gases during a given engine cycle per unit displaced volume. This quantity

neglects all losses (frictional, heat losses, etc.) and measures only the PdV work delivered to the piston. Pumping losses during the intake and exhaust strokes are neglected. The net $IMEP$ is defined in Equation 4.3,

$$IMEP = \frac{\int_{-\pi}^{\pi} P dV_{cyl}}{V_d} \quad (4.3)$$

where P is the in-cylinder pressure and dV_{cyl} is the differential change in volume. Because the cylinder pressure data is discretely sampled, the integral given in Equation 4.2 can be simplified into a summation of the pressure data collected throughout the compression and expansion strokes. This is possible because the in-cylinder pressure data is discretely sampled as a function of the crank angle. This transformation is shown in Equation 4.4 .

$$IMEP = \frac{\sum_{\theta=-\pi}^{\theta=\pi} P \frac{dV_{cyl}}{d\theta} d\theta}{V_d} \quad (4.4)$$

The resolution of the encoder used to trigger the data acquisition system has been used as the differential change in crank angle, $d\theta$.

The rate of heat release is an excellent means by which to characterize the combustion process. Cylinder pressure data can be used to approximate the heat release rate by treating the combustion chamber as a closed system of varying volume during combustion. By neglecting heat transfer and the effects of the crevice volumes, an energy balance on the combustion chamber volume yields the expression in Equation 4.5:

$$\frac{dQ_{chem}}{d\theta} = \left(\frac{1}{\gamma-1}\right) V_{cyl} \frac{dP}{d\theta} + \left(\frac{\gamma}{\gamma-1}\right) P \frac{dV_{cyl}}{d\theta} \quad (4.5)$$

where $dQ_{chem}/d\theta$ is the rate of change with respect to crank angle yields an expression for the heat release rate as a function of the measured pressure, volume, incremental amount of chemical energy released, P is the cylinder pressure, dV_{cyl} is the differential change in the cylinder volume, and γ is the ratio of specific heats. The ratio of specific heats can be used as a constant or it can be estimated as a function of temperature throughout the combustion

process. The heat release rate can also be integrated and normalized to yield a measure of the burned gas fraction. The importance of the heat release rate is the direct link between the measured cylinder pressure data and the actual cycle resolved combustion events.

4.5.6 Optical Access

The single-cylinder engine was optically accessible through a Bowditch-type piston. A Bowditch elongated piston equipped with a 52 mm-diameter quartz window in the piston crown was used to provide optical access inside the combustion chamber. A camera pointed towards a stationary mirror at a 45° angle situated in the center of the piston. The mirror allowed the camera to view the combustion chamber through a quartz window in the piston cap insert. An exemplary photo in Fig. 3 describes the viewable area through the piston window where injector is located at the top of the image.

4.5.6.1 High-Speed combustion image acquisition

Direct photography of the flame combustion was acquired through a 45° mirror mounted in the extended piston with a Photron FASTCAM SA1.1 (12 bit) CMOS (Complementary Metal-Oxide Semiconductor) camera. Figure 4.9 shows the high-speed video camera which was used in our experiment. The Photron FASTCAM SA1.1 will meet the imaging requirements of the most demanding applications in research and development due to its unrivalled sensitivity, speed and resolution. The FASTCAM SA1.1 uses the latest CMOS sensor to achieve sensitivity and speeds previously unattainable. FASTCAM SA1.1 release of this camera delivers megapixel resolution with a top speed in excess of 600,000 fps (frames per second) and with true 12-bit dynamic range. The lens was a 50 mm, f/1.5 Nikon, and the frame resolution was 384×320 pixels² at 40,000 frames per second. Combustion was initiated by the spark and the flame propagation to the maximum optical area stage capture varied between 21 and 100 images, depending on the equivalence ratio, injection timing, and ignition regime.

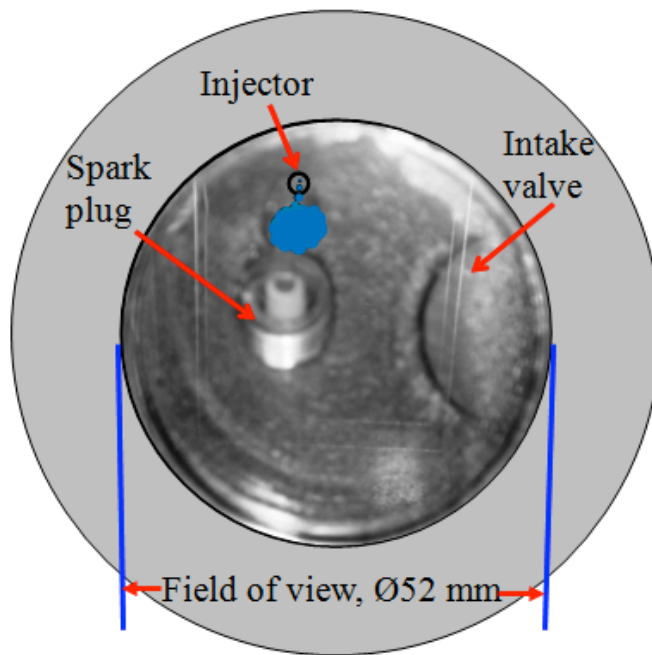


Figure 4.8 Viewable area through the piston window



Figure 4.9 Photron FASTCAM SA1.1 (12 bit) CMOS type camera.

4.5.7 Operating conditions

Experiments were conducted in a single-cylinder SI engine. The fuel injector was a GDI swirl injector and the injection pressure was maintained at 5 MPa. Air was introduced into the cylinder through the inlet valve at an initial pressure of 0.1 MPa and temperature of 298 K. The indicated mean pressure was measured throughout the cycle. The fuel-air mixture was ignited at TDC by the centrally-offset spark electrode. The four ignition modes at an overall equivalence ratio of 0.22 were categorized as shown in Figure 4.10 and can be summarized as follows.

1. Tail Ignition (TI): Hydrogen is injected during the compression stroke and ignites at the end of the injection (EOI) period. Start of injection (SOI) is at a 332° CA (variable) and the EOI is at TDC.
2. After Tail Ignition (ATI): Hydrogen is injected during the compression stroke, and the EOI is at a 5° CA before TDC. Ignition occurs at TDC. The SOI is at a 327° CA (variable) and the EOI is at a 355° CA.
3. Center Ignition (CI): Hydrogen is injected during the latter portion of the compression stroke and ignites at TDC so that combustion occurs between the SOI and EOI. The SOI is at a 343° CA (variable) and the EOI is at a 382.5° CA.
4. Head Ignition (HI): Hydrogen is injected during the latter part of the compression stroke and ignites at TDC, close to the start of injection. The SOI is at a 355° CA and the EOI is at a 394.5° CA.

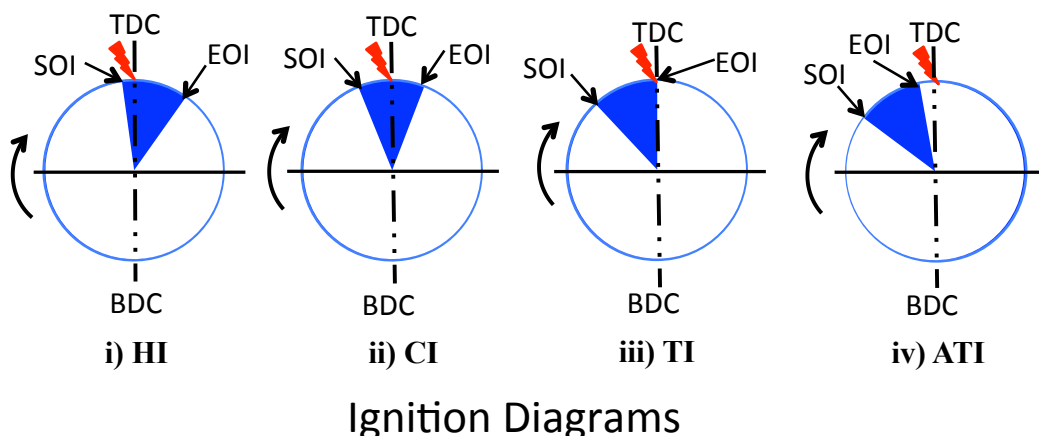


Figure 4.10 Diagrams showing the fuel-injection timing relative to the ignition timing.

4.6 Experimental results

4.6.1 Effect of injection timing relative to ignition timing

The results are shown in comparison with the combustion characteristics obtained for four different ignition modes. Time-series spark-ignited combustion images along with the typical pressure histories and the rate of heat release (ROHR) for different ignition timings at overall equivalence ratio, ϕ of 0.1 to 0.28 are shown in Fig. 4.11 to Fig. 4.14. The in-cylinder pressure gradually increases with the increase of overall equivalence ratio due to stratified mixture formed near the spark plug. For an overall equivalence ratio of 0.1, the lean mixture induced a low in-cylinder pressure with a slow-burning heat-release profile. For TI, where ignition occurred during the end of the injection period, a rapid increase in pressure just after ignition was observed, with a maximum peak ROHR. The ATI ignition mode allowed a 5° CA after the EOI for the injected gas to mix and settle before ignition. A medium peak combustion pressure was observed compared to the other ignition modes; the heat release rate increased smoothly to a maximum and then progressively decreased as the entire mixture was consumed. For CI, in-cylinder combustion pressure was lower compared to TI and ATI. The ROHR for CI was faster in the initial stage, but slower burn in the later stages, indicating diffusive phase combustion. For HI mode, ignition timing at the early stage of SOI, resulting in reducing the in-cylinder pressure with a low burning rate. The second part of ROHR for HI mode indicates the diffusive phase like combustion as well as in CI mode. Figure 4.11 to Fig. 4.14 shows that TI mode combustion had faster burning rate compared to the other ignition modes and thereby increases the combustion efficiency.

Photographs combined with thermodynamic data provide an effective tool for combustion analysis. Combustion images of the four different ignition modes are shown for the spark discharge and flame propagation periods. Some additional luminosity was observed during flame growth, perhaps due to combustion of the lubricating oil [84]. The intensity of the flame was relatively weak at a small overall equivalence ratio. The flame kernel initialized from the center-off of the combustion chamber, and the flame front propagates across the cylinder. Flame photographs at an overall equivalence ratio of $\phi = 0.16$ are shown in Fig. 4.11 to Fig 4.14; the flame propagation exhibited a trend similar to that at $\phi = 0.1$. However, the intensity of the flame was stronger than at $\phi = 0.1$, suggesting that with the increased

equivalence ratio, a higher degree of mixture stratification occurred near the spark electrode gap at ignition. Moreover, the high flame intensity induced by a high gas temperature during the combustion process, which was expected since the amount of fuel increases with the overall equivalence ratio.

For TI timing mode, the results presented in Fig. 4.11 to Fig. 4.14 shows an initial early kernel growth after the spark discharge as the rapid flame propagated through the combustion chamber. Pictures of the initial combustion phase indicate an initial quasi-spherical and later partially wrinkled flame. When the flame kernel becomes larger than the smallest turbulent eddies, the flame front will become wrinkled [96]. For ATI, the flame travelled a short distance from the spark-plug center, as shown in Fig. 4.11 to Fig. 4.14. It has been known that the hydrogen jet injection produced turbulence flow field in the surrounding air, which resulted in turbulent combustion during the initial phase of CI. For the HI, combustion images were found with very weak flame intensity. The flame propagation indicated that the mixture, which was ignited during the fuel injection, behaved quite differently from when ignition occurred after the termination of the injection. Two possible reasons exist to explain this phenomenon: the first relates to the degree of charge stratification of the mixture, and the second relates to the decay of the turbulence generated by the hydrogen jet.

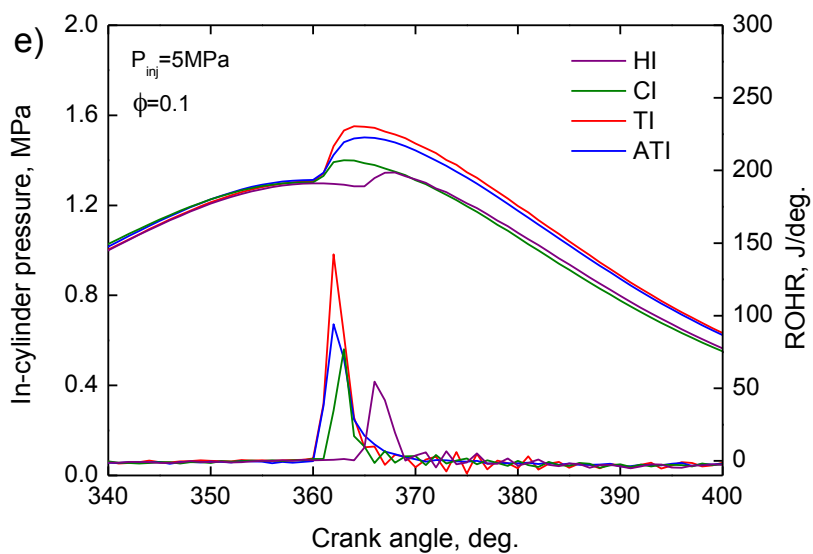
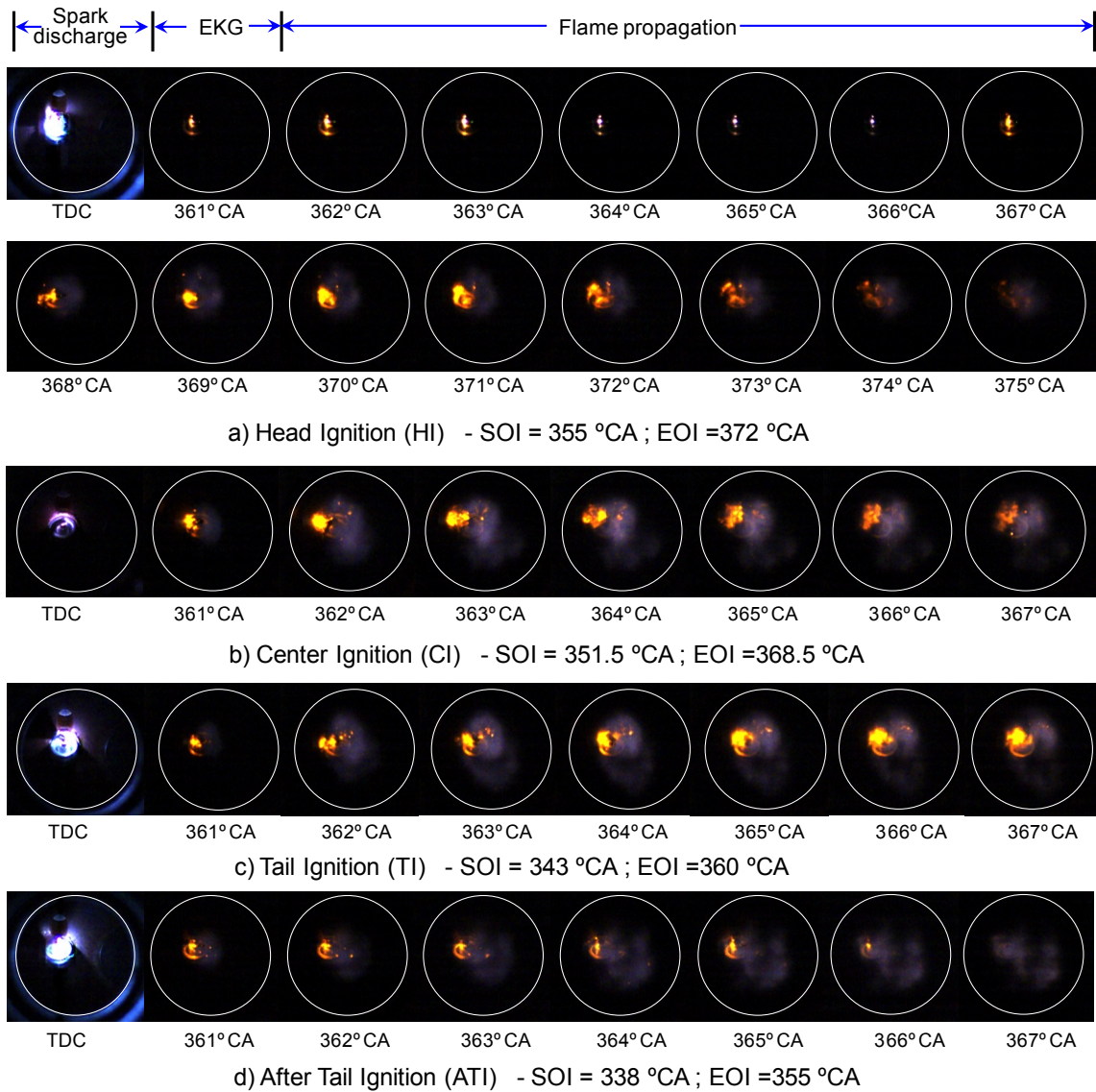


Figure 4.11 Time-series combustion images and typical in-cylinder pressure history along with ROHR at different ignition modes. ($\Phi=0.1$)

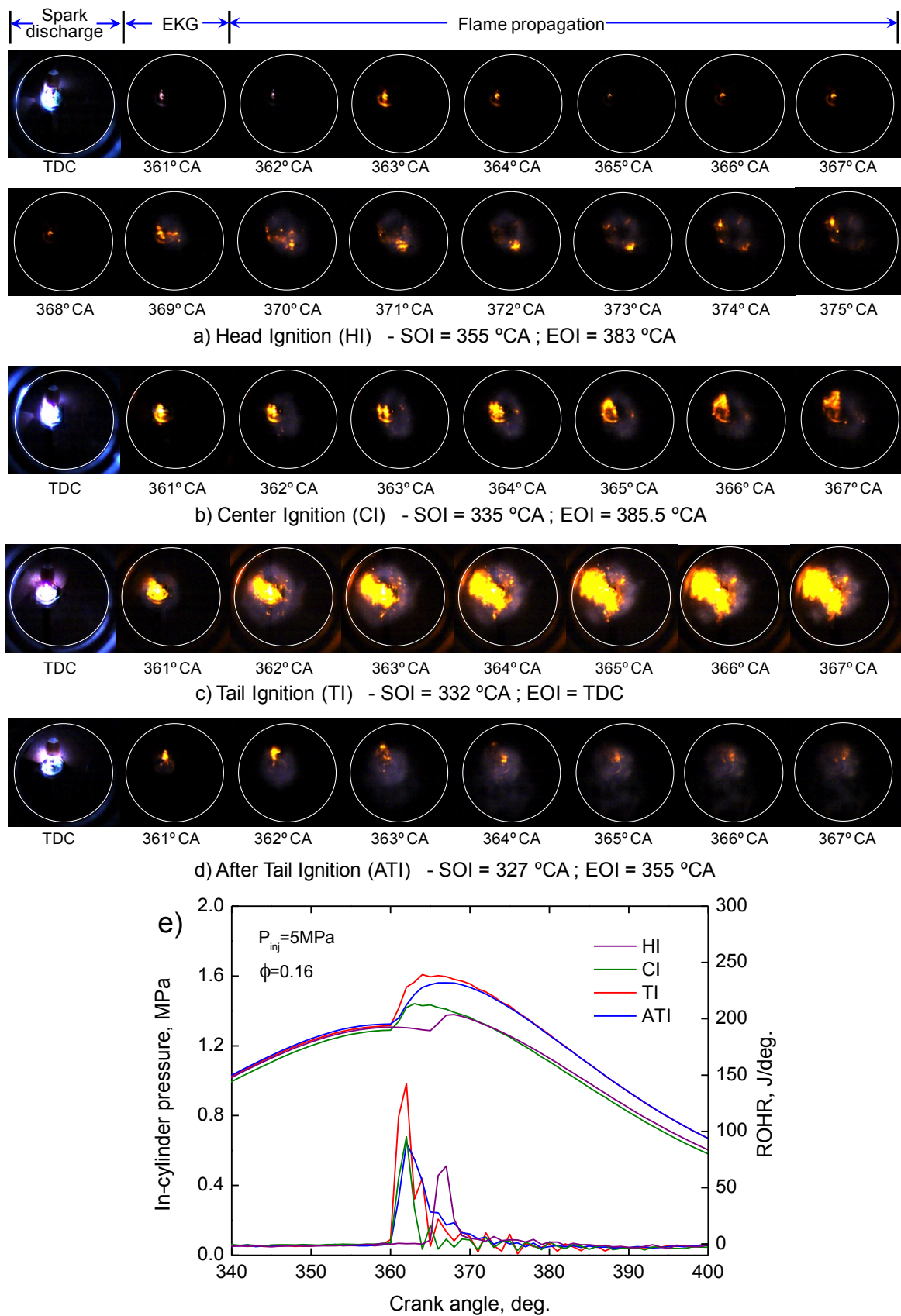


Figure 4.12 Time-series combustion images and typical in-cylinder pressure history along with ROHR at different ignition modes. ($\Phi=0.16$)

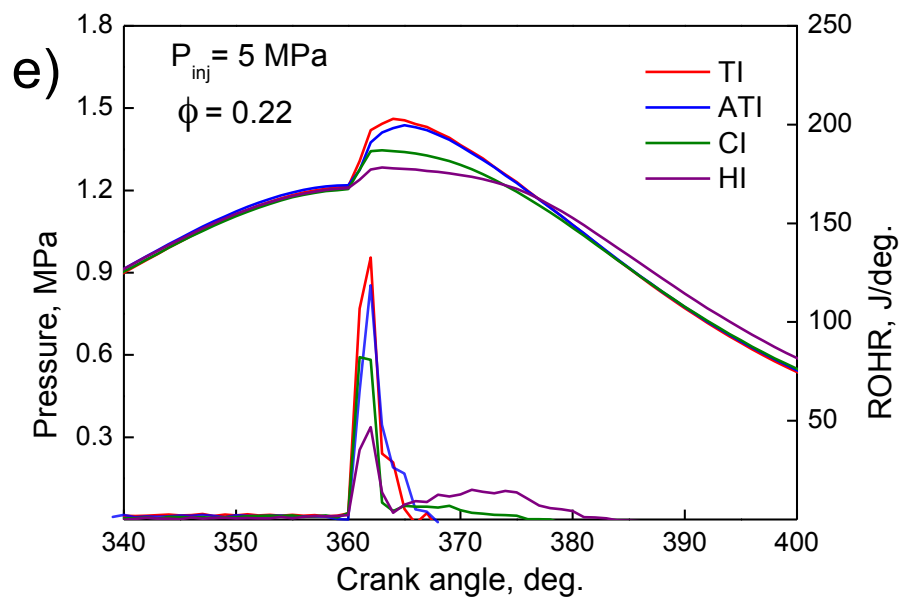
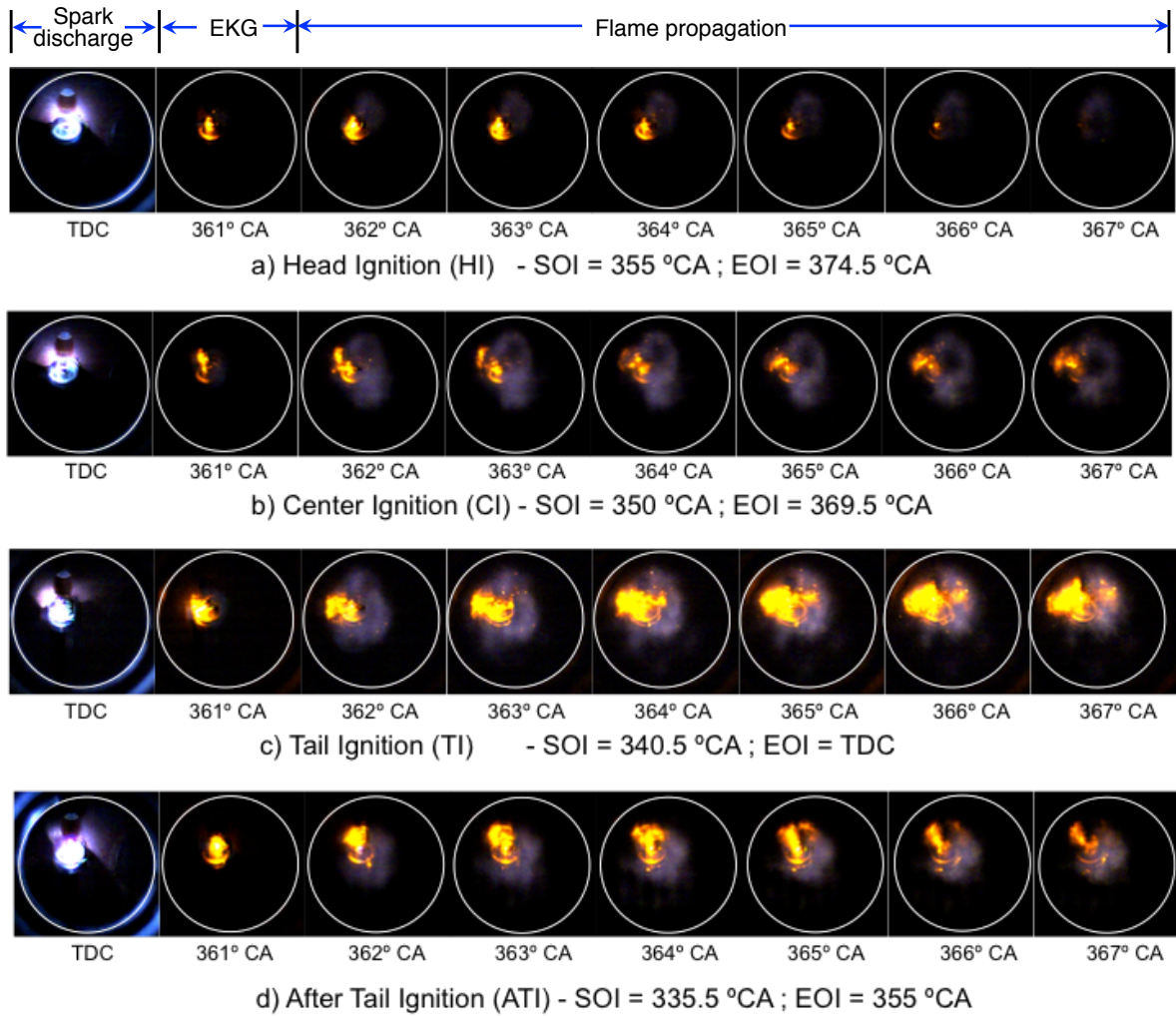


Figure 4.13 Time-series combustion images and typical in-cylinder pressure history along with ROHR at different ignition modes. ($\Phi=0.22$)

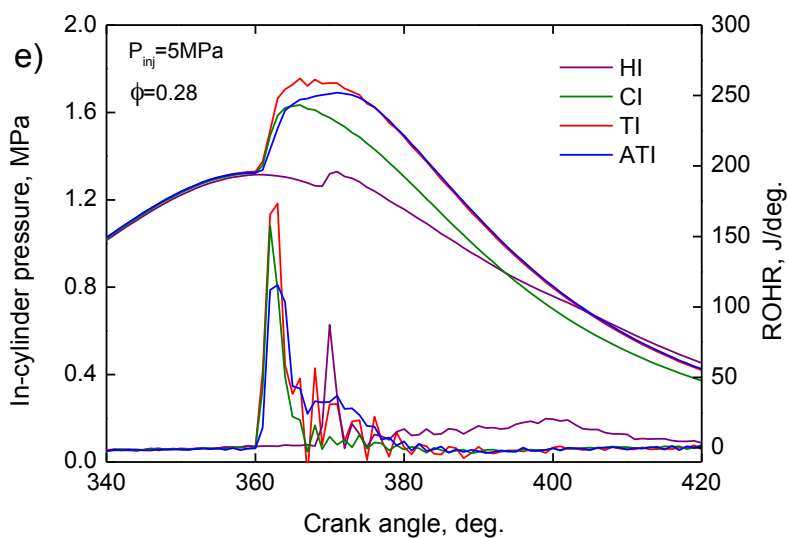
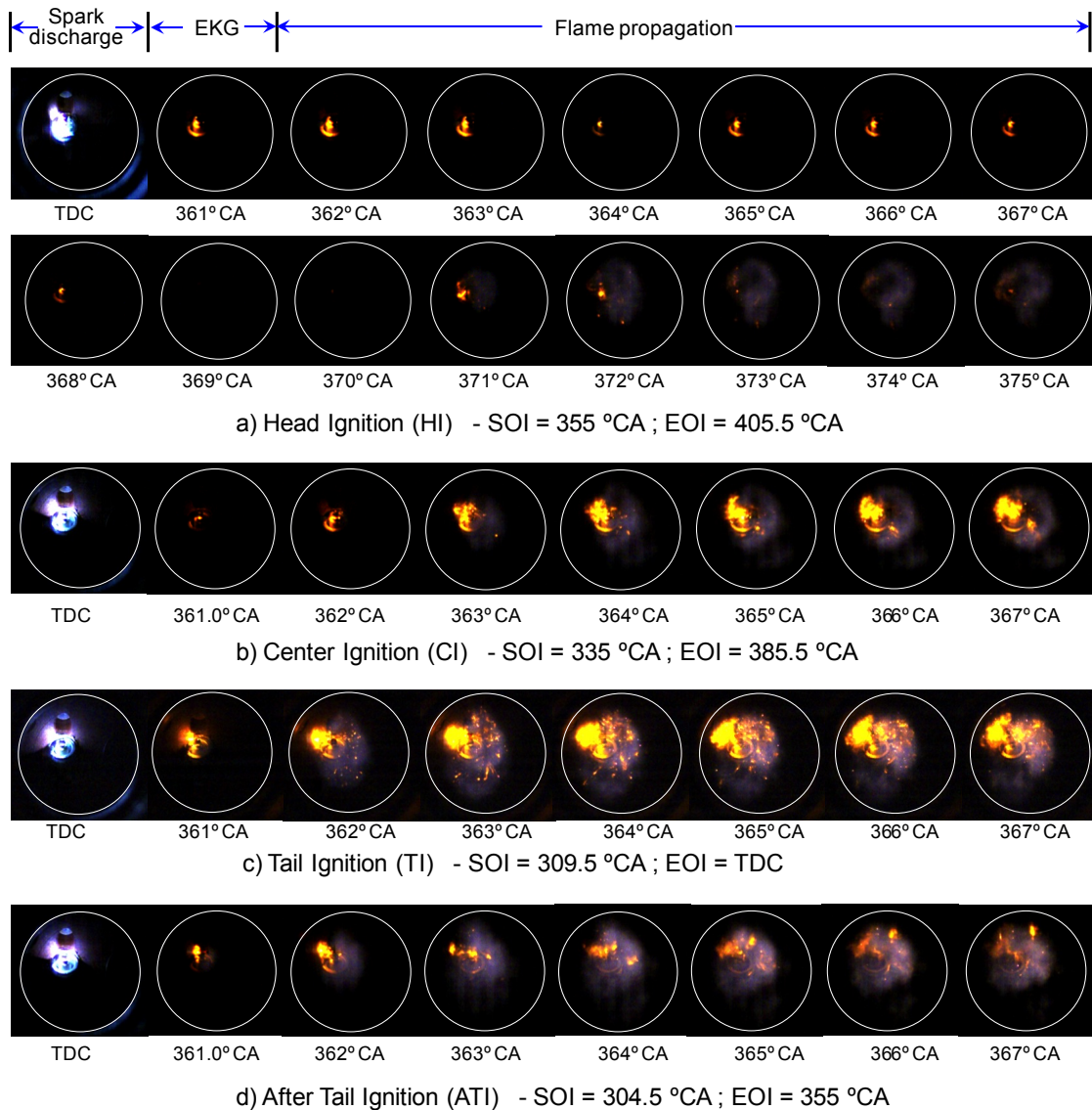


Figure 4.14 Time-series combustion images and typical in-cylinder pressure history along with ROHR at different ignition modes. ($\Phi=0.28$)

4.6.2 Mass fraction burn for different ignition modes

The fuel burn fraction is plotted against CA for the four-ignition modes combustion under different equivalence ratio, as shown in Fig. 4.15. The Rassweiler model is used to identify the mass fraction burn of hydrogen and positive value of fuel fraction burn is observed after TDC ignition. Figure 4.15 show the thermodynamically derived mass fraction burned (MFB) for the four different injection modes at different equivalence ratio. Different points such as combustion phasing, rapid-burn duration, and flame development duration during the combustion process can be used to evaluate the differences in combustion for the different ignition mode. Combustion phasing, θ_{50} , gives the crank angle degrees at which 50% of the fuel mass has been burned. The duration from spark discharge to when a small but noticeable amount of the fuel is burned is called the flame development duration denoted by 0 to 5% or 10%. MFB 5% is considered to be a robust indicator of the beginning of hydrogen combustion. The positions of MFB 5% in Fig. 4.15 a) are almost identical for CI, TI and ATI combustion except HI combustion.

The 10%-90% burn duration denoted as $\Delta \theta_{10-90}$ gives a measure of flame propagation rate, and is connected with efficiency. This makes sense, as the higher flame propagation rate ends combustion earlier in the expansion process and increases the peak cylinder pressure. Figure 4.15 a) shows that the burn duration, Δ_{10-90} for TI combustion is about 1° - 2° earlier than for ATI combustion. The rapid burn duration gives an indication of the speed of the flame. In CI combustion, there were fast burn rates at the initial stage and slower burning at the later stage. The faster initial combustion in CI mode might be due to rapid burn of the initial mixture due to higher turbulence, while a slower burn in the later stage due to diffusion. The flame propagation indicated that the mixture, which was ignited during fuel injection, behaved quite differently from that when ignition occurred after the termination of injection.

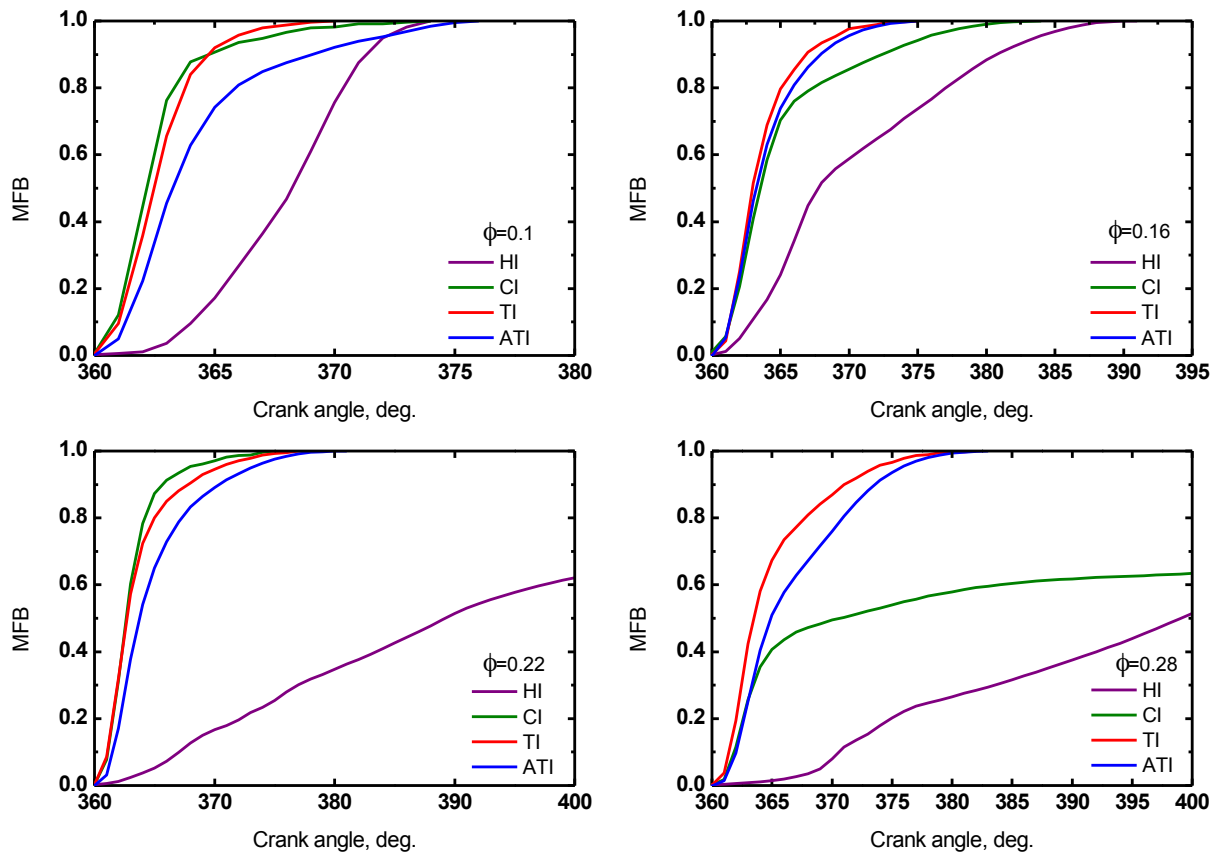


Figure 4.15 MFB for different ignition modes under different overall equivalence ratio.

4.6.3 Combustion stability measurements

Figure 4.16 shows the IMEP at different equivalence ratios in the different ignition mode combustion. The IMEP increases gradually with equivalence ratio and reaches a maximum at an approximately stoichiometric mixture. Due to dissociation at high temperatures following combustion, molecular oxygen is present in the burned gases under stoichiometric conditions. The effect of increased temperature and increased number of moles of burned gas in the cylinder was to increase the IMEP. Here, IMEP reached a maximum at an overall equivalence ratio of 0.28. Hydrogen has a wide flammability limit, making it possible to use very lean mixtures. The present results indicate that a more practical lean limit for combustion in engines is around 0.1. The use of lean mixtures in a hydrogen-fuelled engine not only results in fuel economy but also opens up the possibility of controlling the power output of the engine by changing the fuel flow rate while keeping the airflow unthrottled.

The COV of IMEP, which is defined as the standard deviation of the IMEP divided by the mean IMEP [35], is a good measure of the combustion stability. Cycle variation in a SI engine results from the change in the mean effective pressure caused by combustion variation, which is brought about by variation in the flow of the fuel–air mixture at the time of ignition. The turbulence inside the engine due to piston motion and hydrogen jet at the moment of the discharge stretches the plasma channel. This stretching effect has two consequences. The first one is that as the intensity of the turbulence increases, a higher current is needed to keep the plasma channel attached to the spark plug, otherwise the plasma would detach and possibly re-strike provided that enough energy was still available in the electrical circuit. The second effect is that as the turbulence intensity increases it also increases the heat loss by convection from the plasma channel and therefore reduces its temperature [76].

The COV of the IMEP for the four ignition modes is shown in Figure 4.17. The COV of IMEP for TI mode was about or below 7% at overall equivalence ratio $\phi=0.22$ and $\phi=0.28$ respectively, indicating that the combustion was relatively stable. This was attributed to sufficient hydrogen being in the vicinity of the spark plug to create an ignitable mixture, which could burn reliably, as observed in direct combustion images. The other three ignitions modelled to the large cycle-by-cycle variations. The ATI mode showed quite unstable combustion except $\phi=0.28$ because at early injection timing, where the in-cylinder pressure is relatively low, the gas jet travels further from the spark plug, causing less effective burning. Further ignition during the midpoint of the injection period for CI mode, caused the COV of the IMEP to increase by more than 18%. CI mode combustion had become unstable, as a heterogeneous fuel–air mixture formed due to short mixing time. The COV of IMEP for the HI mode was over 13%. The HI mode showed very unstable combustion due to the shortening of the mixing time of the hydrogen jet and air since the ignition timing was set closer to the SOI. The results suggest that the TI mode at overall equivalence ratio $\phi=0.22, 0.28$ gives the relatively stable operation of the ignition modes considered here.

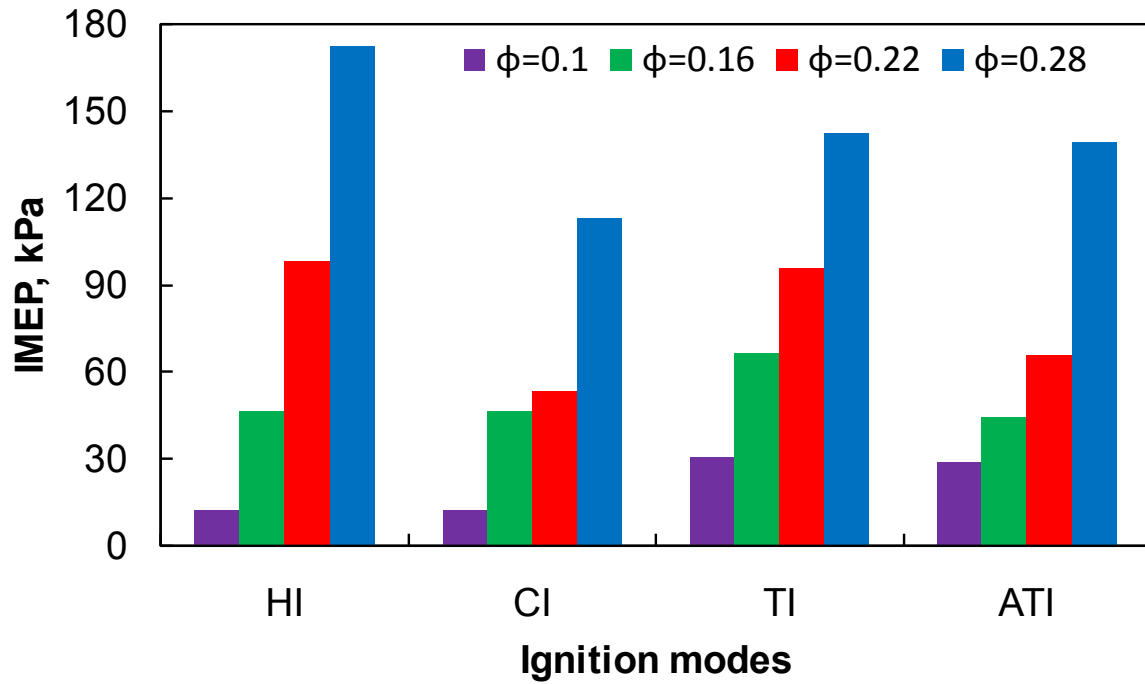


Figure 4.16 IMEP at different ignition modes combustion.

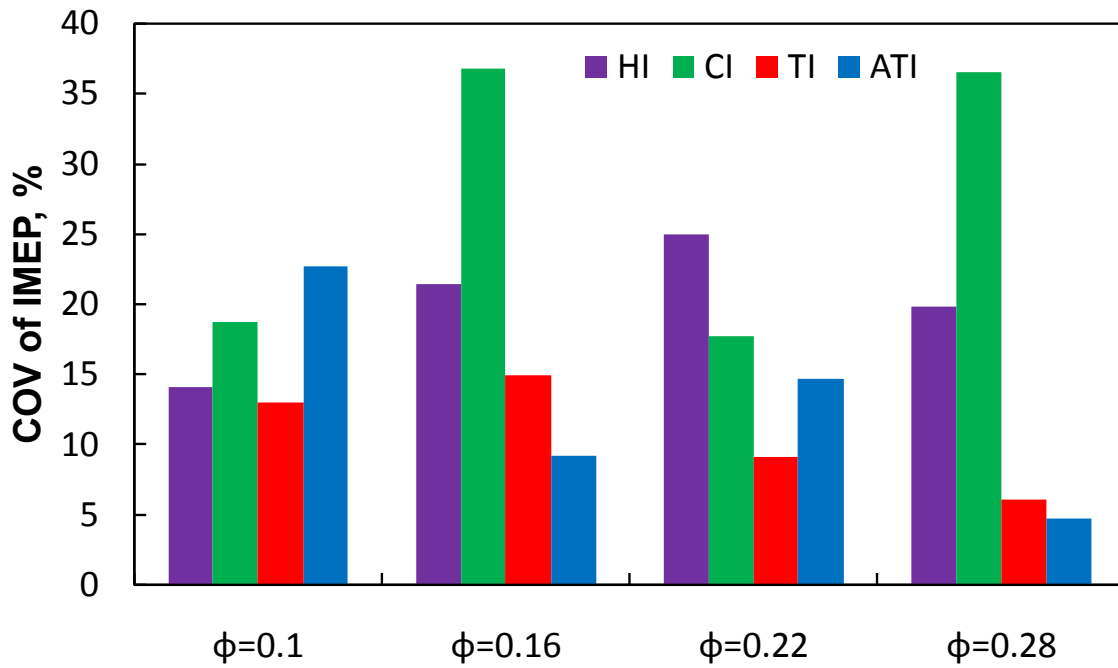


Figure 4.17 COV of IMEP at different equivalence ratio.

4.6.4 Combustion images analysis

Image digitization of the flame area was carried out to obtain quantitative information from the combustion process. To determine the flame area per degree crank angle, images were binarized and the pixel intensities were summed. In this experiment, cycle-averaged flame areas were computed based on the chemiluminescence flame intensity up to the maximum travel within the cylinder. Some additional flame luminosity was also observed during very fast flame growth; this may have been due to combustion of the lubricating oil. Additional bright luminous intensity that was produced in combustion was eliminated while measuring the area by the image processing. Figure 4.18 a)-b) shows the maximum flame area growth, for the four different injection modes at different overall equivalence ratio. Different points such as combustion phasing, rapid-burn duration, and flame development duration during the combustion process can be used to evaluate the differences in combustion for the different ignition mode. Combustion phasing, θ_{50} , gives the crank angle degrees at which 50% of the fuel mass has been burned. θ_{50} for TI exhibits earlier combustion phasing with compared to the other ignition modes. Similar trend can be notice in Fig. 4.18 that the measured flame area for TI timing being reached closer to maximum value at 50% burned point. Ashurst [77] reported that the distorted flame exhibits exponential growth until about half of the mass is consumed, at this point the burnt gas appears to almost nil the chambers. Moreover, flame growth was faster for the spark at EOI in TI combustion when compared to the direct combustion images of section 4.8.

Figure 4.19 shows the maximum flame area growth with the second derivative of the flame area, $d^2A/d\theta^2$, for the four different injection modes with an overall equivalence ratio of 0.22. This figure represents the timing and the duration of the early kernel growth and the maximum flame period. Theoretically, early kernel growth (EKG) is the period after the spark discharge where a small reaction kernel exists. As electrical energy is fed into the discharge, the arc expands and exothermic chemical reactions capable of sustaining a propagating flame develop. Reuss et al. [78] proposed a model whereby the end of the early kernel growth rate (EOEKG), is defined as the crank angle where the second derivative of the flame area, $d^2A/d\theta^2$, is a maximum and occurs at the beginning of the flame propagation (Fig. 4.19). A similar

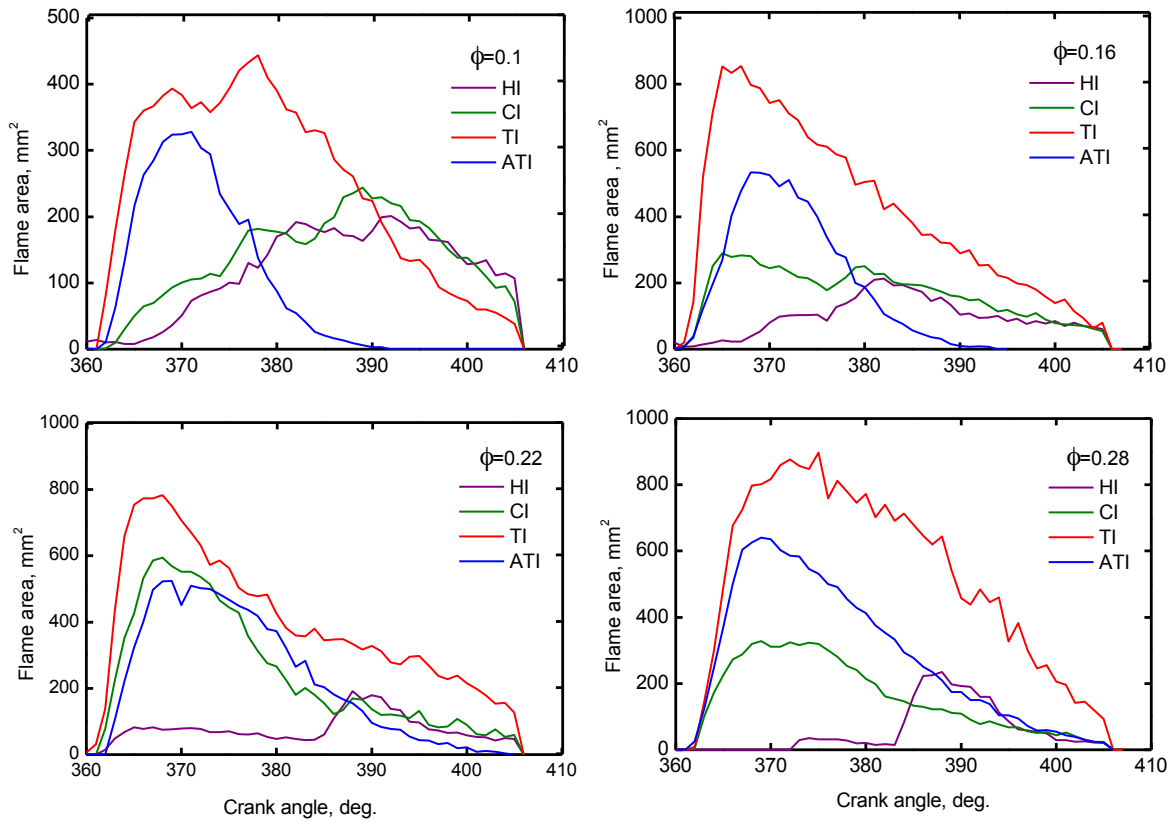


Figure 4.18 Average flame area at different ignition modes combustion.

model was described by Abraham et al. [79] based on a homogeneous SI engine where the ignition kernel grows slowly on a laminar-flame time scale, and then the transition to rapid growth occurs on a turbulent-flame scale. The TI combustion mode at an overall equivalence ratio of 0.22 had a faster growth EKG and a larger maximum flame area than the ATI and CI combustion modes. This can be explained using the same argument as for the ROHR analysis. The faster initial flame development can indicate a faster burning rate, and the HI combustion mode showed a slower EKG and a smaller maximum flame area. In addition to the flame development being slower, the ROHR throughout the combustion process was lower. Finally, there was a good relationship between the in-cylinder EKG rate and flame area, allowing measurements of flame behaviour for different levels at different crank angles.

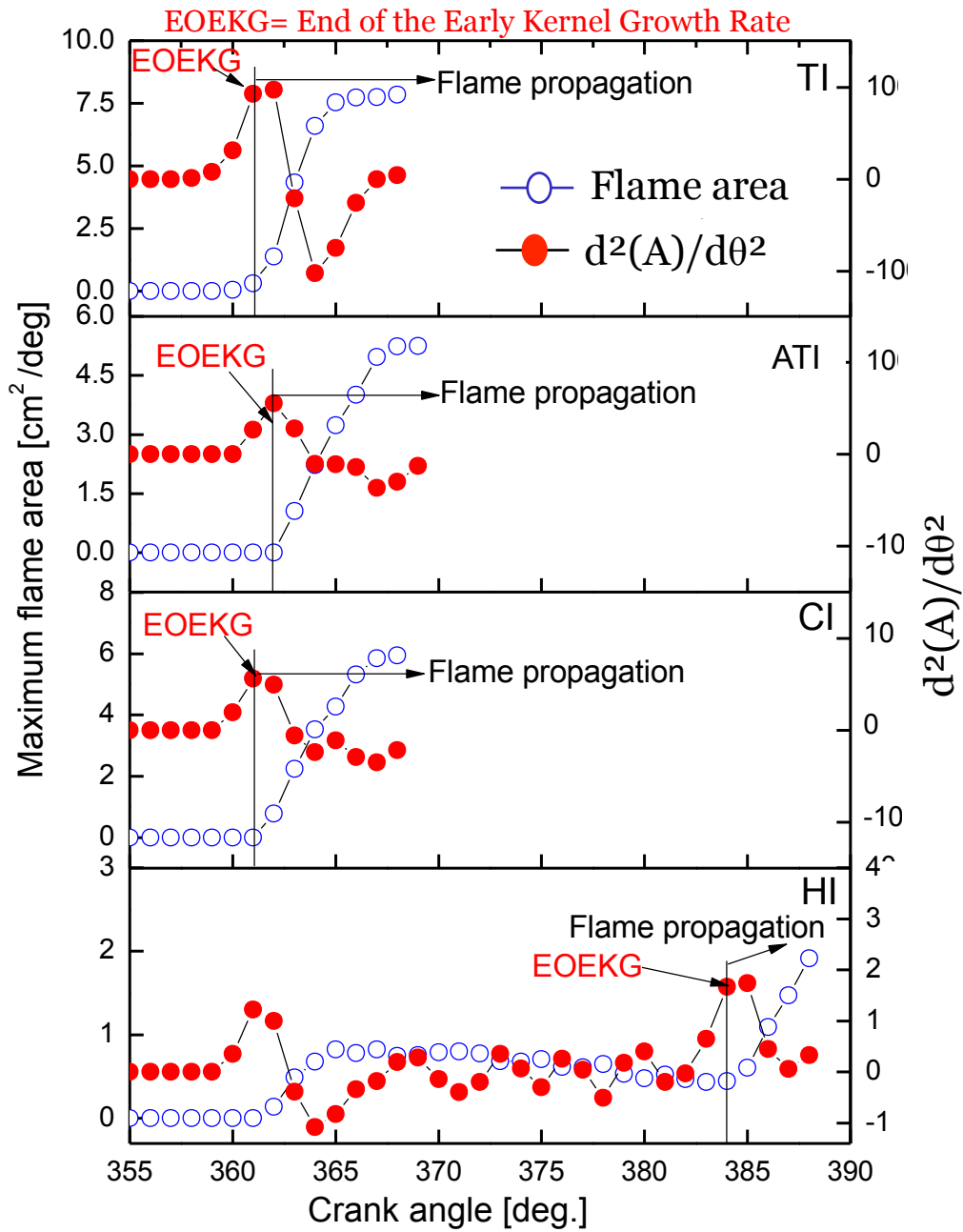


Figure 4.19 Average flame area and early kernel growth rate (EKG) at an equivalence ratio of 0.22 under different injection modes. The open circle symbols indicate the area growth rates and the solid circle symbols show the double derivative of the flame area with respect to each crank angle (EKG rate)

4.7 Summary

Chapter 4 described the combustion characteristics of the hydrogen jets, which can be controlled by varying the fuel injection timing. Four injection timing combustion modes were studied. The conclusions found in this chapter are given as follows.

1. The Tail Ignition (TI) mode, whereby injection is terminated at the instant of the spark ignition, resulted in sufficient hydrogen being present in vicinity of the spark plug to create an ignitable mixture at the EOI. TI mode combustion had faster burning rate compared to the other ignition modes and thereby increases the combustion efficiency.
2. For CI, in-cylinder combustion pressure was lower compared to TI and ATI. The ROHR for CI was faster in the initial stage, but slower burn in the later stages, indicating diffusive phase combustion. For HI mode, ignition timing at the early stage of SOI, resulting in reducing the in-cylinder pressure with a low burning rate.
3. Pictures of the initial combustion phase indicate an initial quasi-spherical and later partially wrinkled flame. The flame intensity was stronger with the increased of equivalence ratio, means a higher degree of mixture stratification occurred near the spark electrode gap at ignition. Moreover, the high flame intensity induced by a high gas temperature during the combustion process, which was expected since the amount of fuel increases with the overall equivalence ratio.
4. The COV of the IMEP for the four ignition modes were shown in this experiment, Tail Ignition (TI) mode showed relatively stable combustion compared to other ignition modes. This engine has only one intake valve. The in-cylinder exhaust gas was drawn out by a vacuum pump through the inlet valve. There is no influence in the present study from the residual gas and charging that play the influence on the cyclic variations in a real direct-injection engine. The experimental conditions such as the temperature and pressure are also much lower than those of a real engine. Thus, the cyclic variations in the engine study only reflect the mixture formation, both local equivalence ratio and degree of mixture stratification and/or mixture inhomogeneity besides the influence from gas flow.

5 Local fuel concentration measurement

The local equivalence ratio near the spark plug at the time of the spark discharge is particularly important for successful ignition, since the jet-guided system generates a stratified fuel concentration near the spark plug in a DISI engine. The fuel concentration around the spark plug together with the fluid motion strongly influences the duration of combustion initiation. This causes cycle-to-cycle variation, which can become large in lean-burn engines[35].

5.1 Literature review

A variety of optical techniques have been used previously to measure the local fuel concentration or the fuel-air ratio in SI engines, including infrared (IR) absorption, planar laser-induced fluorescence (PLIF), Laser-induced breakdown spectroscopy (LIBS) and Raman scattering. LIF measurement has been widely used because the LIF signal is strong and provides two-dimensional fuel concentration data at a specific time. Tomita et al. [55] applied the PLIF method to study the fuel concentration distribution in the transient hydrogen jet. Results showed that each transient hydrogen jet had different configurations and concentration distributions.

Kaiser et al. [57] performed an optical study of mixture preparation in a hydrogen-fueled engine using a PLIF technique; their report favors increased injection pressure and careful nozzle design. Equivalence ratio fields for the three post-IVC injection timings are presented in Fig. 5.1. For each timing, a representative single shot, the ensemble averaged images and the corresponding root-mean-square (RMS) are shown. In Fig. 5.1 we see that for early injection in the mean the fuel is distributed uniformly. In terms of the spatial fuel distribution, the other two injection timings produce results significantly different from the early injection case. For intermediate injection timing, the sample single-shot image has a region near the injector, where on a larger scales the fuel is fairly homogeneously distributed, although with small-scale fluctuations within that region. For late injection, the fuel is even more concentrated towards the injector and there is no region of relatively uniform equivalence ratio anymore.

Blotevogel et al. [58] used a triethylamine (TEA) tracer-based LIF technique (rather than an acetone tracer) to measure mixture formation in H₂-ICE under a high-temperature and high-

pressure environment, and demonstrated a very good signal-to-noise ratio. Besides the TLIF and flame luminosity images, Fig. 5.2 also shows the cylinder pressure curve to identify the cycle position of the taken images and the behavior of the combustion process at that time. Cycle 320 in Fig. 5.2 shows the regular working cycle for this operating point. Cycles 202 and 259 are working cycles with noticeable fluctuations. The ignition spark can still be seen in the flame luminosity images (lower row) as a high-intensity spot. For Cycle 320, the TLIF image shows a good homogeneity of the hydrogen/air mixture, which becomes a little bit richer on the inlet side (left side of the images). Combustion in Cycle 259 should therefore be slower than and not as intense as in Cycles 320 and 202. The image of the flame corresponds to this; the image intensity is much lower than at Cycle 320 and also a bit lower than at Cycle 202.

Ferioli et al. [59] used LIBS on engine exhaust gas to illustrate the ability of this technique to measure the equivalence ratio of SI engines using the ratios of C/O and C/N atomic peaks derived from the measured spectra. Phuoc et al. [60] used a laser-induced spark to measure the ignition and fuel-to-air ratio of CH₄-air and H₂-air combustible mixtures simultaneously using the measured spectral peak ratio H α (656 nm)/O (777 nm). Shudo et al. [61] measured the mixture formation characteristic of hydrogen jet into constant volume chamber filled with nitrogen using LIBS techniques. Fig. 5.3 shows example spectra of atomic emissions from hydrogen-nitrogen mixture measured with LIBS and the local equivalence ratio. The peak at 656 nm is from hydrogen, while other three peaks at 745 nm, 823 nm, and 871 nm are from nitrogen. The measuring point with laser beam focus was scanned from nozzle tip to the jet direction when hydrogen was injected into the chamber. As the measuring point is moved to downstream, the peak concentration decreases more quickly with hydrogen. This indicates that hydrogen diffuses and mixes with ambient nitrogen quickly, which can be attributed to a high diffusivity of hydrogen.

Quantitative measurements of the cycle-to-cycle variations in the mixture strength at or near the ignition site are comparatively rare for practical hydrogen SI engine. Kawahara et al. [62] used a spark-induced breakdown spectroscopy (SIBS) technique to measure the influence of the H α /O intensity ratio on the hydrogen-air mixture concentration during fired engine operation. Ando et al. [63] and Fansler et al. [64] reported individual measurements of the equivalence ratio at the spark gap using the ratio of cyanogens (CN, 388 nm wavelength) and

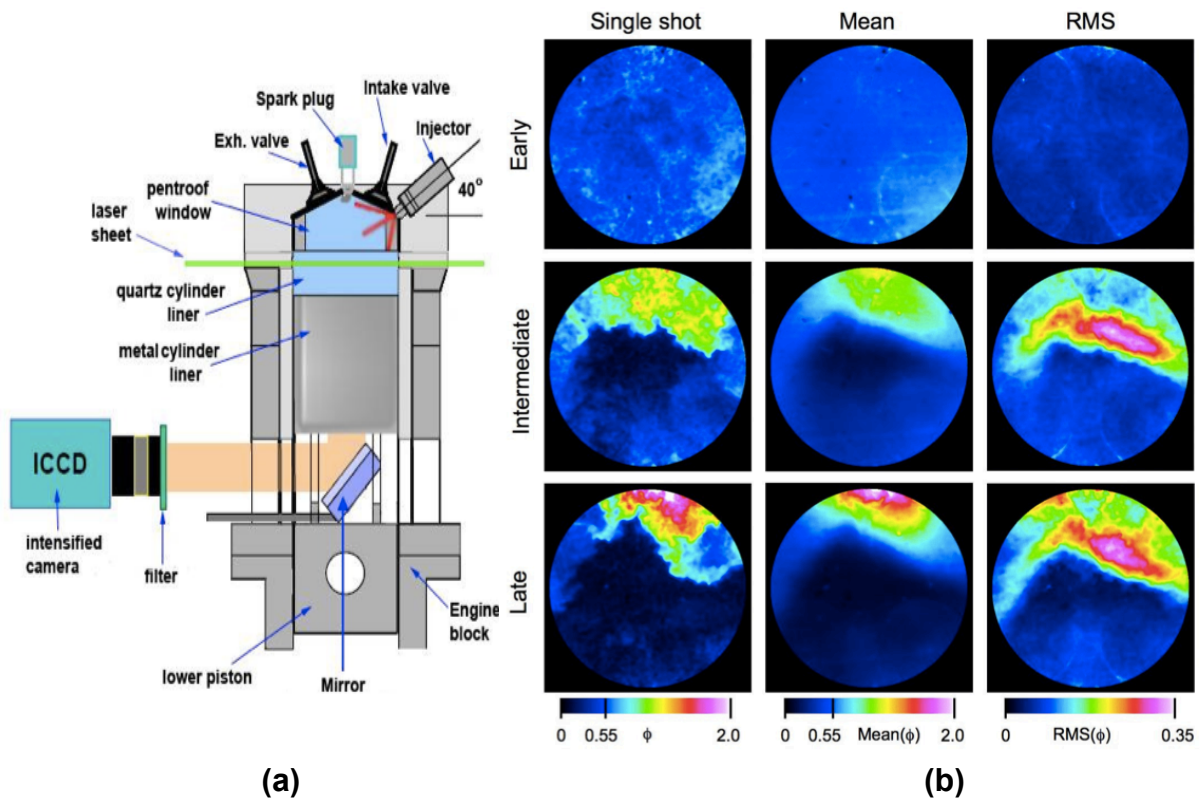


Figure 5.1 PLIF measurement (a) Experimental Set-up, (b) Local fuel concentration measurement at different injection timing. [54]

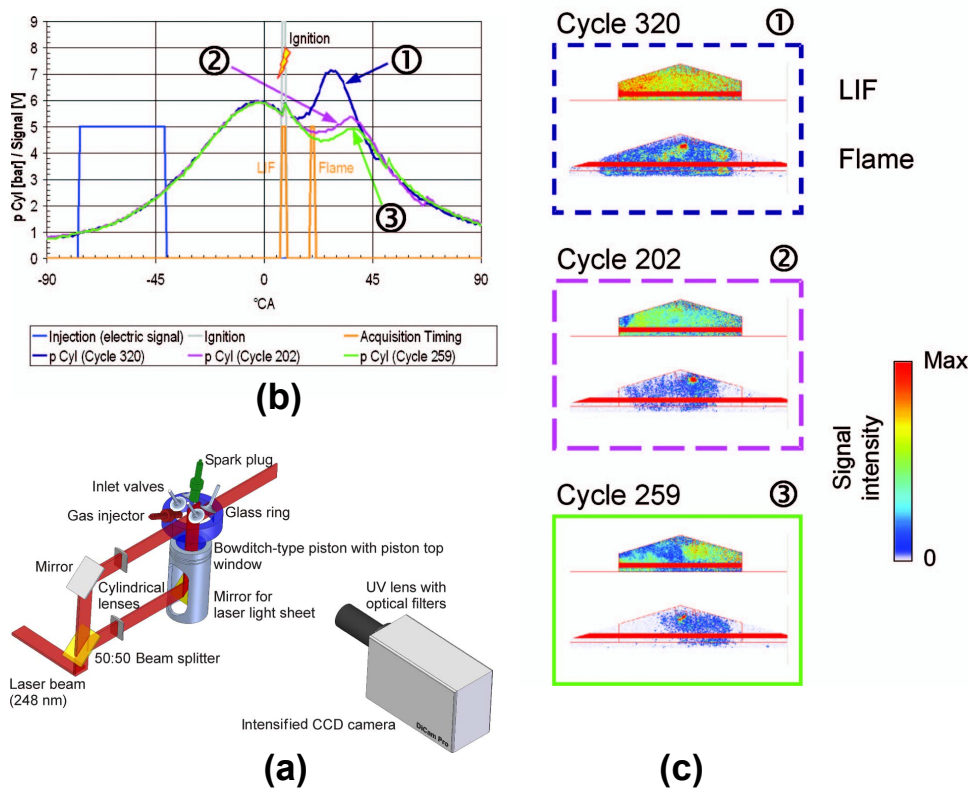


Figure 5.2 TLIF Measurement (a) Experimental set-up (b) In-cylinder pressure histories (c) LIF and Flame intensity. [55]

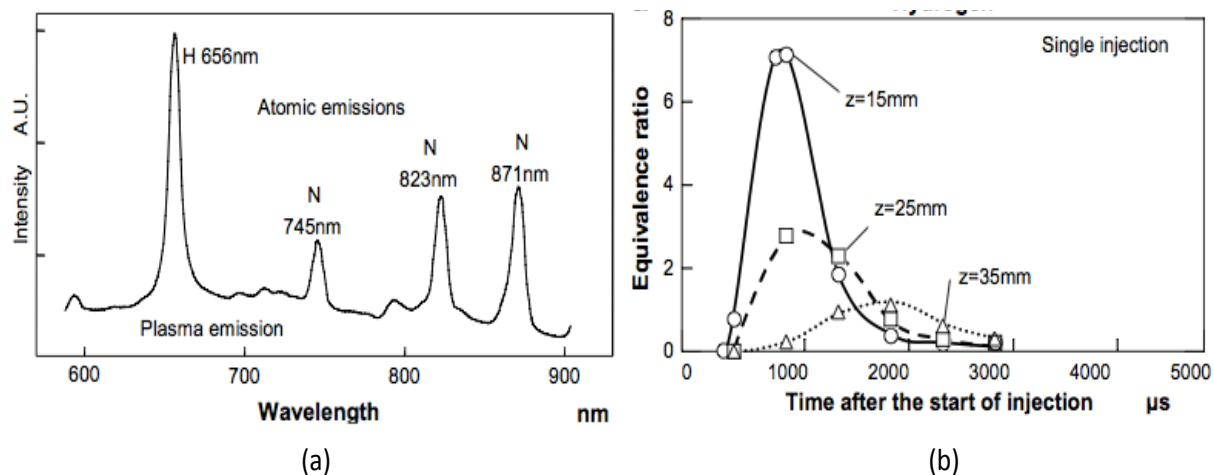


Figure 5.3 Hydrogen concentration measurement in a constant vessel using LIBS. [58]

hydroxyl (OH, 306 nm wavelength) emission intensities from the spark that initiates combustion. They determined the cycle-resolved local fuel–air ratio in the spark gap, controlled the large-scale stratification, and evaluated the utility of SIBS as an engine diagnostic tool.

5.2 Background spark ignition physics

Since the development of the very first combustion engines, engineers have been concerned with ignition of the combustible mixture in the cylinder. In order to ignite a mixture of fuel and air, its thermal energy must be increased locally to overcome the activation energy of the starting reactions. Various concepts have been developed. In today's internal combustion engines, merely two of them are used: spark ignition (SI) and compression ignition (CI).

5.2.1 Phases of a spark discharge

In order to achieve an electrical discharge in the gap of a spark plug, it is necessary to apply a sufficiently high voltage. Considering typical ignition systems, it takes upto several hundred microseconds to raise the voltage to the necessary level. This level is heavily influenced by electrode shape, gap size, gas composition and pressure, as well as the presence of ionizing radiation. The latter is needed to provide primary electrons needed to start the ionization

process in the gap. However, the rate of creation ($\approx 10 \text{ cm}^{-3} \text{ s}^{-1}$) and lifetime (10ns) of such free electrons is insufficient to initiate an avalanche directly. Instead, these electrons get attached to electro negative species, such as O_2 . Since there is also a reverse process (electron detachment), an equilibrium will form in the gas, constantly providing and consuming free electrons, thus increasing the average density of electrons available in the gas considerably. From this reservoir, electrons are accelerated towards the anode. More pairs of electrons and excited ions are formed by collisions of the fast electrons with other particles in the gas. These secondary electrons are then accelerated themselves and create more electron-ion pairs further ahead. However, since this avalanche is directed towards the anode, it will extinguish as soon as the latter is reached. Therefore, other, non-local processes are needed to get things started: After the collision, the ions are left behind in an excited state. During de-excitation, UV radiation ($\lambda < 200 \text{ nm}$) is emitted, which eventually ionizes atoms closer to the cathode, providing a means for the process to start again. This way, the origin of the avalanches can move closer to the cathode. The process is illustrated schematically in Fig. 5.4.

The electrical discharge produced across the electrodes of a spark plug is composed of four distinct phases: pre-breakdown, breakdown, arc discharge, and glow discharge [68][69]. Each phase of the spark discharge involves a different physical process; therefore each phase has a different effect on electrode erosion[68] [69]. This section will discuss each phase of the electrical spark discharge and how each mechanism contributes to electrode wear.

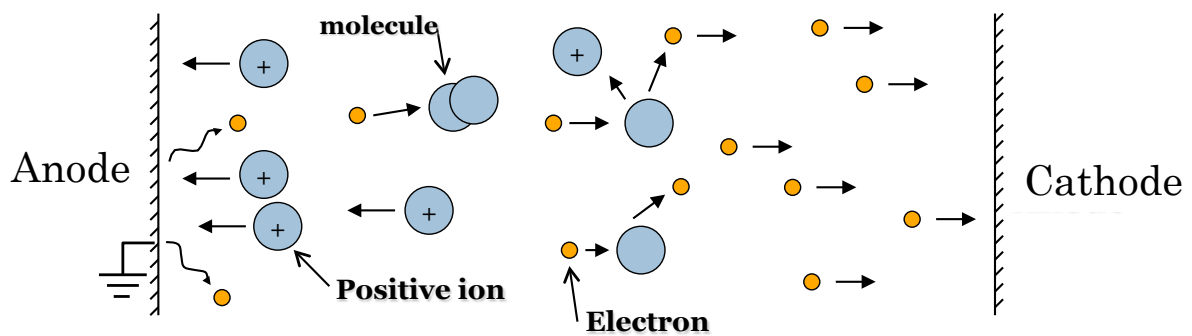


Figure 5.4 Development of an electron available in the direction of the anode. UV radiation emitted by highly excited ions is responsible for the progress of the avalanche origin towards the cathode. Once positive ions are formed close to the cathode, they are accelerated towards it and may liberate electrons from its surface.

Initially, the gas between the two electrodes plays the role of an insulator. As the voltage is applied to the anode, the electric fields in its vicinity attract drifting electrons, which are accelerated by the field. It is assumed that there are always a few electrons around the gap provided by the action of cosmic rays or other sources[70]. As the electrons are accelerated by the electric field, they may reach high enough kinetic energy that once they collide with an atom, the atom becomes ionized and loses an electron. The distance between collisions is on the order of the mean free path. On average, the atom-electron collision will produce one ion and one electron. The region of ionized gas and electrons is called a streamer. Based on Kulikovsky's [71] simulation of pre-breakdown for a 1-centimetre (cm) gap at atmospheric pressure, the mechanism of streamer propagation was defined by the ionization growth in a thin region ahead of the streamer tip. As the streamer progresses to the cathode with help from the electromagnetic field, the number of electrons and ions grows exponentially.

In Figure 5.5 schematic diagram of the voltage and current of ignition sparks as function of time is presented [77]. The actual values depend on the electrical components of the discharge circuits as indicated. The breakdown phase is characterized by very high peak values of voltage (~ 10 kV) and current (≈ 200 A), an extremely short duration (1-10ns) and a cold cathode. The breakdown phase starts from the moment the gap is bridged up to the moment where thermal equilibrium between the electron temperature and the gas temperature can be assumed in the plasma channel. Naidis [72] explained that once the streamer has closed the gap, there are two mechanisms that have been proposed. The first one is thermal, which is responsible for lowering the gas number density because of the spark channel expansion due to heating. The other mechanism, which is chemical, involves the accumulation of radicals and excited molecules, which change the balance between the rates of generation and loss of electrons. He mentioned that for streamer-to-spark transition the chemical mechanism is dominant. On the other hand, Maly [69] reported that the electron and gas temperatures could reach 60000 K during the breakdown phase and that the gas is highly ionized. The gas molecules inside the channel are fully dissociated and ionized. The energy supplied is transferred almost without loss to the plasma, where it is stored by dissociation and ionization.

Uhm [73] developed an analytical expression for the ionization rate and compared it to the air ionization rate measured experimentally with an applied electric field, E/p , where E is the electric field and p is the ambient pressure before the beginning of the discharge. He showed

that both methods lead to an identical profile of gas ionization. By using the ionization rate and assuming a Maxwellian energy distribution of electrons, he found a good agreement between the experiment and the analytical solution. From the analytical solution he derived the maximum temperature of the electrons during the breakdown and found it to be equal to:

$$T_e = 9.14 \times 10^{-5} \frac{E}{p} \quad (5.1)$$

Where E is the electric field, i.e. breakdown voltage divided by the spark gap, in V.cm^{-1} , p is the pressure in atmospheres, and the temperature of the electrons, T_e , is in electron Volts (eV, 1 eV is equivalent to 11600 K). The breakdown voltage, in kV, for air can be approximated from Paschen's law as a function of temperature and pressure via Equations (5.2) and (5.3),

$$V_b = 24.22 \times x + 6.08 \sqrt{x} \quad (5.2)$$

$$x = \left(\frac{293}{T}\right) \left(\frac{P_p}{1}\right) \left(\frac{d}{10}\right) \quad (5.3)$$

For Paschen's law, the pressure, P_p , is in atmosphere, d is the spark gap, in millimetre, and T is the temperature of the gas, in Kelvin. The use of overvoltage as employed by Aldén, to deposit the energy in a short amount of time, does not contribute to an increase of the gas or electron temperature, but rather increases the spark channel radius by increasing the spark current. This observation is illustrated when the plasma radius, r_o , in millimeter, is estimated by the time dependent equation [74][75],

$$r_o = 0.93 \rho_r^{-1/6} I^{1/3} t^{2/3} \quad (5.4)$$

Where ρ_r is the gas density before the discharge, in g.cm^{-3} , the spark current, I , is in kA, and t , the time, is in microseconds. The gas pressure in which a spark is produced in can have a significant affect on the discharge production and development as well as the electrode erosion progression. Studies have shown that spark production at or near atmospheric pressure (1 bar) only involves the breakdown and glow discharge phases [68]. This regime produces a low current density while still delivering substantial energy to the gas thereby limiting and in some cases eliminating cathode erosion[68]. However in an engine the gas pressure is substantially higher and research has shown a distinct difference in the spark

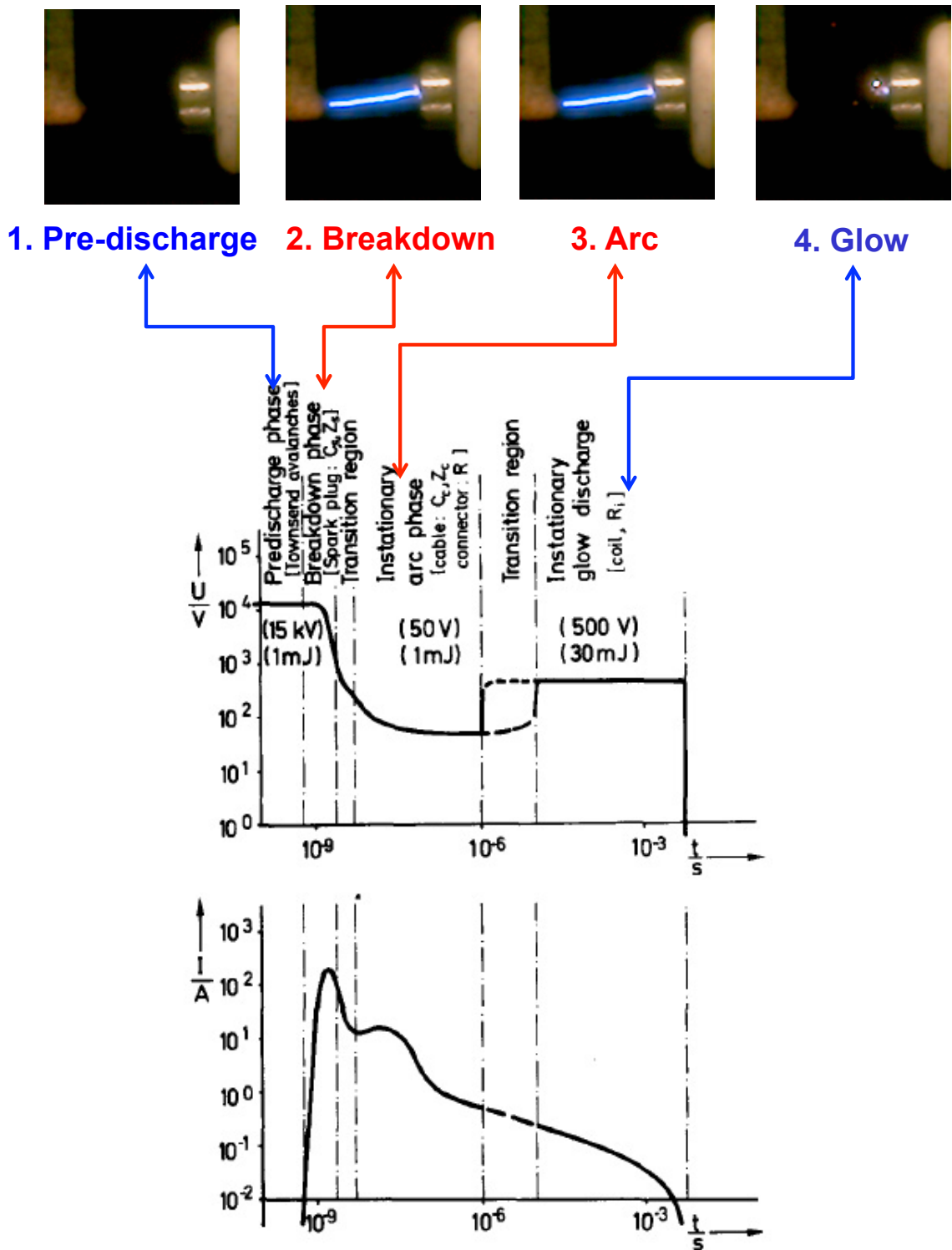


Figure 5.5 Schematic diagrams of voltage and current of technical ignition systems as functions of discharge time. Typical values are given in parentheses, circuit parameters responsible for discharge modes are indicate in brackets. [77]

formation and development at in-cylinder pressures. At higher pressures all three phases of the spark breakdown process occur. For electrical arcs produced in a gas, Paschen's Law states that the threshold breakdown voltage for a given spark gap is proportional to the gas pressure within the spark gap. Figure 5.6 shows breakdown voltage as a function of pressure according to Paschen's Law for a 1 mm electrode gap.

The arc and the glow discharge must always be preceded by a breakdown phase, which provides the conductive path between the electrodes necessary to start these discharges. The arc voltage is very low (<100 V), although the current may be as high as the impedances of the external circuit permit (500mA to several kA). Only 1% of the particles are ionized, but the degree of dissociation may be quite high in the central region of the discharge.

The final phase of the electrical breakdown process is the glow discharge. This phase begins as the available current from the ignition system begins to drop (below ~ 100mA) and the hot spot can no longer be sustained [68]. The electrons are then supplied by a much more inefficient process, ion impact emission that induces a large voltage drop and spreads the discharge across the entire electrode face significantly lowering the current density.

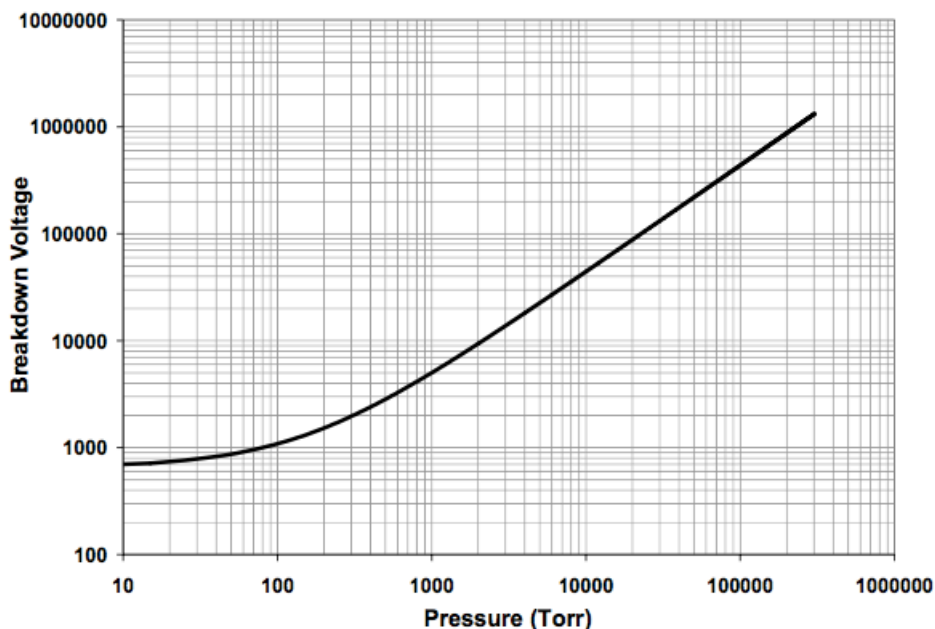


Figure 5.6 Minimum breakdown voltage for 1 mm electrode gap according to Paschen's law.

5.3 Spark-induced Breakdown Spectroscopy (SIBS)

Spark Emission Spectroscopy- One possibility to measure the equivalence ratio at the spark gap is the spectral analysis of the spark emission directly after the spark breakdown. Merer and Wallace [65] described the temporal evolution of the light-emitting processes in the spark (Figure 5.7). Within the first 10 ns of the spark the radiation is emitted from excited fuel and air molecules. After this phase emissions from atoms can be detected, which emit light by relaxing from multiply ionized atomic states. This period is followed by the formation of excited diatomic molecules from the recombination of atoms [66]. In this phase molecules with nitrogen, e.g. NO, NH and CN are spectrally dominant. In the next step chemical reactions take place and the flame kernel is formed. This can be observed in the colder fringes at the plasma. According to Fansler et al. [67], the CN emission signal intensity at 388 nm during the recombination phase can be correlated with the local carbon number density n_c . Therefore, it can be assumed that the CN molecules result from the ionization and recombination in the breakdown and arc phase of the spark. For a given spark gap geometry the gas density is the determining factor for the required breakdown voltage and thereby for the energy in the spark. Therefore, the CN emission intensity must be normalized to the amount of electrical energy dissipated in the spark during the measurement interval. The signal intensities from the spark emission depend on the experimental setup and quantitative measurements require calibration. For calibration, the engine is operated with homogenous charge and known amounts of air and fuel. For each condition the carbon number density, n_c is calculated using measured pressures and calculated temperatures. Fansler et al. investigated equivalence ratios ϕ in the range $\Phi = 0 - 3$ while running the engine skip-fired; where one fired cycle was followed by eleven non-fired cycles. For the experiments presented here the engine was continuously fired, with a nearly constant residual gas fraction of 10% over the whole range of operating points. Without skip firing we must ensure reproducible composition of the residual gases and thus prevent misfire. The calibration measurements are therefore limited to the $0.7 < \Phi < 1.6$ ranges.

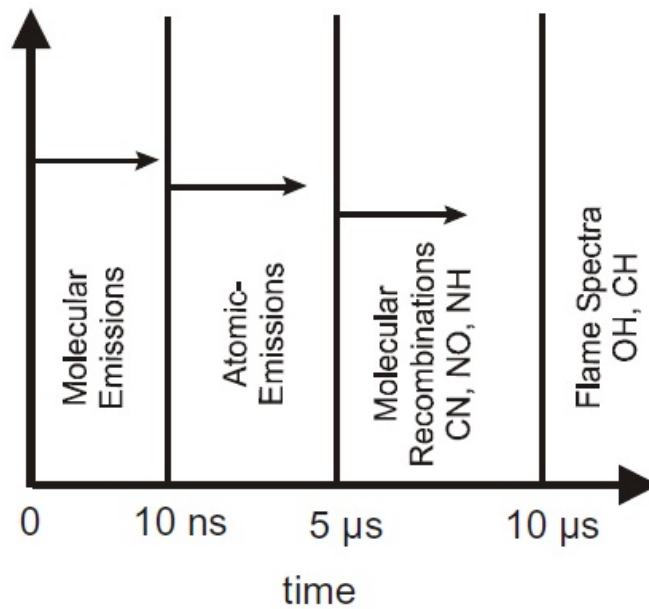
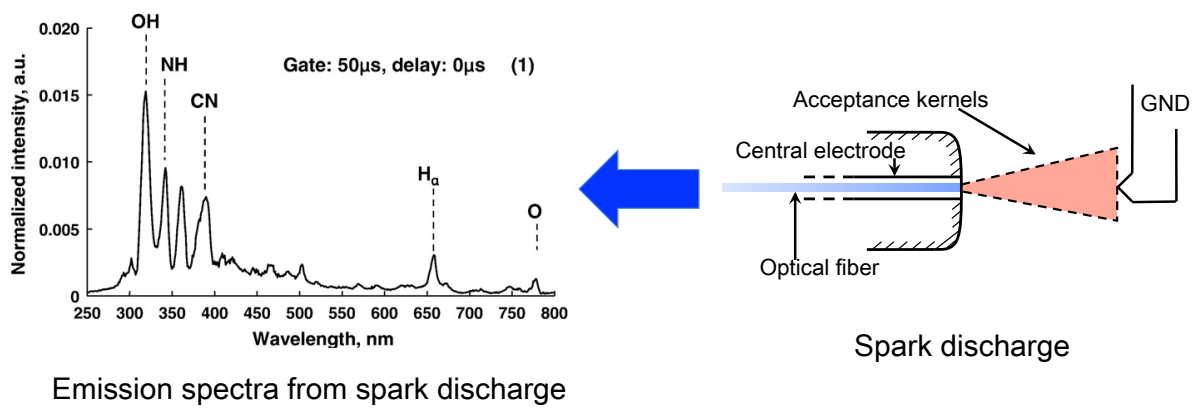


Figure 5.7 Temporal evolution of spark emission.[65]

5.4 SIBS experimental set-up

SIBS is a measurement technique in which spectrally resolved emissions of plasma generated by the spark plug. In theory, the air–fuel ratio in the spark gap can be determined through analysis of the light emission from the spark, which initiates combustion. Figure 5.8 shows the measurement system used with our fiber optic spark-plug sensor in the same optical SI engine. A specially designed single-cylinder compression-expansion engine that could only be fired once was used for the experiments. This engine can observe only single cycle combustion phenomena in one experimental run. A summary of engine specifications is provided in Table 3. Emission spectra from the spark discharge between the ground and center electrodes were obtained with the optical fiber coupled to a spectrometer.

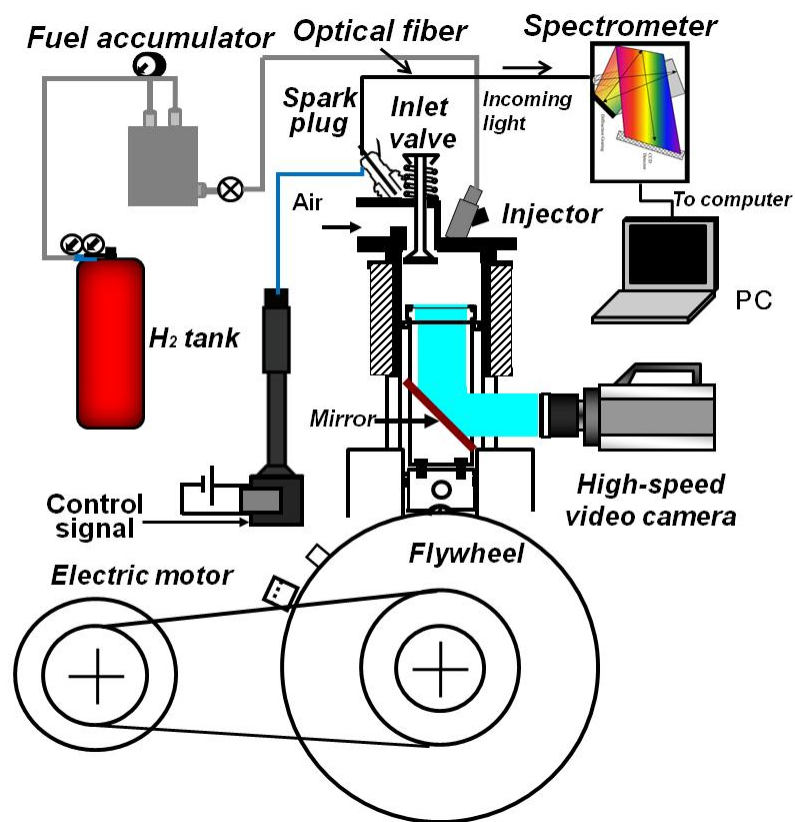


Figure 5.8 Schematic view of the optical engine experimental setup with SIBS sensor.

5.4.1 Spark plug

A commercial spark plug (see Figure 5.9) with an electrode spacing of 2 mm was used as the SIBS sensor in a practical SI engine. The fiberoptic spark plug is shown in Figure 5.9. The discharge voltage and current were supplied from a direct-current power source with an input voltage of 12 V and input current of 20 A. A spark-charging duration of 10 ms was used. Coil ignition systems normally have three phases: breakdown, arc, and glow discharge. Dissociation and ionization occur during the breakdown phase, during which an ionizing streamer propagates from the ground electrode to the center electrode. After breakdown, the arc phase occurs, and atomic recombination leads to molecule formation. The breakdown and arc phases appear together as a spike in the discharge voltage and current. An optical UV-grade quartz fiber with a core diameter of 600 μm was housed in the center electrode of the spark plug. The optical fiber had a numerical aperture (NA) of 0.20, which covered the area around the ground electrode. Figure 5.10 show that the ground electrode had a small projection toward the center electrode to allow stable initiation of the spark discharge. This small projection was the starting point of the ionic streamer during the breakdown and arc phases.

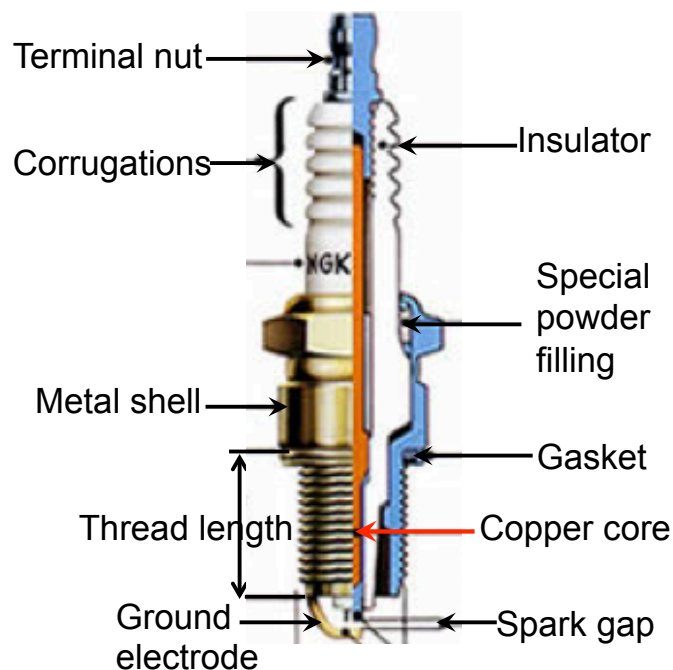


Figure 5.9 Construction of a spark plug.

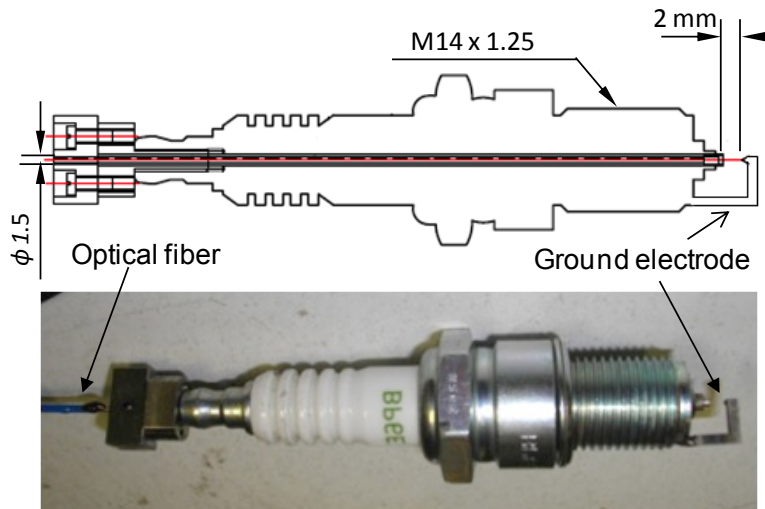


Figure 5.10 Developed fiberoptic spark plug sensor.

5.4.2 Spectrometer

In this experiment Ocean Optics USB2000+ spectrometer was used to measure the SIBS spectra. The spectrometer measured the optical emission spectrum over a range from 250 and 800 nm with a resolution of 0.3 nm and a minimum integration time of 1 ms. The spectrometer converted incoming light into voltage across a charge-coupled device (CCD), wherein each pixel of the CCD represented a pre-calibrated wavelength. Data analysis was performed using the Ocean Optics SpectraSuite software package.

A spectrometer is a device that measures light intensity as a function of wavelength. It does this by diffracting the light beam into a spectrum of wavelengths, detecting the intensities with a charge-coupled device, and displaying the results as a graph. The output of a spectrophotometer is usually a graph of light intensity versus wavelength. The data collected to generate this graph can typically be saved as a table of wavelengths and intensities. There are four main parts of a spectrometer: the light source, subject, detector, and interpreter. Some examples of light sources are visible, infrared, and ultraviolet light. The light created by the light source passes through the subject where some light is usually absorbed, is received by the sensor, and is interpreted into an output such as a graph.

In the Ocean Optics USB2000+ spectrometer as shown in Fig. 5.11, the light source passes through the sample and enters the spectrometer through a slit. The narrow slit disperses the light, spreading it out. The light reflects off of a concave collimating mirror and is reflected to a dispersion grating. The dispersion grating reflects the light and also disperses it towards a second concave mirror. This focusing mirror focuses the light onto a detector. At the end of the light path is the detector. In most spectrometers, it is a linear charge-coupled device (CCD). A CCD is a type of image sensor that detects light. It is an integrated circuit made up of an array (or in this case, a linear arrangement) of linked/coupled light-sensitive capacitors. The light-sensitive capacitors detect the intensity of light received and convert it into an electrical signal.

The linear CCD detector corresponds to the range of wavelengths on a hand held spectrophotometer. Each pixel on the CCD represents a specific wavelength of light, and the more photons absorbed, the more electrical signal generated. Therefore, the electrical signal output by the CCD at each pixel is proportional to the light intensity at each corresponding wavelength.

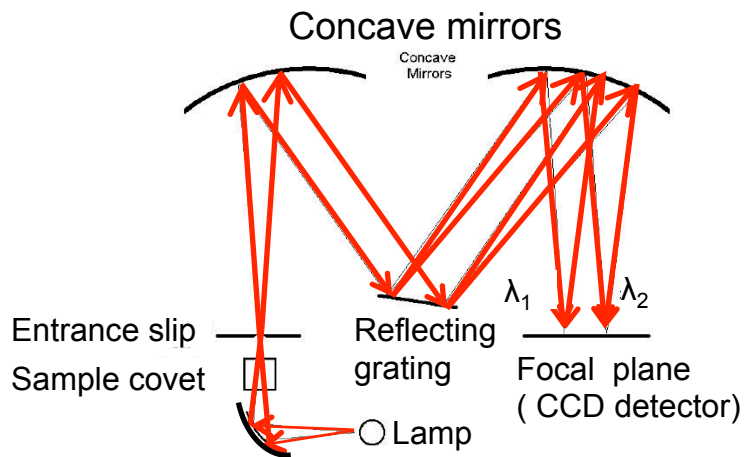
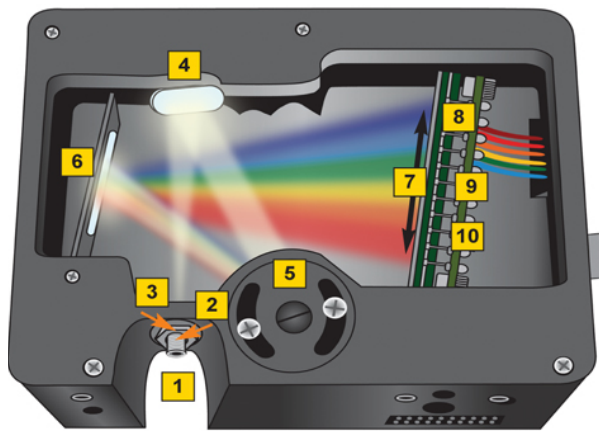


Figure 5.11 Schematic optical path of the ocean optics USB2000+ spectrometer.

5.4.3 Optical fiber

In this experiment ST600F-FV type optical cable was used to collect SIBS spectra. The cable used here is known as a step index (SI) and refers to the fact that the refractive index of the fiber core (n_{core}) is a constant and it is the step change in the refractive index between the core and cladding materials that leads to rays being guided down the optical fiber due to the total internal reflection of rays above the critical angle as shown in Fig.5.12. On the vinyl-coated optical fiber, it has a structure that accompanied the transition longitudinal reinforcement for protection from external forces such as tension and compression forces, thereon.

The Numerical Aperture (NA) is a measure of how much light can be collected by an optical system such as an optical fibre or a microscope lens. The NA is related to the acceptance angle θ_a , which indicates the size of a cone of light that can be accepted by the fibre.

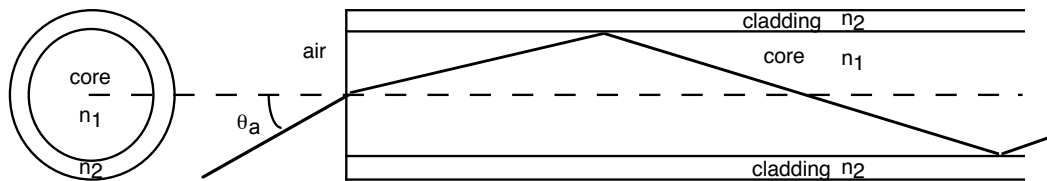


Figure 5.12 Guided rays of a step index (SI) optical fiber

Both numerical aperture and acceptance angle are linked to the refractive index via:

$$NA = n_a \sin \theta_a = (n_1^2 - n_2^2)^{1/2} \quad (5.5)$$

Where n_1 = refractive index of core; n_2 = refractive index of cladding; n_a = refractive index of air (1.00). Table 4 show the optical fiber specifications.

Table 4 Optical fiber specifications

Type	Size	NA	Core diameter μm	Fiber diameter μm	Optical transmission loss
SI	ST600F-FV	0.2	600	750	$\leq 5 \text{ dB/km}$

5.5 SIBS calibration

5.5.1 Background estimation and subtraction

The background at any point, due to inelastically scattered, is assumed to arise solely from the scattering of electrons of higher kinetic energy and is thus proportional to the integrated photoelectron intensity to higher kinetic energy. The background estimation is made under the steps,

1. Calculating the smoothing curve of the spectrum
2. Regard the smoothing curve as the background curve within the region without peak.
3. Let q_1 and q_2 be the start and end points of the background on the energy axis for a peak.
4. Connect the end points (q_1, B_1) and (q_2, B_2) on the spectrum with a straight line or Shirley method.

The background curve based on the Shirley method is calculated by the following way: For the calculation of the background curve shown in Fig. 5.13, we assume that there are n points between the end points of (q_1, B_1) and (q_2, B_2) , and let the background and net peak at the i -th point in the j -th approximation be $BG_j(i)$ and $N_j(i)$, respectively. Then

$N_j(i) = y_i - BG_j(i)$. By using the Shirley's formula,

$$BG_i(i) = \frac{(B_1 - B_2)Q_j(i)}{P_j(i) + Q_j(i)} + B_1 \quad (5.6)$$

where $P_j(i)$ and $Q_j(i)$ are the left and right side of the net peak areas at i -th point in the j -th approximation, and they are expected as follows (assuming the step width being 1):

$$P_j(i) = \sum_{l=1}^i N_j(l) - 0.5(N_j(1) + N_j(i)) \quad (5.7)$$

and,

$$Q_j(i) = \sum_{l=i}^n N_j(l) - 0.5(N_j(i) + N_j(n)) \quad (5.8)$$

For the 0-th approximation, the initial background curve $BG_0(i)$ is taken as the straight line connecting the 2 points (q_1, B_1) and (q_2, B_2) . This iterative calculation continues until the following convergence condition is satisfied:

$$|S_j - S_{j-1}|/S_j < 0.001 \quad \text{where, } S_j = P_j(i) + Q_j(i) \quad (5.9)$$

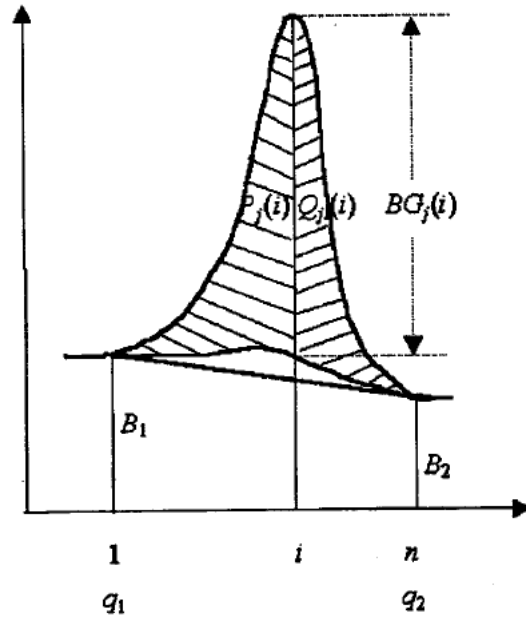


Figure 5.13 Schematic diagram of the background subtraction by the Shirley method.

5.5.2 Intensity ratio with overall equivalence ratio

The calibration measurements presented in this experiment were conducted in the same optical DISI engine for near-homogeneous hydrogen-air mixture combustion at various known equivalence ratios. The overall equivalence ratio for near-homogeneous combustion (initial pressure= 0.1 MPa; initial temperature = 300 K) was changed from 0.31 to 1.4. The SOI was coincident with BDC and spark timing was TDC. In this research, spectra were recorded in a wavelength range from 250 nm to 800 nm. Five strong atomic emission peaks are observed in this wavelength range which are shown in Figure 5.14. The peak at 656 nm is from hydrogen ($H\alpha$), two peaks at 501 nm and 745 nm are from nitrogen, 589 nm is from Sodium (Na), 767 nm is from Potassium and 777 nm is from oxygen. Figure 5.15 illustrates the intensity ratios of $H\alpha/O$, compared with the global equivalence ratio measured during near-homogeneous combustion. The Shirley background correction method [97] was used to subtract the elastic scattering. The $H\alpha$ and the $O(I)$ peak was integrated over a certain wavelength range. The data of $H\alpha/O(I)$ intensity ratio showed a clear increasing trend with increasing overall equivalence ratio, possibly rolling off slightly at higher equivalence ratios. It is possible to generate a calibration curve from the global equivalence ratio and the $H\alpha/O(I)$ ratio. In the present work, the $H\alpha/O(I)$ intensity ratio and the overall equivalence ratio data exhibited a linear fit, determined by least squares to be,

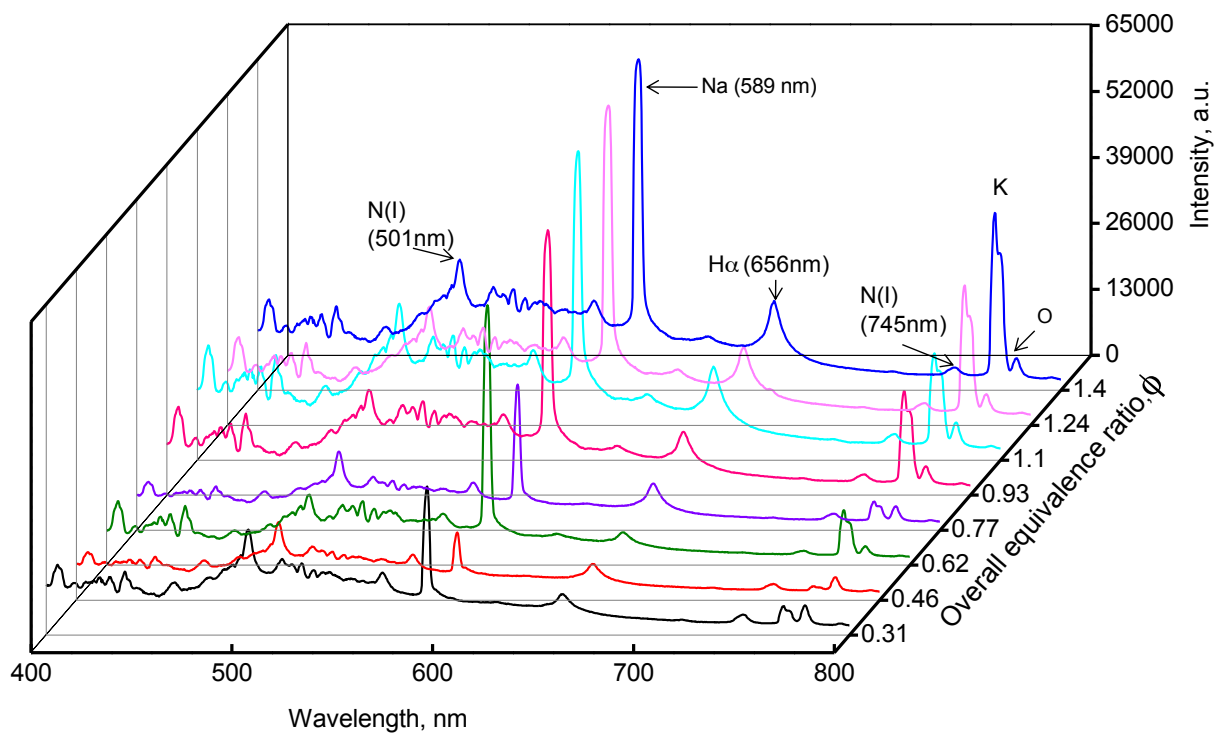


Figure 5.14 Plasma emitted spectra during near-homogeneous combustion at different equivalence ratios.

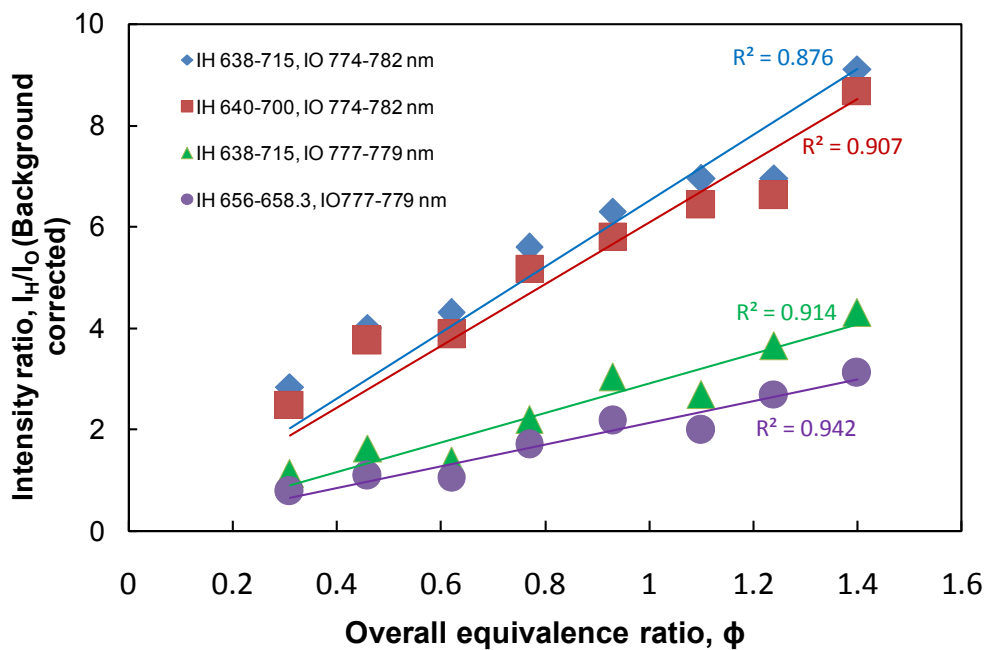


Figure 5.15 Correlation of the atomic line intensity ratio, $H\alpha/O$ with the overall equivalence ratio.

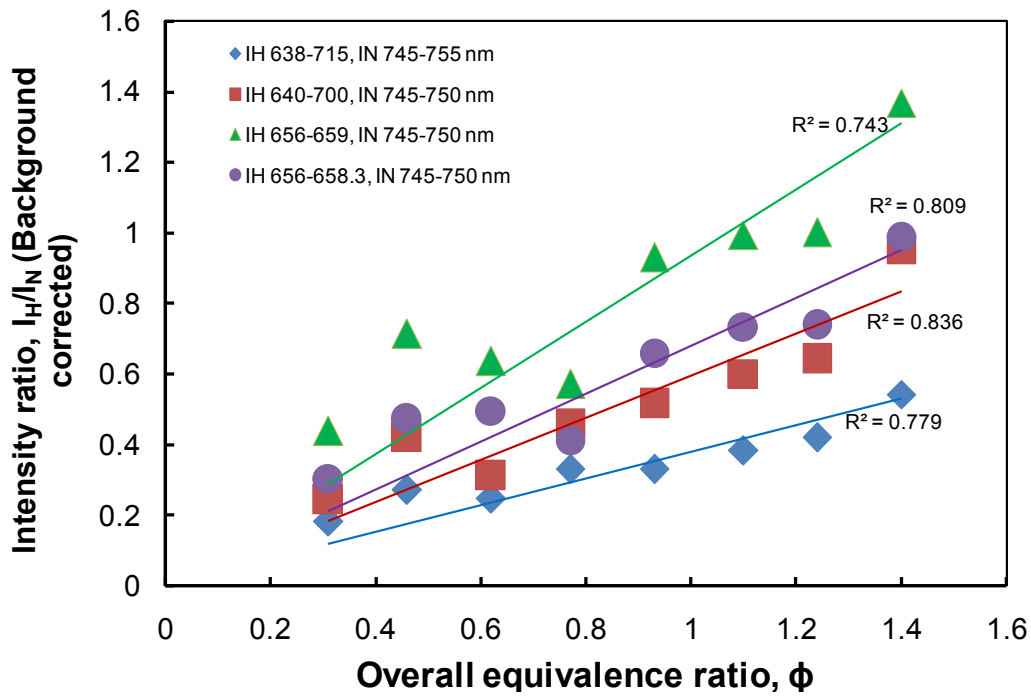


Figure 5.16 Correlation of the atomic line intensity ratio, $H\alpha/N$ with the overall equivalence ratio.

$$\phi = [(H\alpha/O) \times 0.338] \quad (5.10)$$

with regression coefficients $R^2 = 0.942$. For the nitrogen atomic emission, the peak at 745 nm is chosen for this research to compare with that of hydrogen for acquiring nitrogen/hydrogen fraction with high S/N ratios. Figure 5.16 illustrates the intensity ratios of $H\alpha/N$, compared with the global equivalence ratio measured during near-homogeneous combustion. However, further analysis of the intensity ratios, $H\alpha/N(I)$, is required to generate a calibration curve that they must respond linearly with the overall equivalence ratio.

5.6 Local equivalence ratio at different ignition timing

Spectrally resolved atomic emissions of plasma generated by the spark plug were investigated to determine the local equivalence ratio. Equivalence ratio, ϕ is defined as the ratio of the actual fuel-to-oxidizer mass, $m_{\text{fuel}}/m_{\text{air}}$, over the ratio of the fuel-to-oxidizer mass at stoichiometric condition, $(m_{\text{fuel}}/m_{\text{air}})_{\text{stoich}}$. The determination of the local equivalence ratio is important in combustion processes, since this ratio strongly affects the combustion

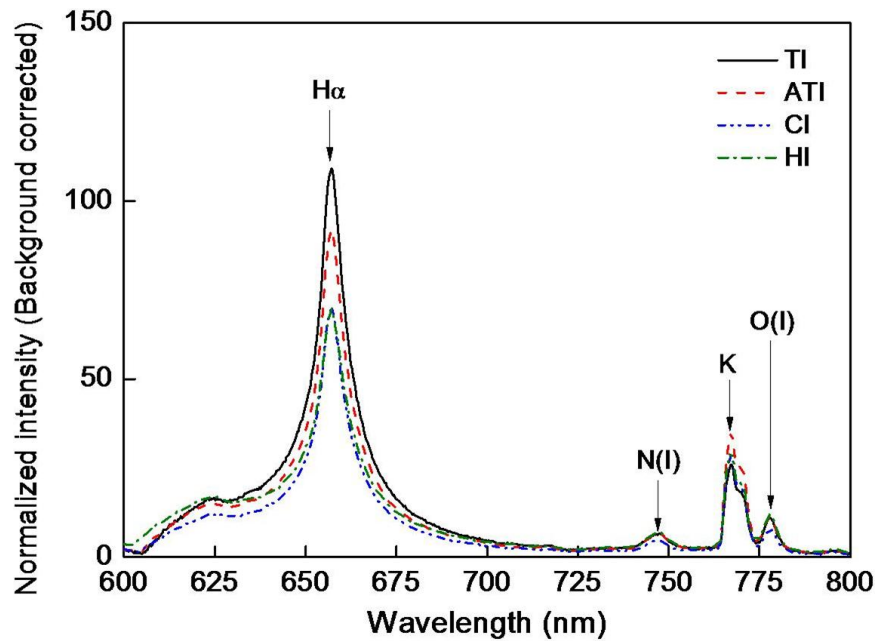


Figure 5.17 SIBS spectra for different ignition mode combustion

characteristics. Figure 5.17 shows the average emission spectra with a corrected background obtained from SIBS sensor for the 600–800 nm regions, corresponding to engine combustion at different ignition modes. The spectrometer integration time was used of 1ms. The spectrometer was gated shortly after spark breakdown. Each spectrum corresponds to the average of 10 cycles of data. A 600 lines/ mm grating was used to record the spectra in the 250-800 nm spectral regions. The atomic emission spectra from the hydrogen $H\alpha$ line at 656 nm, nitrogen N (I) line at 740–750 nm, potassium (K) line at 767 nm, and oxygen O (I) triplet line at 777 nm were obtained using the developed fiber-optic sensor. The emission at 767 nm due to potassium (K) is routinely found in current research and may have been due to combustion of the lubricating oil [84].

Figure 5.18 shows the measurements of the mean local equivalence ratio and the initial combustion duration for the four ignition modes at global equivalence ratio, $\phi = 0.22$. The estimated local equivalence ratio for different ignition modes was obtained using the linear fit (as shown in Eq. 5.10). In this paper, the initial combustion duration is defined as the interval of the crank angle from the ignition start to 5% mass fraction burned. The error bars showed the standard deviation both for the mean local equivalence ratio and the initial combustion

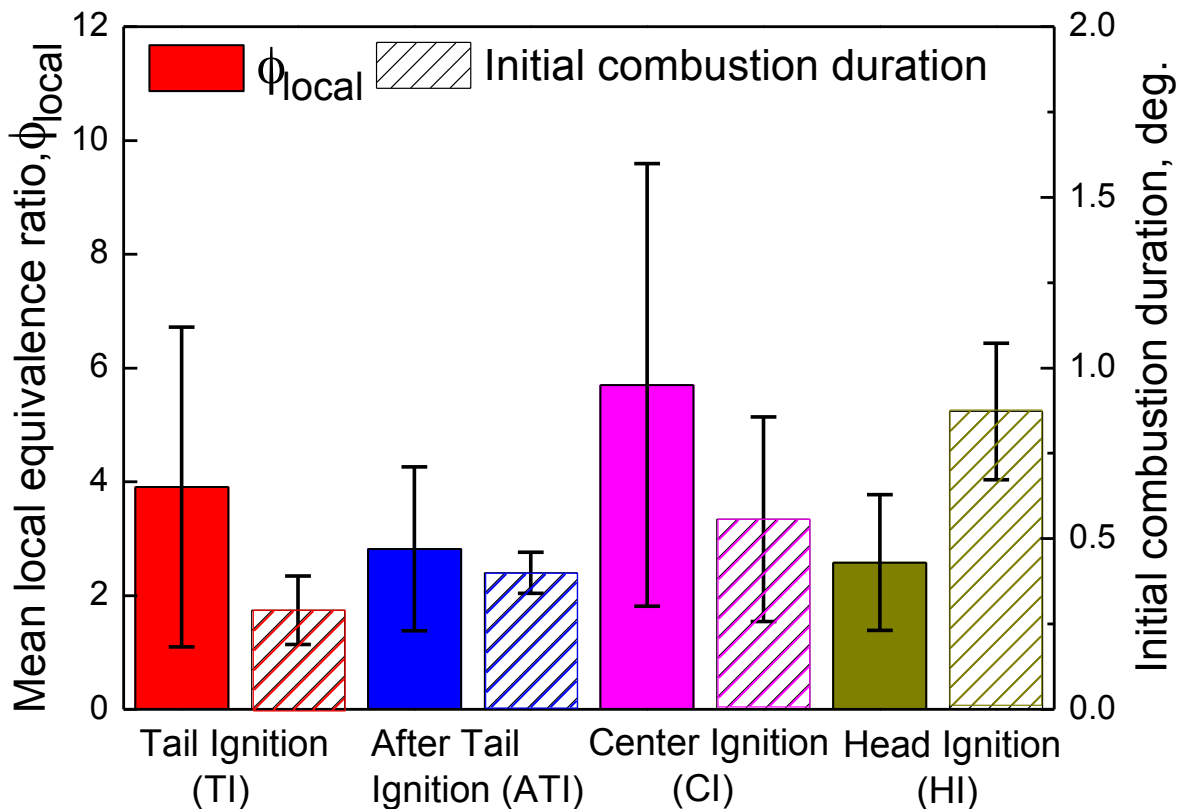


Figure 5.18 Local equivalence ratio measured with SIBS and initial combustion duration.

duration measurements. The estimated local equivalence ratio at the spark gap just after spark breakdown showed very rich. The standard deviation of the local equivalence ratio measurement shows the bulk of the variation at each ignition condition. It has been known that the flammability range for hydrogen is 4–75%, ($\phi=0.1$ to 7.1) by volume in air at 298 K and 1 atm [98]. But for typical engine operation at high pressure and temperature, the minimum ignition energies of hydrogen–air mixtures is much lower than for other fuel. For HI, the estimated local equivalence ratio was relatively lower than those in other ignition modes. The COV of local equivalence ratio for HI was about 40%. The initial combustion duration for HI takes a large crank angle compared to other ignition modes. Fajardo et al. [99] concluded that the increase in shear strain in the spark plug surrounding, combined with fuel stratification and extension of plasma channel, could prevent flame kernel development in a DISI engine. The estimated local equivalence ratio for CI mode combustion showed very rich compared to other ignition mode. The COV of local equivalence ratio for CI was about 46%. CI mode combustion had heterogeneous conditions, in which the ignition occurred while the fuel was in the process of being injected. The estimated local equivalence ratio for TI showed

rich in the spark gap. Hence, parts of the hydrogen jets may still be quite rich in fuel close to the spark plug. The COV of local equivalence ratio for TI was about 28%. The initial combustion duration for TI exhibits short duration compared to the other ignition modes. The estimated local equivalence ratio for ATI was lower than that for TI and CI but higher than HI timing. The COV of local equivalence ratio for ATI was about 33%. Kaiser et al. [57] concluded that late injection yielded bimodal distributions of the fuel mass across equivalence-ratio space, with a rich region near the injector and lean mixtures throughout the rest of the field of view. As described above, the initial combustion is affected by local equivalence ratio and jet flows.

5.7 Summary

Chapter 5 measured the local equivalence ratio at stratified charge combustion condition using spark-induced breakdown spectroscopy (SIBS) with a fiber-coupled CCD spectrometer. A fiber-optic spark plug sensor was developed for application to practical DISI engine. The atomic emission intensities $H\alpha$, and O (I) produced during spark discharge were correlated to the global equivalence ratio. For stratified charge operation of the jet injection relative to ignition timing, the estimated local equivalence ratio at the spark gap just after spark breakdown was very rich and varies widely from cycle-to-cycle. The results presented here confirm the usefulness of spark-induced breakdown spectroscopy as a diagnostic tool for spark-ignition engine. Optimization of the UV-grade optical fiber and the optical gate period in CCD camera should be carried for further measurement.

6 CFD analysis on mixture formation

6.1 Introduction

The abbreviation CFD stands for computational fluid dynamics. It represents a vast area of numerical analysis in the field of fluid's flow phenomena. Headway in the field of CFD simulations is strongly dependent on the development of computer- related technologies and on the advancement of our understanding and solving ordinary and partial differential equations (ODE and PDE). For numerically simulating gas flows, fuel sprays and combustion in fuel injection engine, an original computer code GTT (Generalized Tank and Tube) with high-order numerical schemes has been developed by research group of Kyoto University.

6.2 Literature reviews

In the last two decades, great progress has been made on CFD tools for both Diesel and spark plug internal combustion engines with the development of numerical models for various phenomena occurring inside the cylinder. However, only few works has been made on gas injection and the connected physical processes.

Johnson et al. [104] simulated transient injection of hydrogen and its combustion on a coarse mesh by removing the details of the jet dynamics at the exit of the orifice, and compared model predictions with experimental penetration results in a constant volume chamber at engine operating conditions. They showed that the jet tip penetration with combustion is comparable to the penetration without combustion and the penetration history was highly sensitive to the mesh refinement and the treatment of turbulence. Mather and Reitz [106] modelled the injection of auxiliary gas in engines using a single grid cell to represent the nozzle opening. They demonstrated that the penetration rate of the gas jet could be adequately resolved by applying a model of the near-nozzle shock structure in the turbulent underexpanded jet, and by limiting the turbulence length scale in the computational cells near the nozzle exit. However, they needed to alter the inflow area to match the Mach disk area, as the cylinder pressure changed during the combustion process.

Ouellette [107] simulated underexpanded gas jets and noted the limitations of fine grid size that was needed adjacent to the nozzle. Abraham [108][109] investigated the effect of grid resolution and ambient turbulence parameters on the computed structure of transient gas jets. He showed that a grid size of at least the size of the orifice radius was necessary for realistic

values of the turbulence parameters and demonstrated that the jet structure was influenced by the ambient turbulence length and time scales, regardless of the grid resolution when the ambient diffusivity is greater than the jet diffusivity.

Hessel et al. [110] propose a ‘gas sphere model’, which represents an extension to gaseous fuels of the numerical approach usually employed for liquid fuels. Natural gas is injected as fuel parcels, namely gaseous spheres, which are vaporized at a certain point of the computational domain. Even if this model demonstrated to be effective in predicting jet penetration and diffusion, it is too far from the physical phenomenon and too arbitrary in the evaluation of the spheres’ drag coefficient and evaporation point. In other papers, Kuo and Bracco [111] modelled transient incompressible jets using a finite difference solution to the equations of motion including the k - ϵ turbulence model. Their results compared well with experimental data, but comparison was presented only for the early stages of the jet development. Their results pertained to incompressible turbulent jets with Reynolds number between 8650 and 135,100.

6.3 GTT-CHEM

In this study, three-dimensional numerical analysis of gas flow, fuel spray and combustion is conducted by means of the GTT-CHEM [100] [101] code, which is a combination of the engine thermo-fluid analysis code GTT [102] developed by the authors with the general-purpose chemical kinetics calculation code CHEMKIN-II [103]. This code can analyse the process of mixture formation under real fuel injection engine conditions on the basis of the discrete droplet model (DDM), because computational sub models for droplet breakup, mutual impingement and coalescence of droplets, spray impingement on walls, formation of liquid film, and vaporization of droplet and liquid film are included in it. In this code, the sub-models for the fuel spray have been took into account and it is possible to calculate the spray behavior. In other to exclude the effects of fuel injection, initial mixture distributions of fuel vapor and air have been set arbitrarily at the bottom dead center (BDC) without using the fuel injection. The scheme of GTT-CHEM code is shown in Figure 6.1. The GTT computer program consists of a set of subroutines controlled by a short main program. The general structure is illustrated in Fig. 6.1, showing a top-to-bottom encompassing the entire

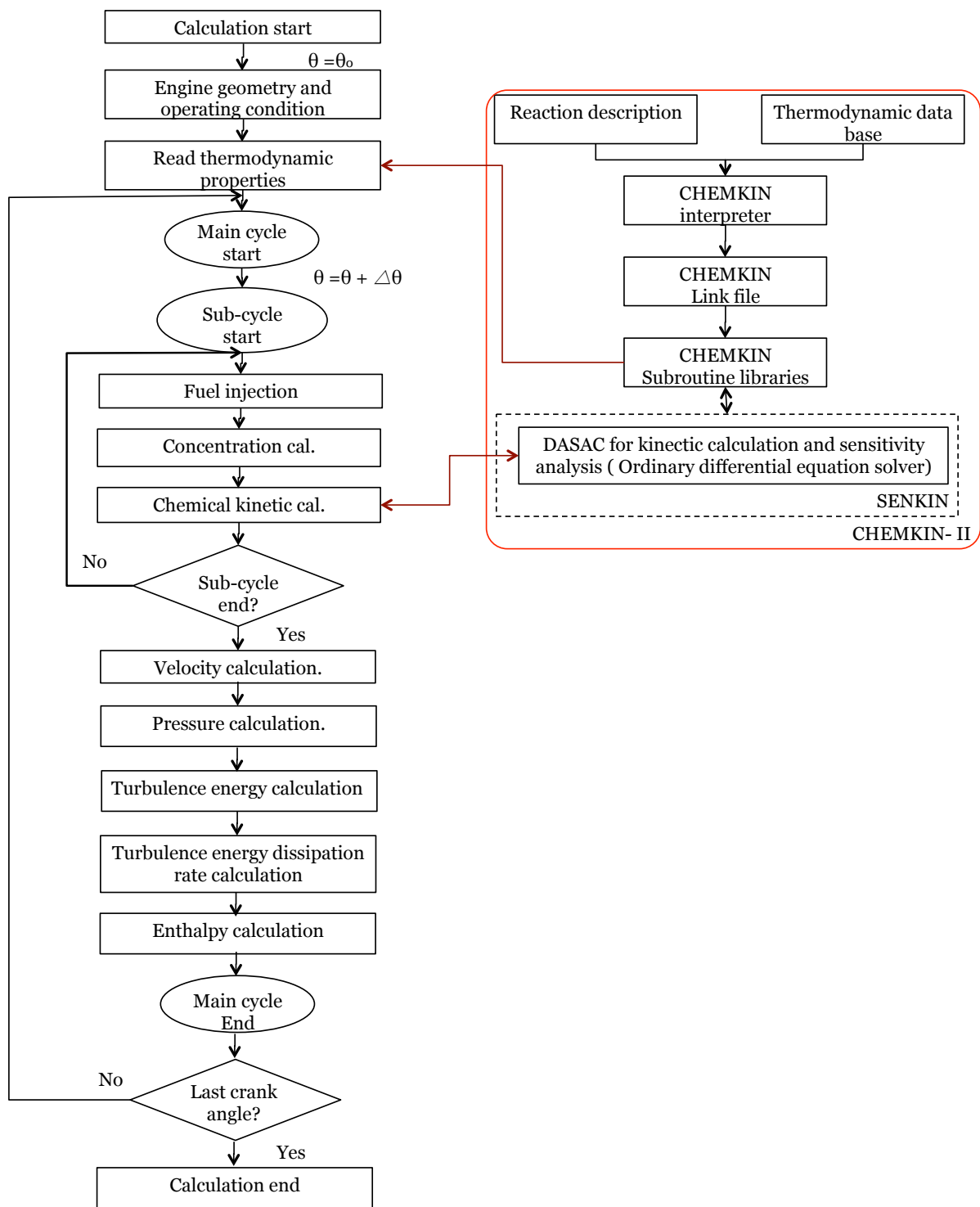


Figure 6.1 GTT-CHEM flow chart

calculation. Beside each box in the flow diagram appears the name(s) of the primary subroutines(s) responsible for the associated task.

6.4 Basic Equation

6.4.1 Gas-Phase

It is assumed that the liquid fuel spray is composed of very small droplets and is sufficiently thin so that the droplets volume may be neglected in the fluid. The effect of gravity on the gas and droplets is ignored. The components of gas phase are air, fuel vapour and combustion products.

The basics equations for the motion of the mixture gas (compressible viscous fluid) are expressed in Cartesian co-ordinates (x, y, z) by the generalized conservation equation:

$$\frac{\partial(\rho\phi)}{\partial t} + \text{div}(\rho\vec{v}\phi - \Gamma_\phi \text{grad}\phi) = S_\phi \quad (6.1)$$

Where ϕ denotes dependent variables; $\phi = 1$ for the continuity equation, $\phi = u, v, w$ for the Navier-Stokes equations, $\phi = h$ for the energy equation, $\phi = Y_j$ for the transport equation of the mass fraction of each gas component, and $\phi = k, \varepsilon$ for the k and ε equations. Γ_ϕ and S_ϕ are the effective diffusion coefficient and the source term, respectively which are shown in Table 5. In Table 5, $\rho_v, (F_l)_x, (F_l)_y, (F_l)_z, Q_l$ are the terms expressing the interaction between the gas and the fuel droplets of liquid film. Namely, these terms are the vaporized fuel mass and the momentum and heat loss by the droplets and liquid film per unit time and unit volume of the mixture gas. The terms Q_r and Y_j in Table 5 represent the rate of chemical heat release and the rate of Y_j change due to chemical reaction, respectively. For the k - ε model, the coefficients shown in Table 6 are used. The mixture gas is assumed to be an ideal gas conforming to the equations $p = \rho RT$.

6.4.2 Droplet

In the GTT code, millions of droplets of various sizes in a spray are treated by the Discrete Droplet Model (DDM) which was employed in the KIVA code [104]. Namely those numerous droplets are represented by thousand of Droplet Parcels, each of which contains droplets having same size and the identical physical properties, and the behaviour of the spray is simulated by calculating the behaviour of those representative particles statistically using a Monte Carlo sampling technique. The breakup of droplets and also the collision and

Table 5 Equations for ϕ , Γ_ϕ and S_ϕ

Equation	ϕ	Γ_ϕ	S_ϕ
Mass	1	0	$\dot{\rho}_v$
Momentum	u	μ_{eff}	$-\frac{\partial p}{\partial x} + \frac{1}{3} \frac{\partial}{\partial x} (\mu_{\text{eff}} \text{div } \vec{v}) - \frac{2}{3} \frac{\partial(\rho k)}{\partial x} + (F_t)_x$
	v	μ_{eff}	$-\frac{\partial p}{\partial y} + \frac{1}{3} \frac{\partial}{\partial y} (\mu_{\text{eff}} \text{div } \vec{v}) - \frac{2}{3} \frac{\partial(\rho k)}{\partial y} + (F_t)_y$
	w	μ_{eff}	$-\frac{\partial p}{\partial z} + \frac{1}{3} \frac{\partial}{\partial z} (\mu_{\text{eff}} \text{div } \vec{v}) - \frac{2}{3} \frac{\partial(\rho k)}{\partial z} + (F_t)_z$
Enthalpy	h	$\left(\frac{\mu}{\sigma_h}\right)_{\text{eff}}$	$\frac{\partial p}{\partial t} + u \frac{\partial p}{\partial x} + v \frac{\partial p}{\partial y} + w \frac{\partial p}{\partial z} + \Phi - \frac{2}{3} \rho k \text{div } \vec{v} + \dot{Q}_l + \dot{Q}_r$
Concentration	Y_j	$\frac{\mu_{\text{eff}}}{S_c}$	$\rho \dot{Y}_j$
Turbulence energy	k	$\frac{\mu_{\text{eff}}}{\sigma_k}$	$G - \rho \epsilon$
Turbulence energy dissipation rate	ϵ	$\frac{\mu_{\text{eff}}}{\sigma_\epsilon}$	$\frac{\epsilon}{k} (C_1 G - C_2 \rho \epsilon) + C_3 \rho \epsilon \text{div } \vec{v}$

Note:

$$\Phi = \mu_{\text{eff}} \left[2 \left\{ \left(\frac{\partial u}{\partial x} \right)^2 + \left(\frac{\partial v}{\partial y} \right)^2 + \left(\frac{\partial w}{\partial z} \right)^2 \right\} + \left(\frac{\partial u}{\partial y} + \frac{\partial v}{\partial x} \right)^2 + \left(\frac{\partial v}{\partial z} + \frac{\partial w}{\partial y} \right)^2 + \left(\frac{\partial w}{\partial x} + \frac{\partial u}{\partial z} \right)^2 - \frac{2}{3} (\text{div } \vec{v})^2 \right]$$

$$G = \Phi - \frac{2}{3} \rho k \text{div } \vec{v}, \quad \mu_{\text{eff}} = \mu_{\text{lam}} + \mu_{\text{turb}}, \quad \mu_{\text{turb}} = C_\mu \frac{\rho k^2}{\epsilon}, \quad \left(\frac{\mu}{\sigma_h} \right)_{\text{eff}} = \left(\frac{\mu}{\sigma_h} \right)_{\text{lam}} + \left(\frac{\mu}{\sigma_h} \right)_{\text{turb}}$$

Table 6 Constant in the k-ε model

$C_1 = 1.44$	$C_2 = 1.92$	$C_3 = -0.373$	$C_\mu = 0.09$
$\sigma_k = 1.0$	$\sigma_\epsilon = 1.3$	$(\sigma_h)_{\text{lam}} = 0.71$	$(\sigma_h)_{\text{turb}} = 0.9$

coalescence of droplets can be taken into consideration in this model. It is assume that the shape of each droplet is spherical and the temperature distribution in the droplet is uniform.

The position of each droplet x_d , is determined from the equation,

$$\frac{d\bar{x}_d}{dt} = \bar{v}_d \quad (6.2)$$

The droplet velocity \bar{v}_d is calculated from the following equations,

$$\frac{d(m_d \bar{v}_d)}{dt} = (\pi/2) \rho r_d^2 \times (\vec{v} + \hat{v} - \bar{v}_d) |(\vec{v} + \hat{v} - \bar{v}_d)| C_D \quad (6.3)$$

Here \vec{v} and \hat{v} are the mean and turbulent components of gas velocity vector respectively where the magnitude of \hat{v} are chosen according to a Gaussian distribution, and the drag coefficient is C_D given by,

$$C_D = \begin{cases} 24[1 + (1/6)Re_d^{2/3}] & \text{for } Re_d \leq 1000 \\ 0.42 & \text{for } Re_d > 1000 \end{cases}$$

$$Re_d = 2\rho r_d |\vec{v} + \hat{v} - \vec{v}_d|/\mu_g$$

$$\mu_g = A_1 \hat{T}^{3/2}/(\hat{T} + A_2) \text{ (} A_1 \text{ and } A_2 \text{ are constants),}$$

$$\hat{T} = \frac{T + 2T_d}{3}$$

The variation of the droplet radius r_d due to evaporation is calculated from the following equations [104]:

$$\frac{dr_d}{dx} = - \left[\frac{(\rho D)_g}{(2\rho_l r_d)} \right] [(C^* - C)/(1 - C^*)] Sh_d \quad (6.4)$$

Where,

$$Sh_d = (2.0 + 0.6 Re_d^{1/2})$$

$$Sc_d = \mu_g/(\rho D)_g$$

$$B_d = (C^* - C)/(1 - C^*)$$

$$(\rho D)_g = D_1 \hat{T}^{D_2} \text{ (} D_1 \text{ and } D_2 \text{ are constants)}$$

The fuel vapour concentration at the droplet surface, C^* , is determine from the equation

$$C^* = M_1 / \left[M_1 + M_0 \left(\frac{p}{p_v} - 1 \right) \right]$$

Where M_1 and M_0 are the molecular weight of fuel vapour and that of mixture gas exclusive of fuel vapour, respectively, and p_v is the equilibrium fuel vapour pressure at T_d .

6.5 Method of Calculation

By integrating the generalized conservation equation, Eq.(6.1) in an arbitrarily-shaped hexahedral control volume, whose surface can move individually with arbitrary velocity v_s , the following equation is obtained, where the Gauss theorem is applied,

$$\frac{d}{dx} \iiint_V (\rho\phi) dV + \iint_S (\rho\phi)(\vec{v} - \vec{v}_S) \cdot \vec{n} dS - \iint_S (\Gamma_\phi \text{grad } \phi) \cdot \vec{n} dS = \iiint_V S_\phi dV. \quad (6.5)$$

The integrated conservation equation (6.5) is discretized using the authors' GTT (Generalized Tank and Tube) method, namely a finite volume method which introduces the technique of general coordinate transformation into Tank and Tube method of Gosman and Ideriah so that boundary fitted non-orthogonal structured grids can be used for arbitrarily-shaped regions with moving boundaries. Concerning the allocation of the dependent variables on grid points, the staggered arrangement is employed. As shown in Fig. 6.2, the gas velocity vector \vec{v} is allocated at each vertex of the control volume, and the other variables p, ρ, h, Y_j, k and ϵ are allocated at the centre of the control volume. Each control volume in the physical domain (x, y, z, t) is transformed into a cube in the calculation domain, which is expressed by general curvilinear coordinates (ξ, η, ζ, τ) , where $\tau = t$.

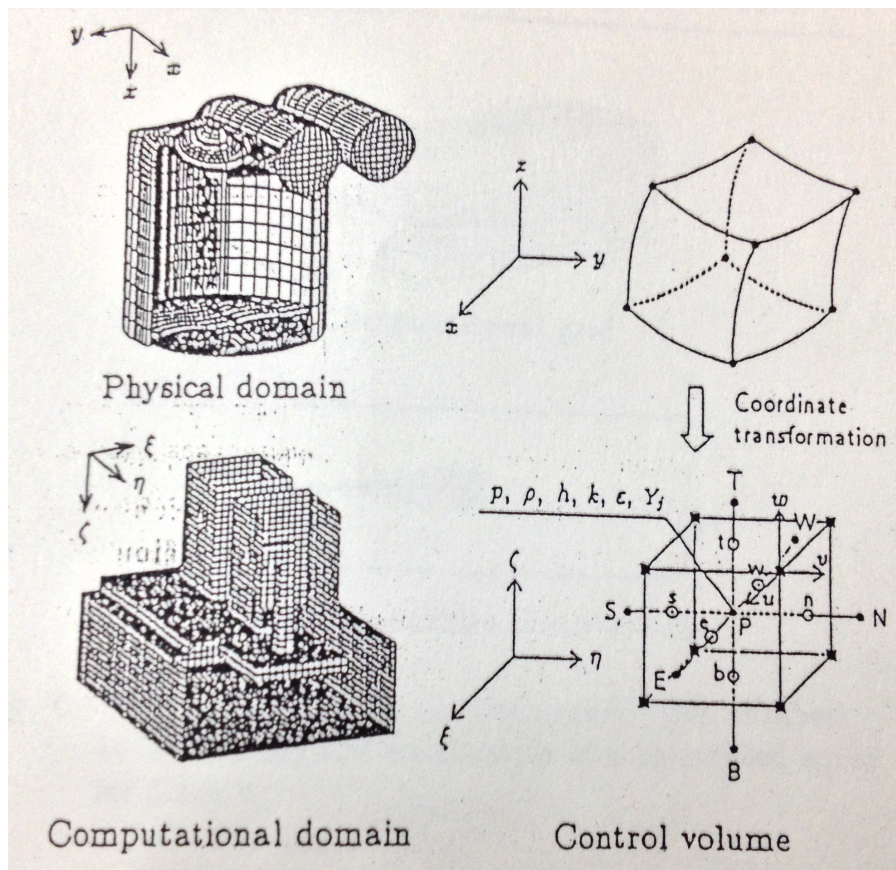


Figure 6.2 Coordinate system and control volume

As to the differencing scheme of convection terms, the third order TVD (Total Variation Diminishing) scheme of Chakravarthy-Osher is used for the Navier-Stokes equation, and the Hybrid scheme is used for the conservation equation of enthalpy, turbulence energy k and its dissipation rate ϵ . These conservation equations are solved every time step on the basis of fully implicit algorithm where pressure-velocity coupling is accomplished by means of the SIMPLEC (Semi-Implicit Method for Pressure Linked Equations consistent) algorithm, which brings about quicker convergence than the SIMPLE (Semi-Implicit Method for Pressure Linked Equations) algorithm does.

In order to avoid smearing of the solution of concentration field due to false diffusion, the transport equation of fuel vapour concentration under non-combustion condition is calculated using the CIP (Cubic Interpolated Pseudo-Particle) method whose false diffusion is very small since this method calculates the convection term explicitly in Lagrangian way. When the combustion process of the mixture is analysed, the TVD scheme is used to calculate all the transport equations of the mass fractions of gas components for saving the required memories on a computer. The CIP method requires much more memories. The time increment Δt in a main cycle, where the velocity field is calculated implicitly, is set at 0.05-0.15 ms. The behaviour of droplets, that of liquid film and the concentration of each of each gas components are calculated explicitly in sub cycles with a smaller time increment Δt_s ($= 1/10-1/100 \Delta t$).

6.6 Gas-Phase solution

GTT-CHEM offers a solution for gas phase flows within a chamber and for the propagation of a liquid spray (liquid phase) within that chamber. Only the gas phase flow is discussed in this chapter. The gas phase solution is a finite-volume approximation to two- or three-dimensional compressible equations of motion. An arbitrary number of species, treated as a mixture of ideal gases, can be specified. The equations are typical Navier-Stokes equations for a mixture of gases.

6.6.1 Gas Parcel Method

Fujimoto et al. developed Gas Parcel method in GTT for numerically analyzing the gas jets [112]. Figure 6.3 shows the typical hydrogen jet, which is generated by gas parcel method in GTT solver. Standard $k-\varepsilon$ turbulence model was used for this method. The calculation technique of the Gas parcel method applied a discrete droplet model (DDM) for considering the local momentum in the jet calculation. The majority of computational spray models employ the discrete droplet model (DDM) [113]. The DDM has been employed for a wide range of spray simulations, particularly fuel sprays in engines [114],[115]. The DDM involves solving the equations of motion for a turbulent carrier gas in a Eulerian scheme, and integrating Lagrangian equations of motion for liquid droplets along true path lines. These two calculation schemes, and therefore the two phases, are then coupled through source terms in the transport equations. The Lagrange formulation introduces the concept of parcel, which identical no interacting droplets termed a ‘parcel’. DDM model treats the spray droplets as parcels. Each parcel represents a group of droplets which all have the same characteristics (size, velocity, etc.). All of the parcels have the same amount of mass, and are followed by the code using a Lagrangian approach. Droplet parcels are introduced in the flow domain with initial conditions of position, size, velocity, temperature and number of particles in the parcel. The space where the droplets are newly introduced embraces more cells, so that the high velocity gradients generated by the momentum transformer can be better distribution and solved in the near nozzle region. The position of each droplet parcel at a new time step is calculated according to the following equation,

$$\vec{x}_d^n = \vec{x}_d^0 + \vec{v}_d^0 \Delta t_s \quad (6.6)$$

Here, n is the index on the new time step; 0 indicates the previous time step. The equation for the droplet velocity, radius and temperature are calculated by the finite difference method. The gas particles have lost momentum. It was assumed that the momentum, \vec{S}_d applied to the gas phase multiplied by the number of gas particles, n_d that comprise the gas parcel.

$$\vec{S}_d = -C_{dg} n_d (m_d^n \vec{v}_d^n - m_d^0 \vec{v}_d^0) \quad (6.7)$$




















	0.2 ms	0.5 ms	1.0 ms	2.0 ms
Exp. Data				
Case-H-1				
Case-H-2				
Case-H-3				
Case-H-4				

Figure 6.3 Comparison of hydrogen jet between experiment and gas parcel method in GTT [104].

Where, m_d represents the mass of the gas particles, C_{dg} is the correction factor (momentum coefficient is corrected until the jet width comparable to the grid spacing, while the gas parcel gradually moving into the gas phase). Further, n_d is represented by the following formula,

$$n_d = m_g / \left(\frac{4}{3} \pi r_d^3 \rho_d \right) \quad (6.8)$$

Where, m_g is the mass of gas injection represents of each parcel (the total injected mass divided by the number of parcels to be injected), ρ_d is the density of the gas injection, r_d is the radius of the gas particles.

The droplet acceleration \vec{a}_d has contributions due to aerodynamic drag and gravitational force: The acceleration, a_d equations of the gas particles motion are as follows,

$$\vec{a}_d = \frac{3 \rho_g}{8 \rho_d} \frac{|\vec{v} + \dot{\vec{v}} - \vec{v}_d|}{r_d} (\vec{v} + \dot{\vec{v}} - \vec{v}_d) C_D \quad (6.9)$$

Where ρ_g is the density of the gas phase, \vec{v} is the gas phase velocity and $\dot{\vec{v}}$ is variation component. Further C_D is the drag coefficient, which was used for the value of that sphere.

The particles and fluid interact by exchanging mass, momentum, and energy. The momentum exchange is treated by implicit coupling procedures to avoid the prohibitively small time steps that would otherwise be necessary. Accurate calculation of mass and energy exchange is ensured by automatic reductions in the time step when the exchange rates become large. Turbulence effects on the droplets are accounted for in one of two ways. When the time step is smaller than the droplet turbulence correlation time, a fluctuating component is added to the local mean gas velocity when calculating each particle's mass, momentum, and energy exchange with the gas. When the time step exceeds the turbulence correlation time, turbulent changes in droplet position and velocity are chosen randomly from analytically derived probability distributions for these changes. The droplet turbulence correlation time, t_{turb} is given by,

$$t_{turb} = \min \left(\frac{k}{\varepsilon}, C_{ps} \frac{k^{\frac{3}{2}}}{\varepsilon} \frac{1}{|\vec{v} + \dot{\vec{v}} - \vec{v}_d|} \right) \quad (6.10)$$

Where C_{ps} is an empirical constant with value 0.16432. Thus the t_{turb} is the minimum of an eddy breakup time and a time for the droplet to traverse an eddy.

Since the difference between the momentum of the gas phase and the parcel is reduced, the interaction between the gas phases is reduced, when the relative velocity between the gas

phases is less than the threshold value is excluded from the calculation by removing the parcel. In this study, the threshold was set to 0.1 m / s.

6.6.2 Wall boundary condition

The wall boundary conditions are briefly described here. The turbulent law-of-the-wall implemented in GTT-CHEM is used to bridge the turbulence model with the wall. The law of the wall matches the tangential components to a logarithmic profile in the boundary layer. Both heat transfer and wall shear stresses are handled by the law-of-the-wall. Either adiabatic or constant temperature wall can be specified. The constant-temperature wall condition was applied in the simulations, being more representative of engine conditions than the adiabatic option. Some assumptions involved in the law of the wall function may be violated in engines. In particular for the modeling of transient jets, if the jet tip were propagating in contact with the wall, the assumption of quasi-steadiness leading to the derivation of the wall function would be violated in the vicinity of the vortex head. The wall function is properly evaluated when the grid point closest to the wall is within the turbulent boundary layer. This may be difficult to accomplish if a jet travels at high velocity near a wall, particularly in the vicinity of the nozzle. Therefore the possibility of inaccuracy is kept in mind in interpreting computational results in which these conditions occur.

6.6.3 Solution algorithm

The basic equations are obtained by integrating differential terms over the control volumes corresponding to the cell volumes. Each computational time step is divided in two phases, a Lagrangian phase and a rezone phase. In the Lagrangian phase the vertices move with the flow, such that there is no convection across the cell faces. In the rezone phase, the flow is frozen, and the mesh is moved to the appropriate position, the convection terms being calculated during that operation. The temporal difference solution is largely implicit, which permits one to adjust the time-step on accuracy conditions rather than stability conditions. All diffusion terms and pressure wave propagation terms are solved during the Lagrangian phase, using an algorithm similar to SIMPLE. Explicit differencing is used in the convection phase, with sub-cycling of the time-step if needed to satisfy the Courant stability condition. Finally,

GTT-CHEM uses a quasi-second order upwind scheme for convection, which improves false diffusion tendencies.

6.6.4 Modification of GTT code

GTT does not readily have inputs for gaseous injections. Boundary conditions corresponding to the injector/chamber interface must therefore be implemented. At the injector/chamber interface, the velocity, temperature and density of the incoming gas must be set. In the current project, the computational domain did not extend within the nozzle area. Figure 6.4 shows the injector/chamber interface for a 2-D grid with downward injection originating from the center of the top wall, at the symmetry axis. The chamber in this case would have the shape of a cylinder (as that of Fig. 6.6), with the jet propagating along its axis. The velocity and temperature must be provided at the vertices within the nozzle/chamber interface (a, b and c). The density, internal energy, turbulent length scale and turbulent kinetic energy flux across the cell faces (a-b, b-c) in the interface region must also be provided. The temperature, velocity and density are inputs to the solution.

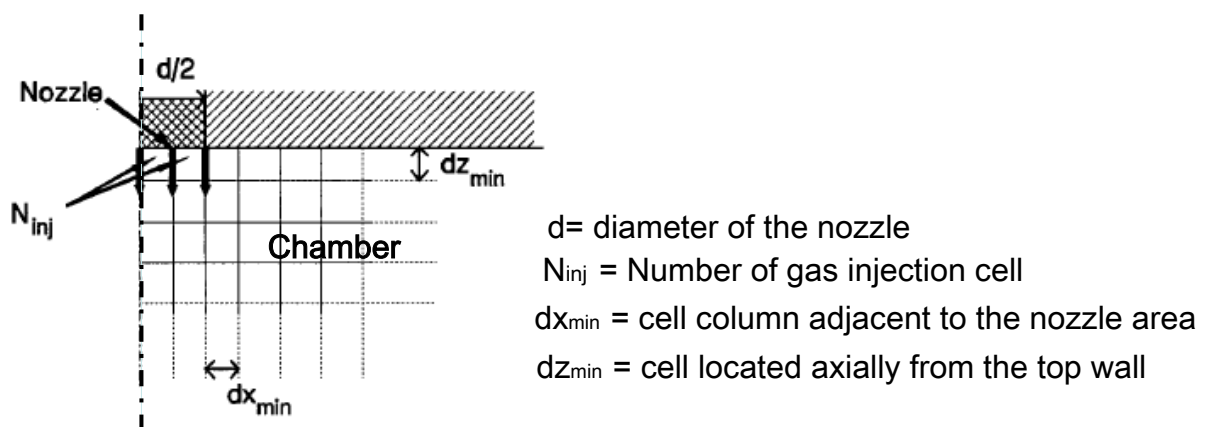


Figure 6.4 Nozzle interface in computational mesh

6.7 The Computing Mesh

In GTT 3D CFD simulation, we used Kmesh program for generating the mesh where source codes are written in Fortran language. This program is base on KIVA Computing Mesh, so variables is defined like ones in KIVA formulation. The right boundary is cylinder wall, and the left boundary is shrunk to zero size to become the central axis. The top boundary is cylinder head, which is flat in this program, and the bottom boundary is the moving piston face, which maybe flat or contain a bowl.

To use this program, it is necessary to input the dimensions of the desired piston geometry by laying out a haft cross section of it on graph paper before, define grid points along the piston silhouette, starting at the bowl axis, and ending at the cylinder wall. For each point, program requires the logical coordinates (i and k), and the physical coordinates (r and z), relative to $z = 0.0$ being the lowest z -coordinate. Besides, the user must enter some data like length of cylinder, namely, the stroke of engine, and the values of OFFSET in both of x -, and y -directions (these values will be 0.0 and 0.0, if piston have an axisymmetric geometry). Because some piston face is designed in ellipse profile, so KEX and KEY are introduced as the ratio between two axis of ellipse along x - and y -directions. (If piston is in circle profile, these values will be 1.0 and 1.0). Corresponding figure for setting the shape of the main engine are shown in figure 6.5 (a) and the cavity shape data for the cavity to form are shown in Fig 6.5 (b).

➤ About variables in program

- */ NPO - number of points defining the piston outline (cf. KIVA)
- */ NI0 - number of i planes (cf. KIVA)
- */ NKSUM - total number of k planes including the cylinder part
- */ ZSTROKE - stroke (cm)
- */ ZPTDC - clearance at TDC (cm)
- */ KEX - a value deciding the horizontal cavity profile in circle or in ellipse along x -direction
- */ KEY - a value deciding the horizontal cavity profile in circle or in ellipse along y -direction
- */ XOFFSET - cavity offset in x -direction (cm)
- */ YOFFSET - cavity offset in y -direction (cm)
- */ ZFACTOR - a factor for ZPO to adjust the compression ratio

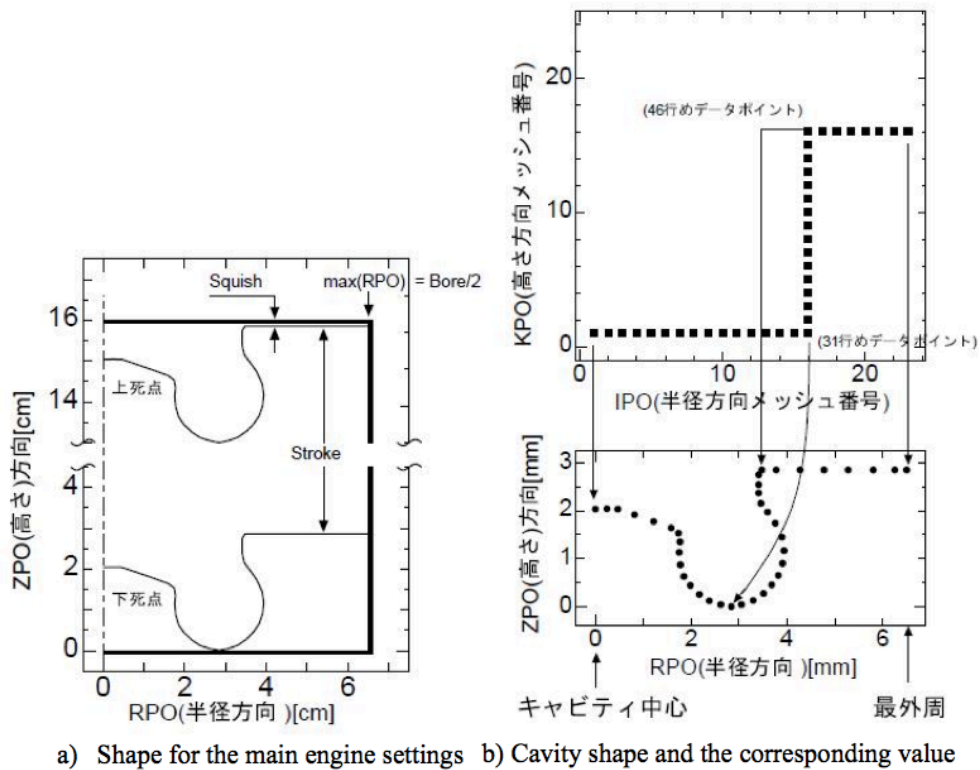


Figure 6.5 Correspondence of data file and shape

6.8 Simulation case for constant volume vessel

6.8.1 Mesh for constant volume vessel

The GTT formulation is based on (x, y, z) Cartesian geometry and is applicable to cylindrical ($CYL = 1.0$) or planar ($CYL = 0.0$) calculations in either two or three space dimensions. The mesh is composed of a block of cells in logic space, NX cells in the i -direction, by NY cells in the j -direction, by NZ cells in the k -direction. Figure 6.6 shows the three-dimensional mesh used in these study. The mesh is made of 70×70 radial cells and 39 axial cells. The radius of the modelled chamber is 80 mm, and the length is 125 mm.

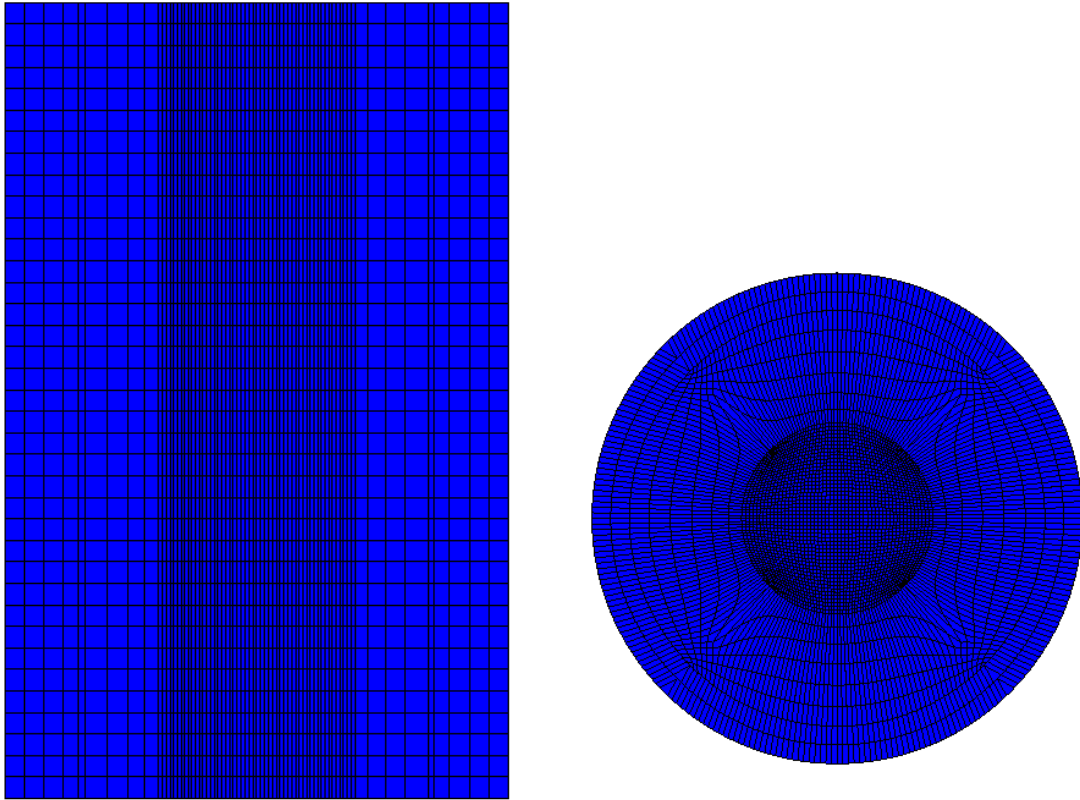


Figure 6.6 3D mesh used in simulating hydrogen jet.

6.8.2 Grid dependency

A study on the grid dependence is conducted in this study. A cylindrical domain of 8 cm in diameter and 12.5 cm in height is used for this purpose. Hydrogen is injected from the center of the top surface. The nozzle diameter is 1 mm. The injection pressure is 5 MPa and the nitrogen filled chamber pressure is 1.5. The temperatures at the injector and chamber are 300K. Three different computational grids used are labelled in Fig. 6.7 as a) (70x70x19 cells), b) (70x70x29 cells), and c) (70x70x39). As shown in Fig. 6.7, it can be seen that the gas penetrations after 1 ms are not similar for all the cases. It can be seen that the prediction of penetration is affected by the mesh resolution in both directions, radial and axial. The influence of radial resolution is evidently stronger than the axial. In Fig. 6.7 a) grid results shows in a higher diffusion of the hydrogen jet compared to the other two cases. As a result, an unphysical jet shape is predicted using the coarse mesh. This is caused by the relatively big minimal volumes of cells in these meshes (for the two coarse meshes), which delays the void fraction in these cells from reaching the threshold value. A typical direct photograph of the jet

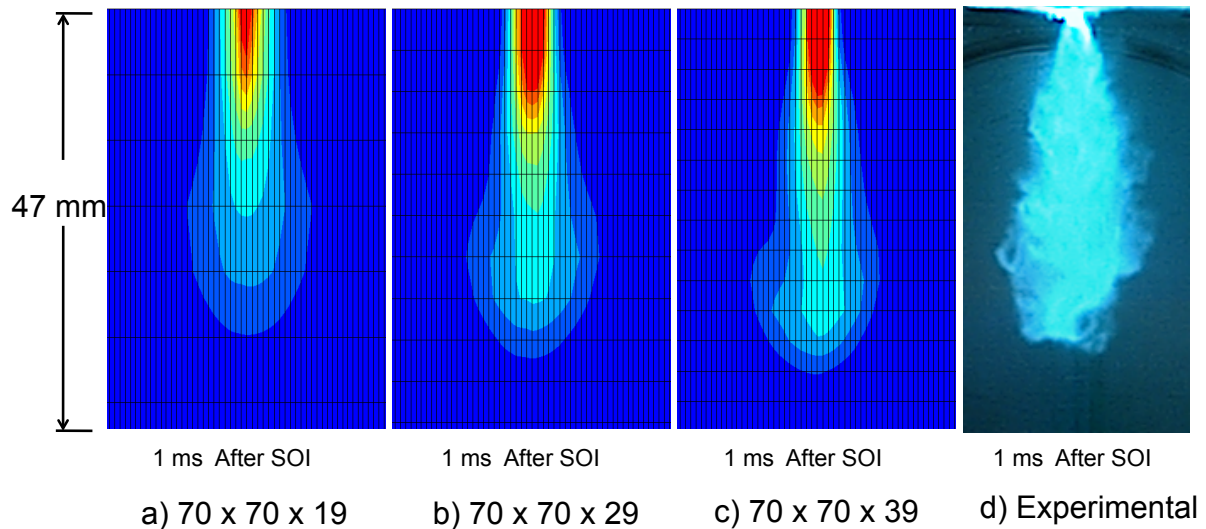


Figure 6.7 Simulated hydrogen mass fraction contours in a constant volume chamber using different grid sizes along with experimental hydrogen jet image

is also shown in Fig. 6.7. It is seen that upstream the jet flow, the flow is very smooth possibly due to the very small eddies produced near the jet flow in this region of the jet. However, further downstream the roughness of the jet boundary is clearly visible and the existence of much larger eddies which are also visible is verified by the photograph to a good extent. The photograph also shows that the jet flow is actually not symmetrical about the jet axis.

6.8.3 Jets penetration in a constant volume vessel (non-reactive)

The gas parcel model in GTT was applied to simulate the experiments of hydrogen injection. As with most model development work, results from simple experiments were desired for testing the model during development. Hydrogen is injected at a pressure of 5 MPa and temperature of 300 K to a constant volume chamber of nitrogen with pressure 1.5 MPa and temperature 300 K. The nozzle diameter is 1mm. The computational domain used in the simulation consists of a constant volume cylindrical chamber with 80 mm in diameter and 125 mm in height. The mesh is divided into 70x70x39 cells. The average cell size is 0.6 mm. Details of the simulation case are given in Table 7.

Table 7 Condition in constant volume chamber case

Medium	Hydrogen injected into ambient nitrogen
Injection duration	4 ms
Nozzle diameter	1.0 mm
Injection pressure	5 MPa
Injection velocity	300 m/s, 500 m/s ,
Parcel number	8000

In the present case of hydrogen gas jet, the eddy Schmidt number, Sc_t and Prandtl number, Pr_t , used were 0.7 and 1.0 respectively. The initial mass concentration at the nozzle exit was set equal to unity assuming pure hydrogen gas was injected. This means the initial mole fraction was also set to unity at the nozzle exit. The time step for the prediction results presented herein was 0.15 ms. Mass flow rate and momentum injection rate were matched by assuming a square wave velocity profile, assigning the injection velocity and total mass injected during the injection duration, and assigning a gaseous sphere radius of 500 microns.

Figure 6.8 shows the contours of hydrogen mass fraction distributions at various times under different injection velocity after the start of injection. Results show good agreement between the numerical and experiment data, as shown in Figure 4.4. The region very near the inflow boundaries, the jet shape for injection velocity 300 m/s predicted using a gas parcel method are in good agreement with the result obtained using the high-speed video camera.

Development of the gas velocity is depicted in Fig. 6.9 by the axial-section vector plots at four characteristic times during injection. The maximum velocity is found along the jet axis. As expected, during injection the maximum gas velocity is located near the injector and is of the order of 300 m/s, Later on, when injection ceases, the location of maximum velocity moves downstream with the jet and the velocity magnitude decreases. Careful inspection of the plots reveals a toroidal vortex formed at the outer edge of the jet.

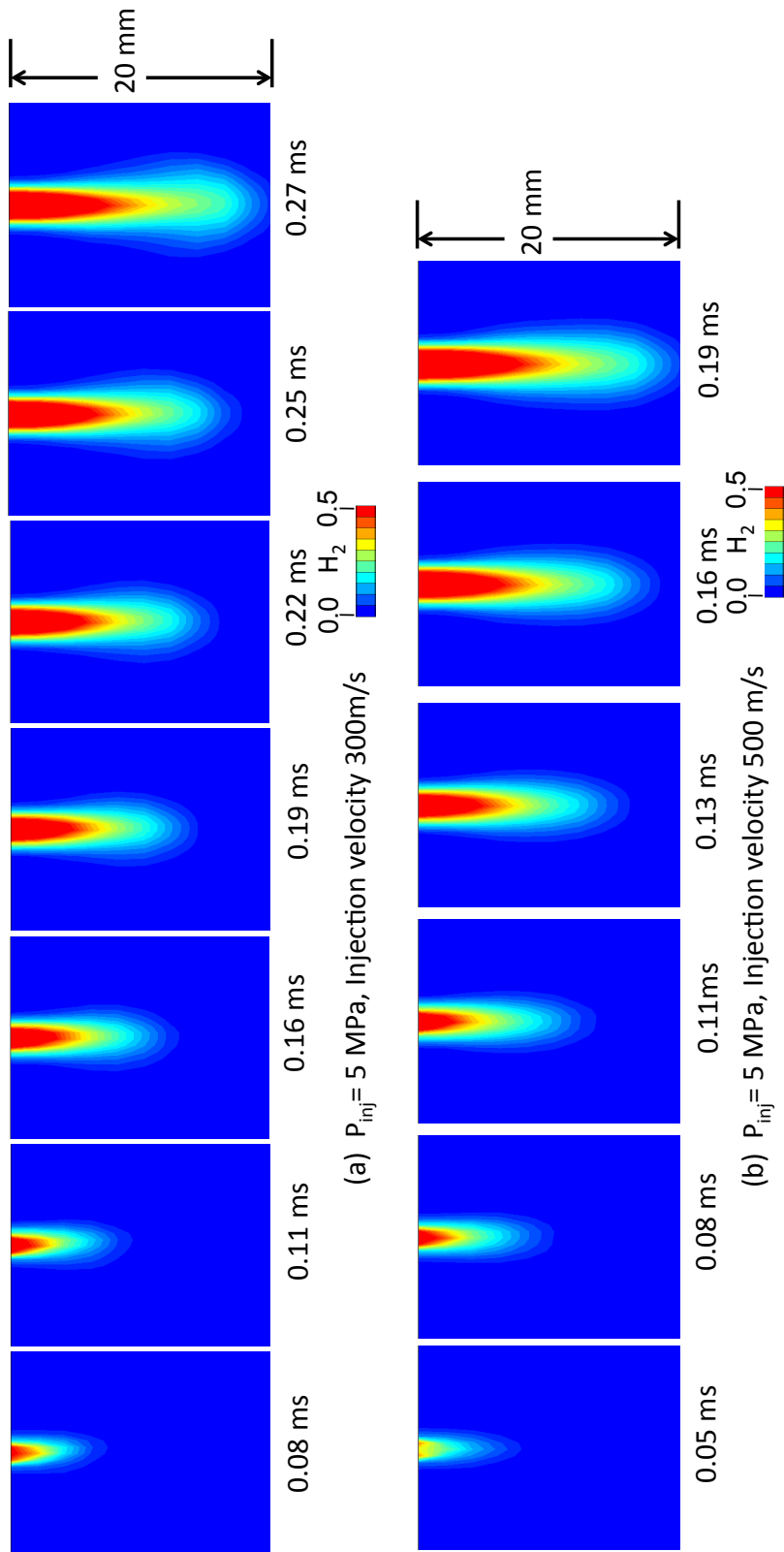


Figure 6.8 Mass fraction distribution of a hydrogen gas jet injected into a constant volume chamber filled with nitrogen.

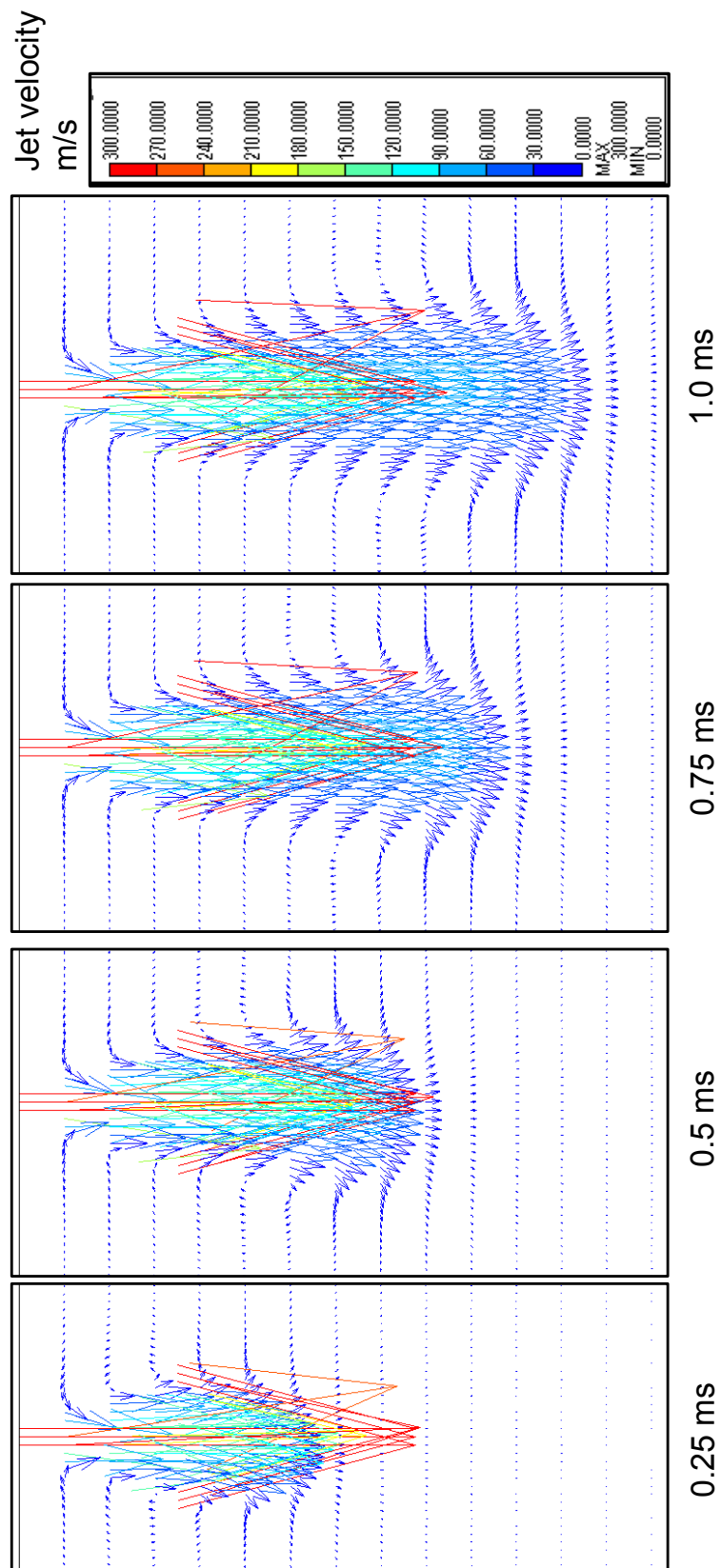


Figure 6.9 Jet velocity vector during injection. (Injection velocity 300 m/s)

6.8.4 Single jet validation

The gas parcel model was applied to simulate the experiments of hydrogen injection. Hydrogen is injected at a pressure of 5MPa and temperature of 300K to a constant volume chamber of nitrogen with pressure 1.5 MPa and temperature 300K. The nozzle diameter is 1 mm. The computational domain used in the simulation consists of a constant volume cylindrical chamber with 80 mm in diameter and 125 mm in height. The domain is meshed using an O-grid scheme with the circular facing assumed as a logical square. The domain is divided into 70x70x19 cells. The average cell size is 0.6 mm. The jet tip penetration is measured as the penetration of 3% mass fraction of hydrogen.

The predicted penetration in GTT is compared with the measured experimental penetration, as shown in Figure 6.10. The experimental penetration was determined using axial penetration distances were obtained from high-speed direct images. Assuming mass diffusion was negligibly small compared to mass convection in the axial direction during transient jet propulsion. In GTT, the initial jet velocity, $U_0 = 500$ m/s and 300 m/s individually was selected at boundary condition to simulate the hydrogen jet. The predicted penetration rate shows the higher rate initially as well as experimental penetration. As the jet expands, the tip penetration gradually slows down. Experimental measured and predicted jet tip penetration after 0.4 ms distributions coincided when U_0 was set at 300 m/s which corresponds to Mach number 0.25 approximately. From this low initial jet speed, it was therefore inferred that despite the seemingly high injection pressure in the gas reservoir, the experimental jet flow was most probably incompressible and subsonic. It seems the actual effective injection pressure inside the nozzle was considerably lower than the injection pressure. The model predicts the same trend as in the experimental data. Overall, good agreement between simulation and experiment is obtained. Despite that the predicted penetration rate is higher than the experimental data. The numerical simulation predicts a higher penetration at the beginning of the injection process.

The present model was also used theoretical correlation for model validation. Dent [116] has proposed the following semi-empirical relation for the temporal streamwise penetration, X_{jp} , of a transient, incompressible or compressible jet,

$$X_{jp} = \sqrt{8U_0 d_e t} \quad (6.11)$$

Where d_e is the equivalent diameter as given by Hinze [27],

$$d_e = d_o \sqrt{\frac{\rho_g}{\rho_a}} \quad (6.12)$$

where , ρ_g and ρ_a refer to density of gas and surrounding medium respectively, U_0 is the jet initial velocity , d_o is the orifice diameter and t is time after jet initiation, with $t \geq 1$ ms generally used for better accuracy. The orifice diameter of 1 mm and the jet initial velocity $U_0 = 300$ m/s and 500 m/s are used in above equation to generate the theoretical penetration. The injection pressure and temperature are 5 MPa and 300 K, respectively, and the pressure and temperature of nitrogen in the chamber are 1.5 MPa and 300 K, respectively. The predicted jet penetration is compared with the theoretical results, as shown in Fig. 6.11. Good levels of agreement are obtained by using initial jet velocity 300 m/s with the measured penetration.

According to Hinze [27], the main aim of using the equivalent diameter to check whether the distribution curves of flow variables in constant density flows will coincide with those of flows varying density fluids. In this regards, the equivalent diameter is particularly useful in analysing behaviour of free flows of varying density like compressible jets or incompressible jets discharging into a dissimilar fluid.

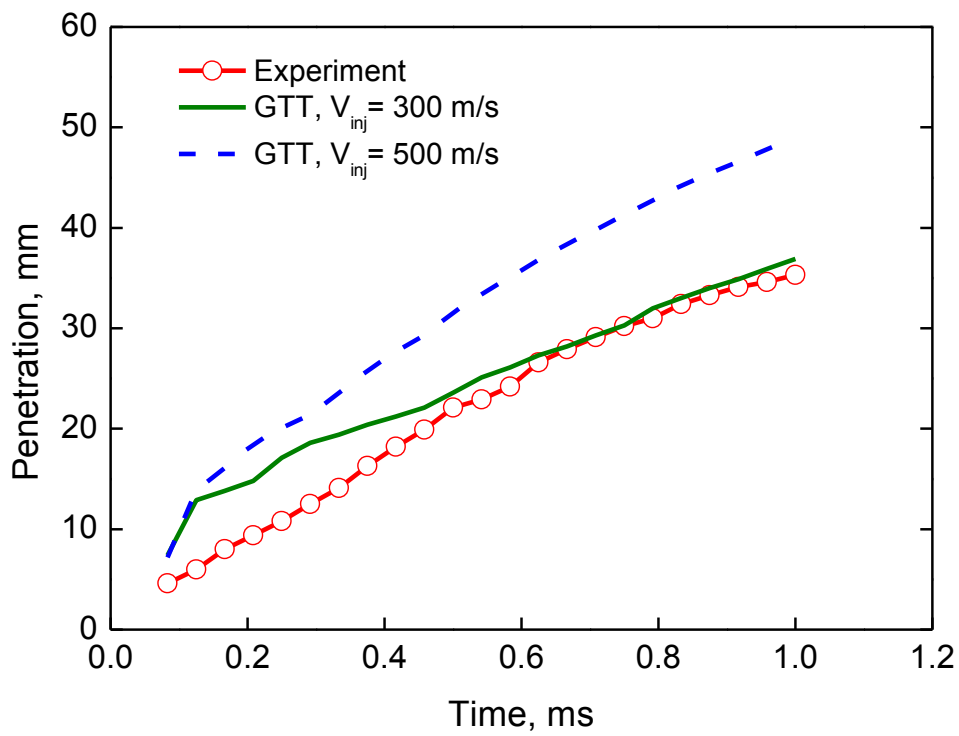


Figure 6.10 Comparisons of experimental and numerical results of the hydrogen jet penetration.

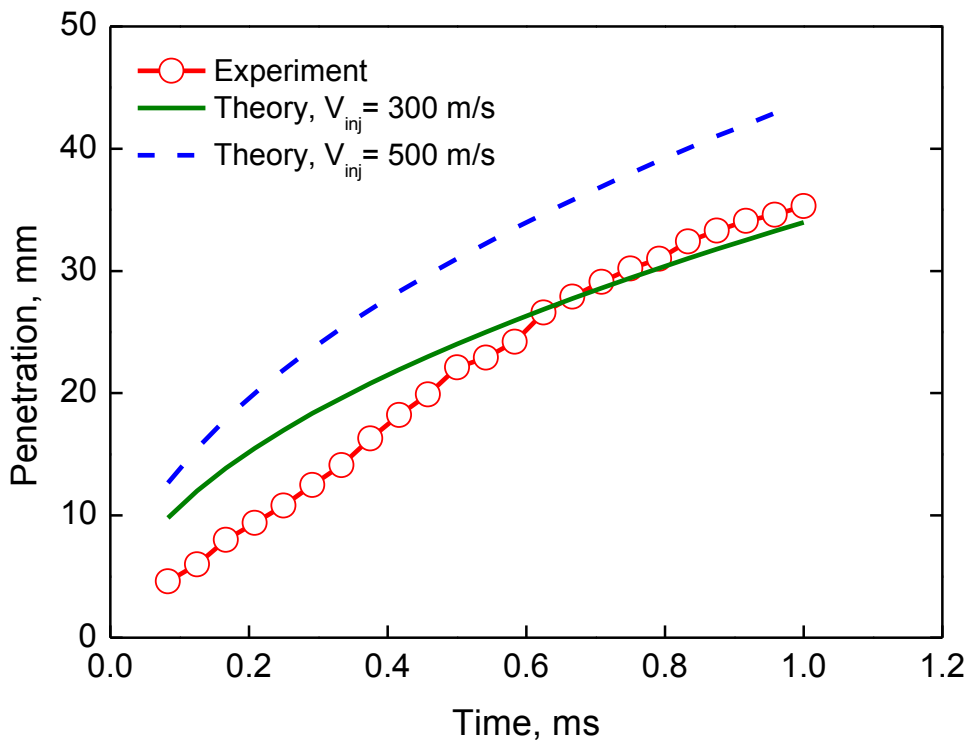


Figure 6.11 Comparisons of theoretical and experimental measured penetrations of a hydrogen jet

6.9 In-cylinder mixture formation in direct injection hydrogen engine

Liquid fuel injection is fairly well characterized and standard engine codes include validated injection models. Gaseous injection in engines is not as simple to model. Typically, gas injection is modeled by specifying boundary elements where a fuel inlet pressure or speed is assigned. This is difficult to implement in the code, requires remeshing for changes in injection parameters (i.e. number of injectors or direction of injection) and it may require fine grid resolution at the nozzle, increasing the computational expense.

The objective of this work is to study the hydrogen mixture formation in direct injection engines. As described in section 6.8, a hydrogen jet model is implemented in GTT CFD code, and the model is validated using the experimental data. In this section, the model is further applied to in-cylinder hydrogen injection and the transient engine cycle is simulated. This study follows a RANS approach combined with k- ϵ model to describe in-cylinder turbulence. The quality of the RANS results is not comparable to more detailed approach such as LES or DNS. The injection parameters are varied and a parametric study is performed to determine the effects of injection parameters on the mixture formation inside the engine.

6.9.1 Computational grid of the engine cylinder

The model was applied to simulate the in-cylinder mixture formation of a two-valve, direct-injection spark-ignition engine. The details of the engine are listed in Table 8. The parameters to be studied include the injection timing, the injector location, and the included angle of injection (i.e., orientation of nozzle). In this study, the quality of the air-fuel mixture is evaluated based on the equivalence ratio distribution in the engine cylinder. Although it is ideal to create a stratified mixture around the spark plug it may be difficult to have quantitative criteria to describe the stratification. Particularly, under direct-injection conditions, there is limited time for mixture preparation.

Table 8 Engine specifications used in simulation.

Piston type	Flat top
Bore (mm)	78
Stroke (mm)	67
Squish (mm)	10
Engine speed	600 rpm
Compression ratio	9.0
Overall equivalence ratio, ϕ	0.22
Hydrogen Injection pressure, MPa	5
Injector orifice	Single hole
Intake pressure, kPa	95
Initial temperature, K	300

Kmesh program is used as a pre-processor to generate the computational grids. The computational mesh is shown in Figure 6.12. The mesh is made of 58 axial cells, 58 radial cells and 39 azimuthal cells. The radius of the modelled chamber is 39 mm, and the length is 67 mm. The mesh consists of approximately 131196 cells. A computational grid of the geometry reduced to the combustion chamber only is used to simulate direct injection and mixture formation. This study focuses on hydrogen direct injection and mixture formation before combustion occurs, therefore only the part of the cycle calculated with the reduced geometry is considered. Because combustion is not modelled, the simulation of the entire exhaust process may not be of significance since the exhaust of combustion products and the mixing of residuals and fresh air are not considered. The only additionally require information is the boundary condition related to the fuel injection. To this aim, the hydrogen mass flux through the nozzle is calculated from the measured mean mass-flow rate, injection duration, and nozzle diameter is set as the boundary condition for the injecting surface.

Hydrogen is injected at a pressure of 5 MPa and the inlet temperature of the injected hydrogen is set to 300K. The mass of hydrogen injected corresponds to an overall equivalence ratio, ϕ of 0.22. Initial ambient air pressure at BDC is set to 95 kPa in this engine simulation. The injector has single holes and nozzle has a diameter of 1 mm. at the bottom-dead-center (BDC). The simulation starts from BDC (180 deg. CA) and ends at 540 deg. CA, which is an appropriate timing to compare with experimental engine cycle.

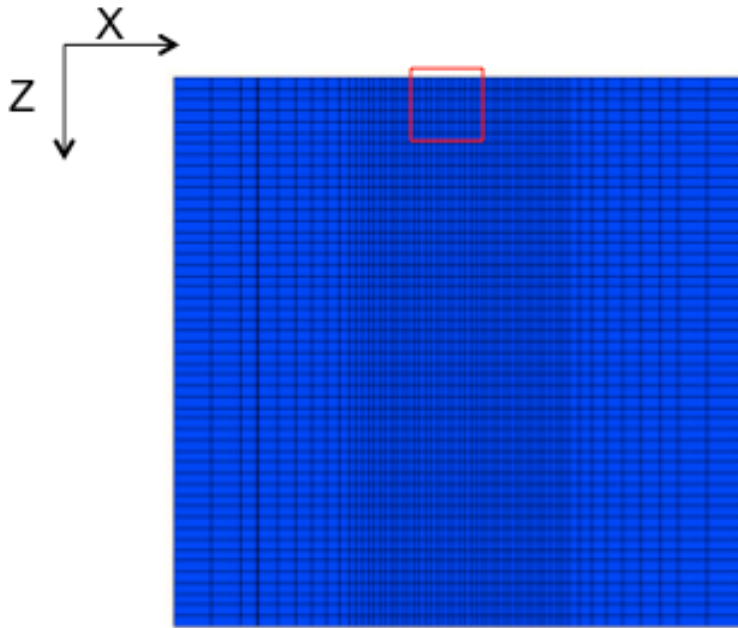


Figure 6.12 Computational grid ($58 \times 58 \times 39$) of the engine.

6.9.2 Qualitative analysis of mixture formation

The hydrogen jet has a relatively high velocity entering the combustion chamber. Note that a gas injection model is used in this study to prevent the modeling of the supersonic jet. Thus, the entrance velocity to the computational domain is subsonic and is diffused rapidly.

A qualitative evaluation of each case can be obtained by assessing the hydrogen mass fraction contours at different injection times. The result is visualized using VTG visualization software. The results from GTT are exported in '.gz' format at regular intervals. The hydrogen mass fraction contours are visualized on different cut planes to analyse the propagation of the fuel from the injector to the engine cylinder. The regions of high fuel content and low fuel content can be identified through the mass fraction contours. In the following sections the mixture formation in each case is analysed qualitatively using hydrogen mass fraction contours. The four different ignition modes injection times such as HI (head Ignition), CI (center ignition), TI (Tail Ignition), and ATI (After Tail Ignition) are used

for the present study. The details of injection time are described in section 4.5.8. The injector location is placed on the center of cylinder head and an angle of injection is set to 45 degree. Figure 6.13 to 6.16 shows the simulation of direct hydrogen injection in terms of mass fraction contour at the specific crank angle (CA) under four different ignition mode timing. The hydrogen mass fraction contours during the injection and at TDC are shown for each ignition mode.

6.9.2.1 HI injection case

The detailed mixture formation process for HI injection mode is shown in Fig. 6.13. The mixing process can be seen from the evolution of the contour of hydrogen mass fraction. In HI mode, fuel injection starts at 5 degree before TDC. The piston is under compression stroke at this crank angle and has reached near TDC. As a result, the chamber pressure during injection is higher. This resulted in a slower penetration of the jet. However, the upward motion of the piston makes the jet to impinge on the piston surface at 356.9 deg. CA. It was also observed that the included angle of fuel jets was reduced as the jet progress through the in-cylinder. After impinging the piston surface, the fuel spreads along the piston towards the cylinder wall. The fuel then moves along the cylinder wall upwards. This phenomenon is clearly observed in Fig 6.17 through the predicted iso-surface of hydrogen mass fraction. The residence time of the fuel inside the cylinder is less and hence the final mixture in this case has rich.

6.9.2.2 CI injection case

Figure 6.14 shows the hydrogen mass contours along the injection plane for CI injection mode. In CI mode, fuel injection starts at 10 degree before TDC. From the side view of fuel mass fraction contours, the angle of fuel jets can be seen. Note that these images are plotted on the cut planes aligned with the gas jet direction. Based on the observation of the present simulation results, the hydrogen jets impinge on the piston surface very quickly due to their high velocities. There is strong influence of vortex generated by piston movement on mixing process. When the piston approaches TDC then the vortex is getting weaker so mixing is less effective. As the cycle progresses, the fuel crawls up along the cylinder wall as show in Fig. 6.18. It can be seen from the contours at TDC that there are regions inside the cylinder with

high fuel content near the piston surface and some regions of low fuel content near by the cylinder wall. The present study did not consider the air intake calculation through the intake valves. The motion of the piston creates swirl and tumble inside the cylinder are chooses as default setting in GTT CFD.

6.9.2.3 TI injection case

The detailed mixture formation process for TI injection mode is shown in Fig. 6.15. In TI mode, fuel injection starts at 20 degree before TDC. The fuel jets impinge on the piston surface at 342.5 deg. CA. After impingement, the fuel spreads along the piston surface towards the cylinder wall as well as CI mode. As the cycle progresses, the fuel crawls up along the cylinder wall. It can be seen from the iso-surface at TDC (see Figure 6.19) that the fuel crawls up along the cylinder wall is similar to the CI mode. There are regions inside the cylinder with high fuel content near the piston surface.

6.9.2.4 ATI injection case

Figure 6.16 shows the hydrogen mass contours along the injection plane for ATI injection case. In CI mode, fuel injection starts at 25.5 degree before TDC and ends at 5 degree before TDC. Similar to the previous case, the fuel jet impinge on the piston surface and after impingement fuel spreads along the piston surface towards the cylinder wall. After the end of inject very few quantity fuel near the wall returns to injector location at TDC timing indicates relative better mixing. Similar trends can observe in Fig. 6.20. There are regions of low fuel content near the cylinder head when piston reached at TDC, which can be seen in the contour image. As we know the ATI ignition mode allowed a 5° CA after the EOI for the injected gas to mix and settle before ignition.

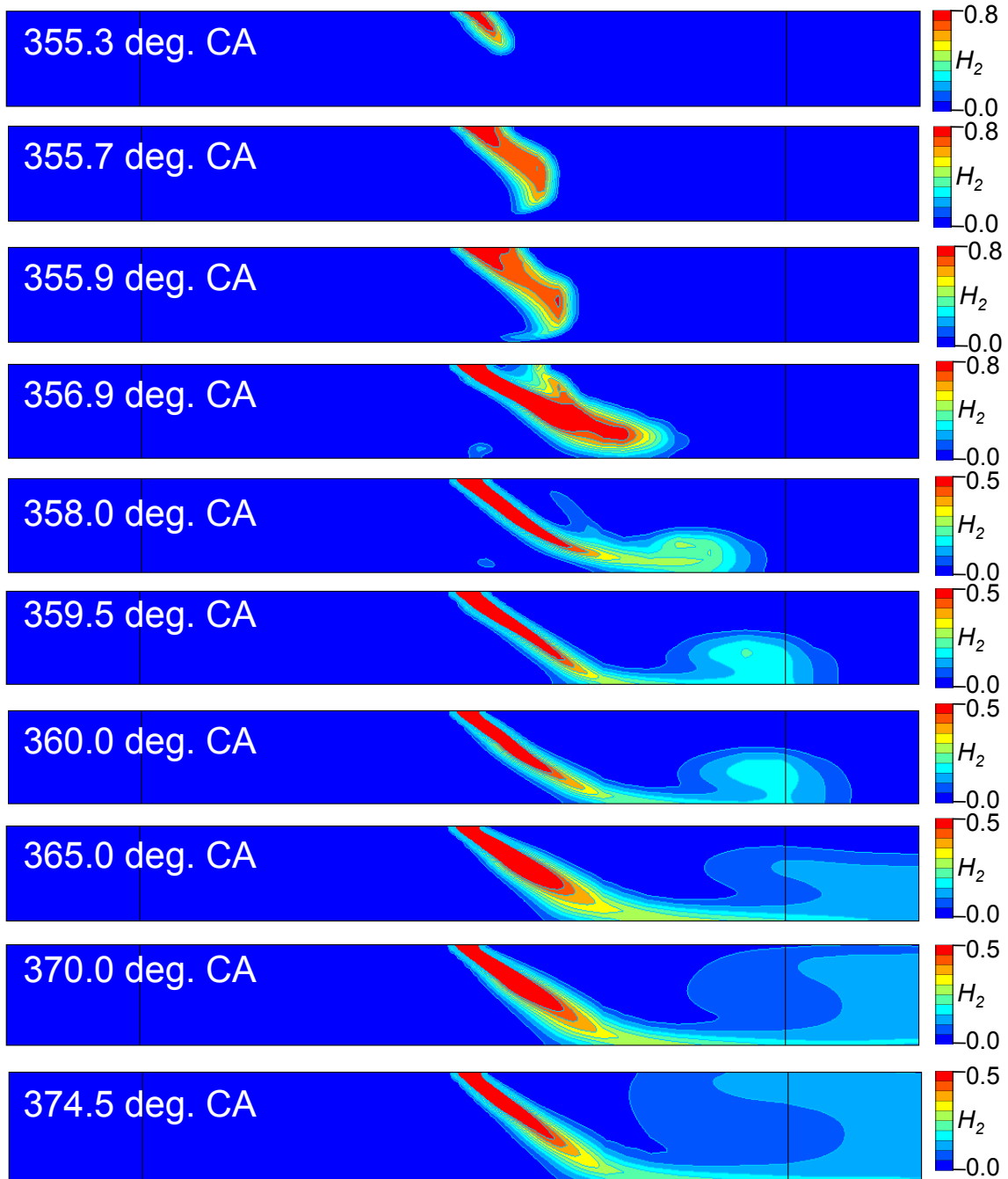


Figure 6.13 Hydrogen mass fraction contours on injection planes during HI timing. Where SOI= 355 deg. CA and EOI =374.5 deg. CA. ($\phi=0.22$, $P_{inj}=5\text{MPa}$, $V_{inj}=200\text{m/s}$)

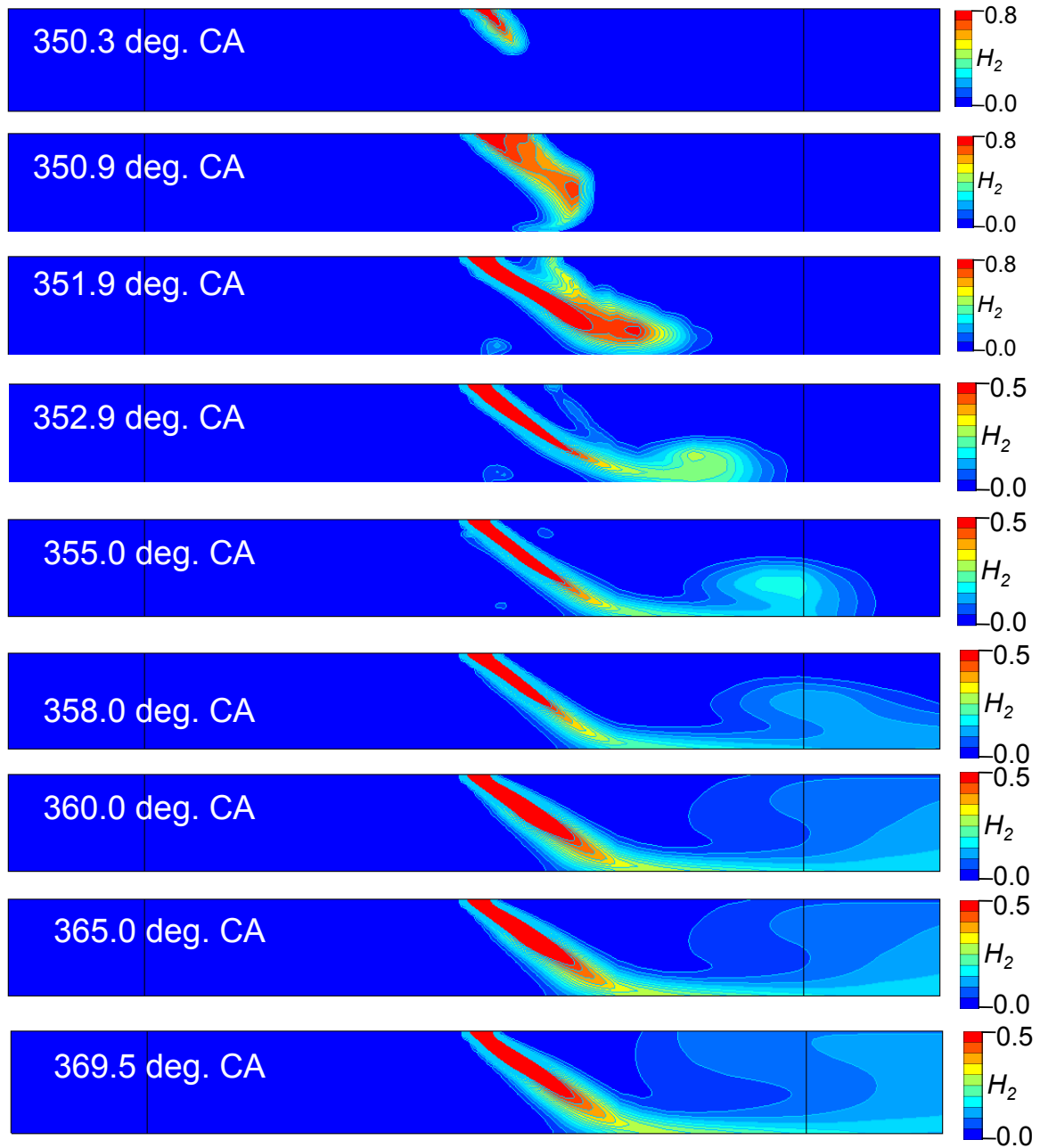


Figure 6.14 Hydrogen mass fraction contours on injection planes during CI timing. Where SOI= 350 deg. CA and EOI =369.5 deg. CA. ($\phi=0.22$, $P_{inj}=5\text{MPa}$, $V_{inj}=200\text{m/s}$)

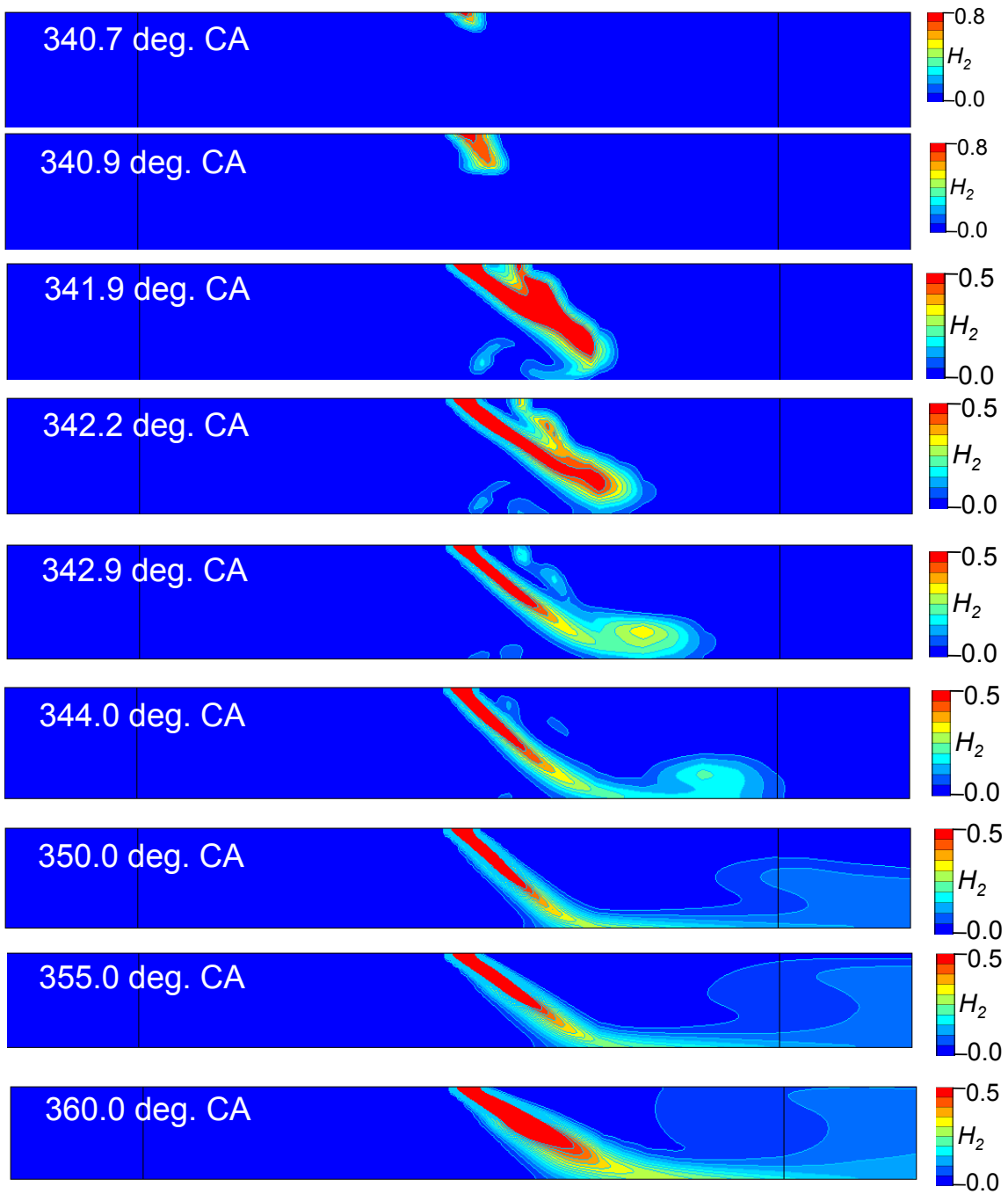


Figure 6.15 Hydrogen mass fraction contours on injection planes during TI timing. Where SOI= 340.5 deg. CA and EOI =TDC. ($\phi=0.22$, $P_{inj}=5\text{MPa}$, $V_{inj}=200\text{m/s}$)

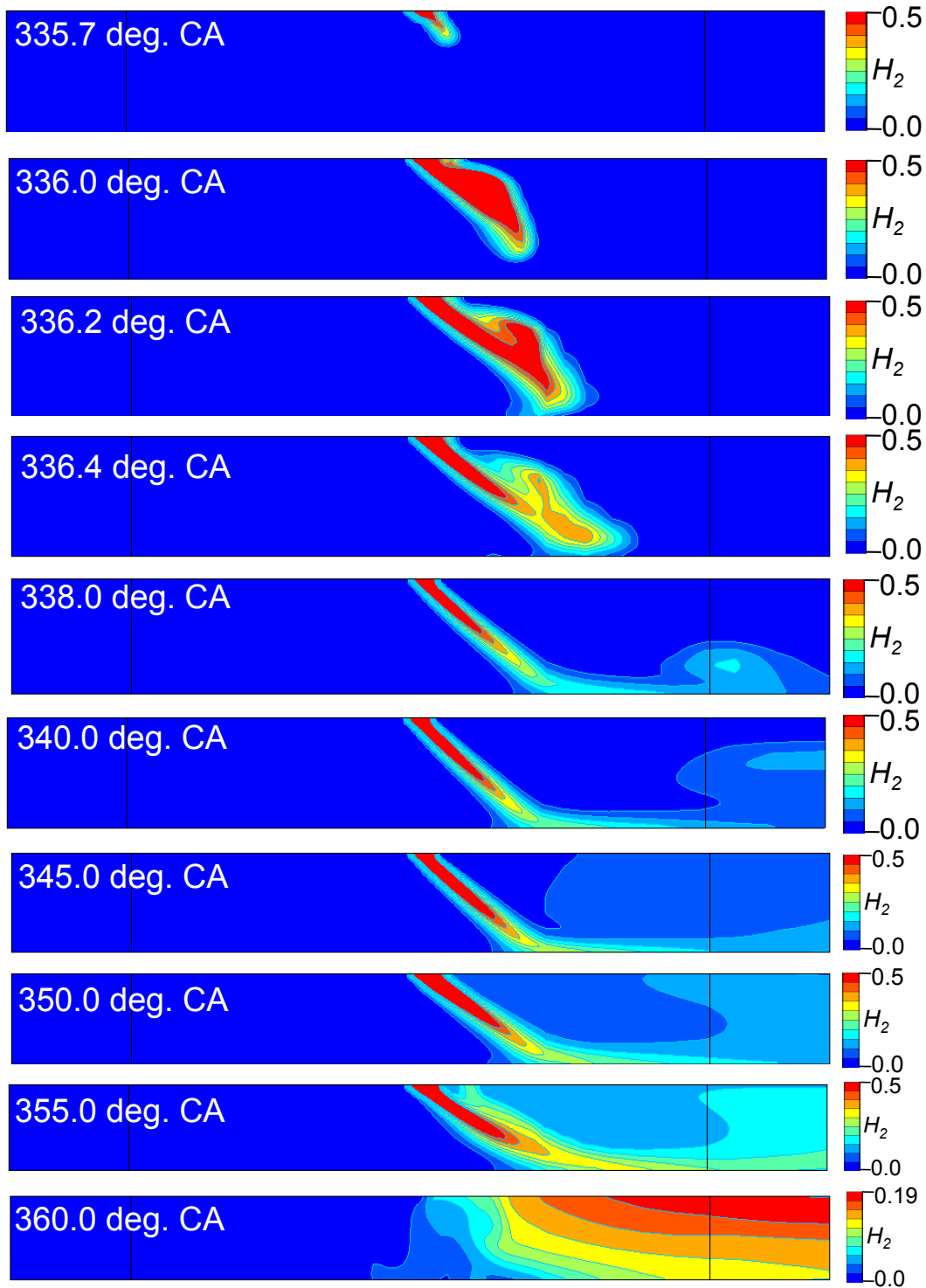


Figure 6.16 Hydrogen mass fraction contours on injection planes during ATI timing. Where SOI= 335.5 deg. CA and EOI =355 deg. CA. ($\phi=0.22$, $P_{inj}=5\text{MPa}$, $V_{inj}=500\text{ m/s}$)

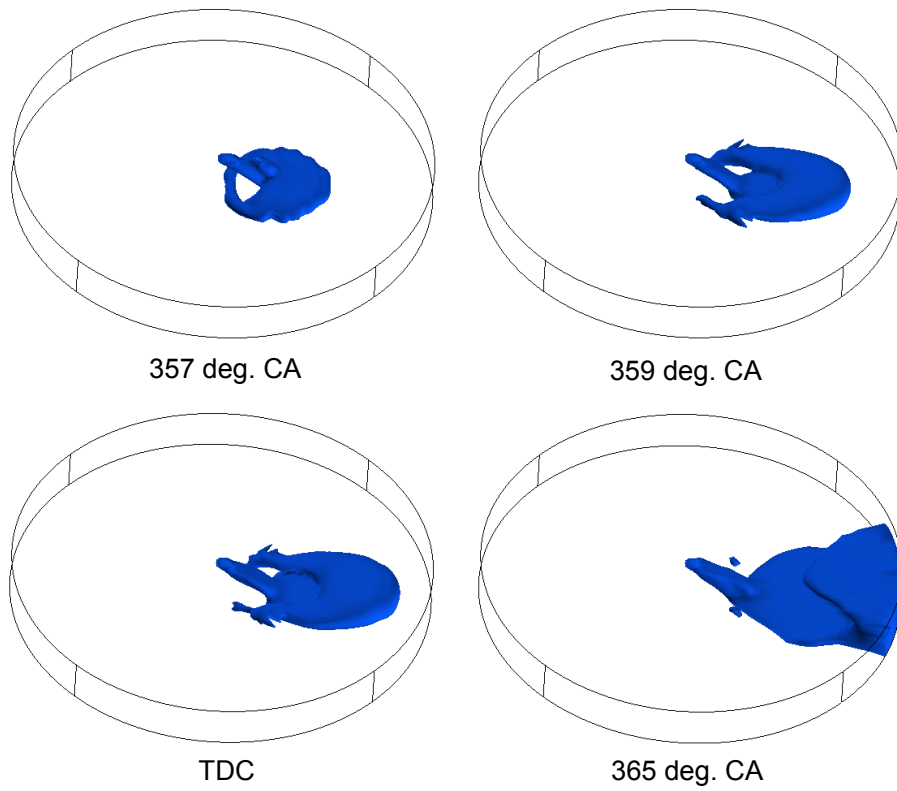


Figure 6.17 Predicted iso-surface of hydrogen mass fraction at HI timing.

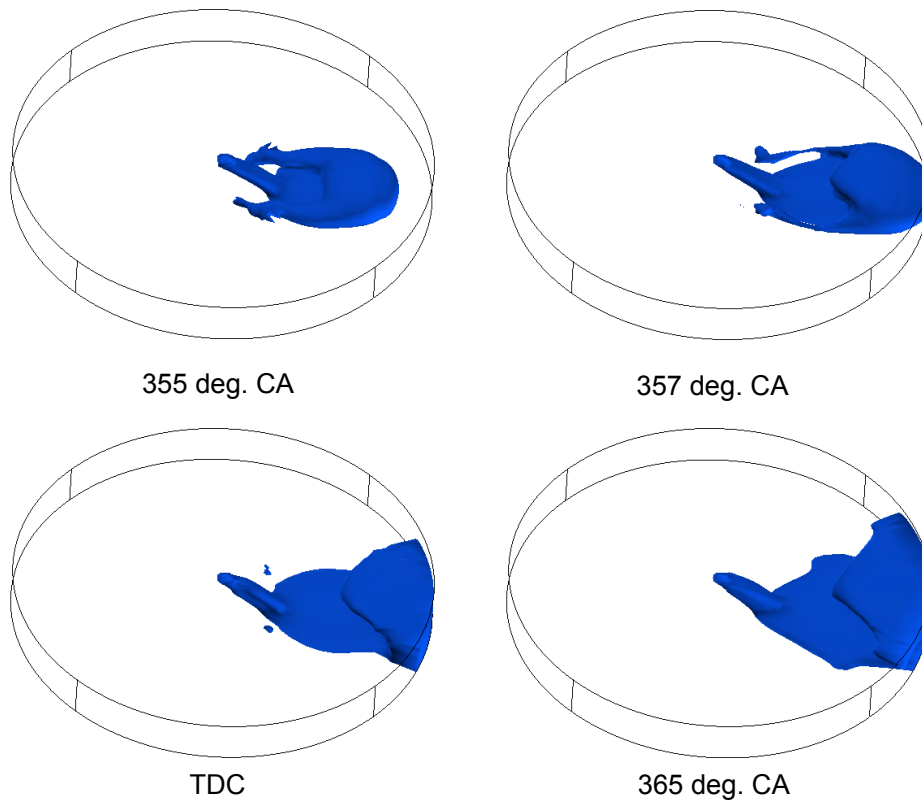


Figure 6.18 Predicted iso-surface of hydrogen mass fraction at CI timing.

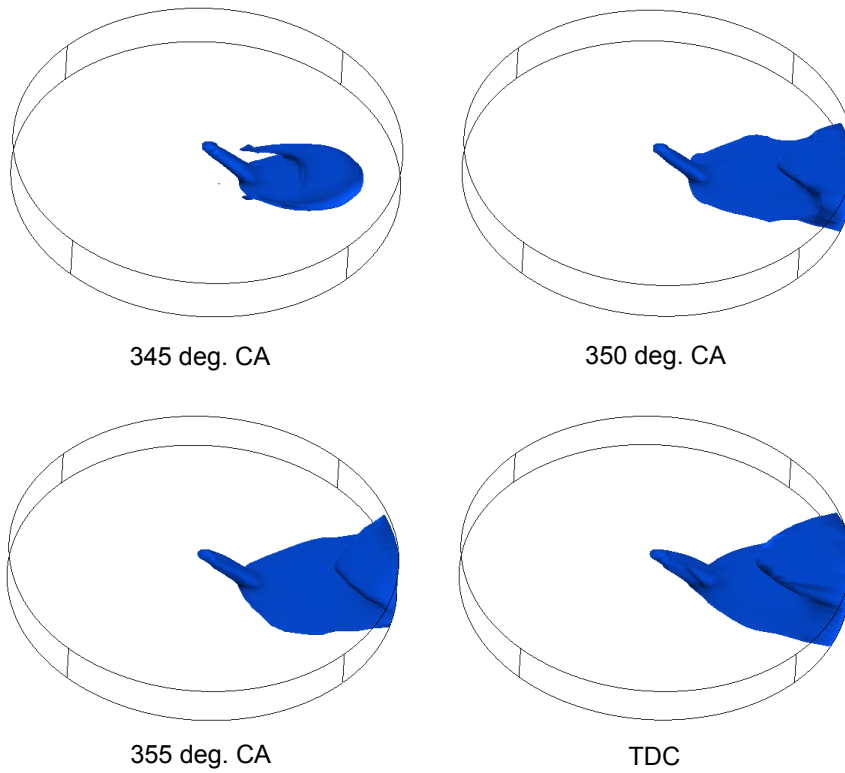


Figure 6.19 Predicted iso-surface of hydrogen mass fraction at TI timing.

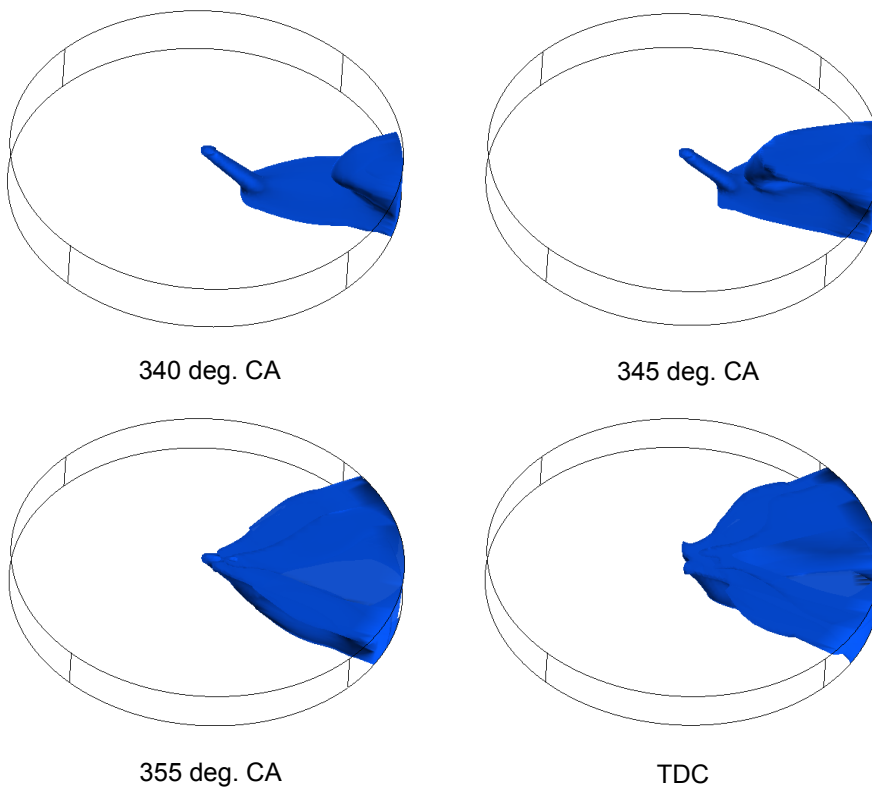


Figure 6.20 Predicted iso-surface of hydrogen mass fraction at ATI timing.

6.9.3 Predicted local equivalence ratio

A parametric study was conducted to analyse the dependence of fuel-air mixing in a hydrogen direct injection engine. In this study Plume Ignition Combustion Concept (PCC) was used, in which with an optimal combination of hydrogen injection timing and ignition timing, the plume tail of the hydrogen jet is spark-ignited upon the completion of fuel injection to accomplish combustion of a rich mixture. The predicted local equivalence ratio contours at TDC position for different ignition mode are shown in Figure 6.21. Our objective is to measure the predicted local equivalence ratio before the combustion initiation at TDC comparing with the experimental local equivalence, which is obtained by SIBS spectra. The engine is in the compression stroke when the fuel is injected. As the SOI is delayed, the volume of air to which the fuel is injected reduces and the residence time of fuel before the start of combustion decreases. The included angle of injection is fixed to 45° . Figure 6.21 shows the fluctuation of the equivalence ratio at the spark location. The high-level equivalence ratio observes in the spray region and the following rapid decrease due to turbulent mixing. It is seen that the mixing is better for the early SOI case. The injected fuel has less time to mix with air in the cylinder as the SOI is retarded. It is observed from the predicted local equivalence ratio that the projected jet centre forms a rich mixture in the vicinity of the spark plug at TDC. When the fuel is injected at SOI =355 deg. CA (HI timing), the initial fuel distribution appears to show a reduction in the jet-spread angle. The jet has penetrated the cylinder and impinged on the piston. Parts of the recirculation vortices from the jet impingement are seen near the jet core. The fuel stays highly concentrated in the piston center. For SOI =350 deg. CA (CI timing), the impinged fuel has rolled over the piston surface and it is moving upwards along the cylinder walls. Due to the presence of the piston higher up in the cylinder and possibly also a larger spreading angle, this fuel has spread to be in the squish zone. Thus very rich fuel reaches the spark plug region. Moreover in CI timing, ignition is occurs in the process of injection, this injection strategy may not be optimal for stably firing engine operation. For SOI =340.5 deg. CA (TI timing) the overall evolution of the jet into a fuel cloud deflected to make round-trip is similar to that CI timing. The impinged fuel has already “rolled over” the piston and cylinder walls. As the fuel cloud moves along the walls it entrains air and becomes leaner. It is well known late cycle breakdown of intake tumble there could also be breakdown of the large vortex induced by the injection. The plane close to spark shows a region rich in fuel. This may enable stably firing

operation of the engine. For ATI timing where $SOI = 335.5$ deg. CA and allowed a 5° CA after the EOI for the injected gas to mix and settle before ignition. Early injection like ATI timing has faster convection. On the other hand late injection yields drastically reduced fuel convection because of shorter aspect ratio of the remaining volume, the increased in-cylinder pressure and the reduction in available time.

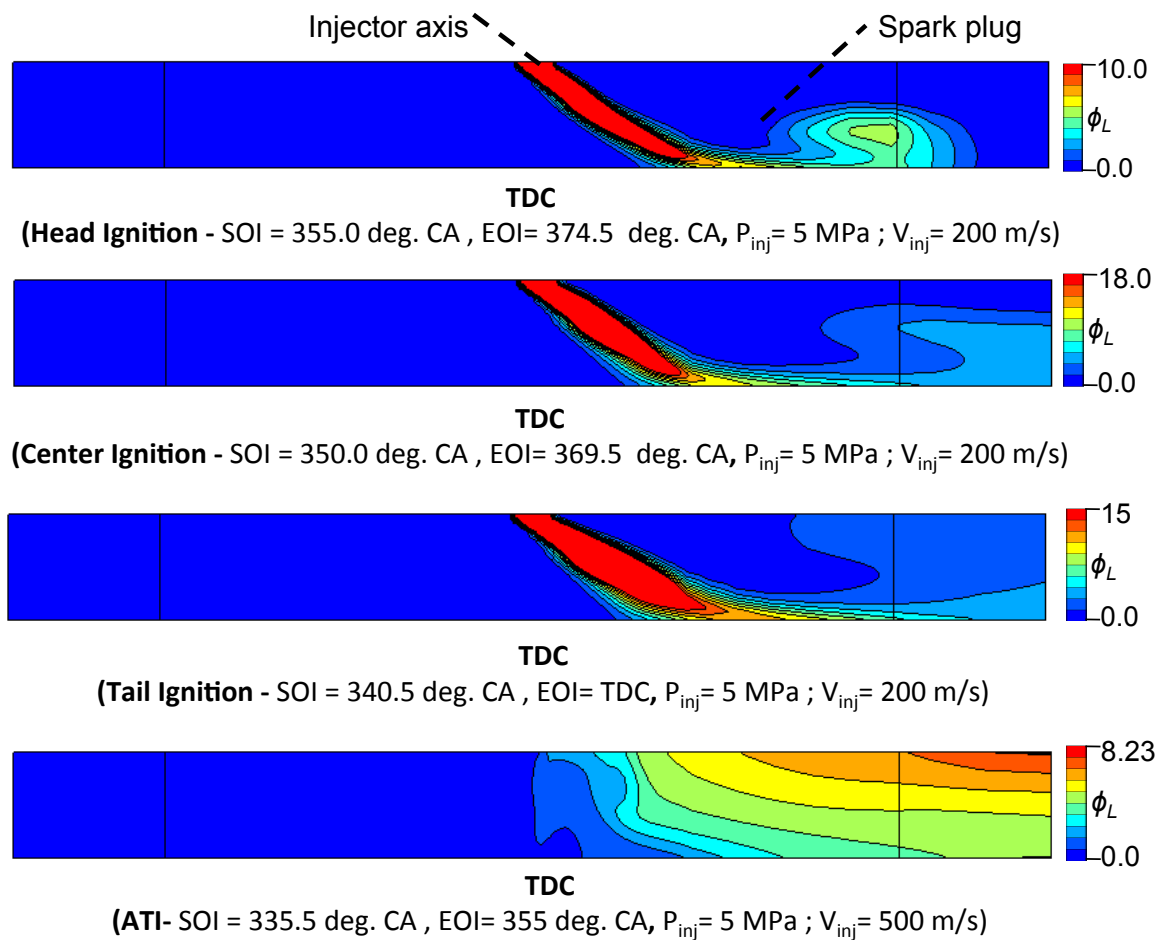


Figure 6.21 Predicted local equivalence ratio at different ignition modes combustion using GTT.

6.10 Summary

The model was validated by comparing the predicted hydrogen penetrations with experimental and theoretical data. Hydrogen jet is injected into a nitrogen ambient which was simulated using gas parcel method in GTT-CHEM. Good levels of agreement between numerical and experimental results are obtained for single jet. A parametric study was also conducted to explore the mixture formation characteristics inside the engine cylinder at various injection timings. This study follows a RANS approach combined with $k-\epsilon$ model to describe in-cylinder turbulence. There is strong influence of vortex generated by piston movement on mixing process. In engine simulation, inclined hydrogen jet impinges on the flat piston surface in a short delay, and that the fuel jet forms a cloud that develops horizontally along this surface. After the impact, the rich pocket lying near the piston surface is convected by the tumbling flow, towards the cylinder head. In the TI condition, the rich zone moves rather slowly from the piston surface, so that favourable conditions are obtained at the spark location and timing.

7 Conclusions

For stratified charge operation the combustion characteristics of the hydrogen jets were studied in a compression–expansion engine running at 600 rpm. A high-speed video camera was used to capture images of jet-guided combustion relative to ignition timing. The effects of injection pressure and fuel injection timing were studied under different equivalence ratios. Moreover a high-speed video camera was used to image hydrogen jet development at the nozzle exit in a constant volume chamber. The effects of fuel injection pressure and ambient density on the jet overall characteristic at nozzle tip were studied. The following conclusions were drawn from this experiment:

1. Argon (Ar)-ion laser beam was used as a light source to visualize the hydrogen jet development at the nozzle exit in a constant-volume chamber. This allowed us to study the structure of the jet in addition to other physical processes resulting from hydrogen gas injection. The penetration depth and jet cone angle are important factors. The experimental results showed that the jet penetration rate increased with increasing injection pressure, and decreased with increasing ambient pressure. Moreover, the effect of injection pressure at 3 MPa resulted in larger initial jet angle than the injection pressure of 5 MPa. Varying the ambient density from 1.15 to 16.83 kg/m³ changed the structure of the fuel jet. Direct visualization of hydrogen jet gives the useful information where the jet tip pushes out the still ambient nitrogen, and then the vortex structure is formed by the interaction between the jet and the ambient nitrogen. Gas injection at high pressure can increase the momentum injected into the cylinder, the mixture turbulence level, and the overall amount of fuel-air mixture.
2. The combustion characteristics of the hydrogen jets can be controlled by varying the fuel injection timing. The Tail Ignition (TI) mode, whereby injection is terminated at the instant of the spark ignition, resulted in sufficient hydrogen being present in vicinity of the spark plug to create an ignitable mixture at the EOI. TI mode combustion had faster burning rate compared to the other ignition modes and thereby increases the combustion efficiency.

3. For CI, in-cylinder combustion pressure was lower compared to TI and ATI. The ROHR for CI was faster in the initial stage, but slower burn in the later stages, indicating diffusive phase combustion. For HI mode, ignition timing at the early stage of SOI, resulting in reducing the in-cylinder pressure with a low burning rate.
4. Pictures of the initial combustion phase indicate an initial quasi-spherical and later partially wrinkled flame. The flame intensity was stronger with the increased of equivalence ratio, means a higher degree of mixture stratification occurred near the spark electrode gap at ignition. Moreover, the high flame intensity induced by a high gas temperature during the combustion process, which was expected since the amount of fuel increases with the overall equivalence ratio.
5. The COV of IMEP for the four ignition modes were measured in this experiment, Tail Ignition (TI) mode showed relatively stable combustion compared to other ignition modes. This engine has only one intake valve. The in-cylinder exhaust gas was drawn out by a vacuum pump through the inlet valve. There is no influence in the present study from the residual gas and charging that play the influence on the cyclic variations in a real direct-injection engine. The experimental conditions such as the temperature and pressure are also much lower than those of a real engine. Thus, the cyclic variations in the engine study only reflect the mixture formation, both local equivalence ratio and degree of mixture stratification and/or mixture inhomogeneity besides the influence from gas flow.
6. The local equivalence ratio at stratified charge combustion condition was measured using spark-induced breakdown spectroscopy (SIBS) with a fiber-coupled CCD spectrometer. A fiber-optic spark plug sensor was developed for application to practical DISI engine. The atomic emission intensities $H\alpha$, and $O(I)$ produced during spark discharge were correlated to the global equivalence ratio. For stratified charge operation of the jet injection relative to ignition timing, the estimated local equivalence ratio at the spark gap just after spark breakdown was very rich and varies widely from cycle-to-cycle. The results presented here confirm the usefulness of spark-induced breakdown spectroscopy as a diagnostic

tool for spark-ignition engine. Optimization of the UV-grade optical fiber and the optical gate period in CCD camera should be carried for further measurement.

7. The model was validated by comparing the predicted hydrogen penetrations with experimental and theoretical data. Hydrogen jet is injected into a nitrogen ambient which was simulated using gas parcel method in GTT-CHEM. Good levels of agreement between numerical and experimental results are obtained for single jet. A parametric study was also conducted to explore the mixture formation characteristics inside the engine cylinder at various injection timings. This study follows a RANS approach combined with k- ϵ model to describe in-cylinder turbulence. There is strong influence of vortex generated by piston movement on mixing process. In engine simulation, inclined hydrogen jet impinges on the flat piston surface in a short delay, and that the fuel jet forms a cloud that develops horizontally along this surface. After the impact, the rich pocket lying near the piston surface is convected by the tumbling flow, towards the cylinder head. In the TI condition, the rich zone moves rather slowly from the piston surface, so that favourable conditions are obtained at the spark location and timing.

8 References

- [1] C.J. Winter, “Hydrogen energy- Expected Engineering Breakthroughs”, *International Journal of Hydrogen Energy* 12(8), 1987, pp. 521-546
- [2] R.M. Zweig, “The hydrogen economy: Phase 1”, *Proceedings of the Ninth World Hydrogen Energy Conference. Volume 3*, pp.1995- 2002
- [3] G.A. Karim, “Hydrogen as a spark ignition engine fuel”, *International Journal of Hydrogen Energy*, 28 (2003); pp. 569-577.
- [4] G.A. Karim, S.R. Klat, “Hydrogen as a fuel in compression ignition engines”, *Journal of Mechanical Engineering ASME* 98(1976); pp. 34-39.
- [5] C.M. White, R.R Steeper, A.E. Lutz, “The hydrogen fueled internal combustion engine: a technical review”, *International Journal of Hydrogen Energy*, 31 (2006); pp. 1292-1305.
- [6] J. Romm, “The car and fuel of the future”, *Energy Policy*, 34 (2006); pp. 2609–2614
- [7] H. Eichlseder, T. Wallner, R. Freymann, J. Ringler, “The Potential of Hydrogen Internal Combustion Engines in a Future Mobility Scenario”, *SAE paper 2003-01- 2267*
- [8] A. Mohammadi, M. Shioji, Y. Nakai, W. Ishikura, E. Tabo, *International Journal of Hydrogen Energy*, 32 (2007), pp. 296-304.
- [9] A. Wimmer, T. Wallner, J. Ringler and F. Gerbig, *SAE paper 2005-01-0108*.
- [10] L.M. Das, R. Gulati, P.K. Gupta, “A comparative evaluation of the performance characteristics of a spark ignition engine using hydrogen and compressed natural gas as alternative fuels”, *International Journal of Hydrogen Energy*, 25 (2000); pp. 783-793.
- [11] L.M. Das, “Hydrogen engine: research and development (R&D) programmes in Indian Institute of Technology (IIT) Delhi”, *International Journal of Hydrogen Energy*, 27 (2002); pp. 953– 965.
- [12] H. Li, G.A. Karim, “Knock in spark ignition hydrogen engines”, *International Journal of Hydrogen Energy*, 29 (2004); pp. 859–865
- [13] T. Wallner, A.M. Nande, J. Naber, “Evaluation of injector location and nozzle design in a direct-injection hydrogen research engine”, *SAE Paper 2008-01- 1785*
- [14] M. Oikawa, Y. Ogasawara, Y. Kondo, K. Sekine, K. Naganuma, Y. Takagi, Y. Sato, “Optimization of Hydrogen Jet Configuration by Single Hole Nozzle and High Speed Laser Shadowgraphy in High Pressure Direct Injection Hydrogen Engines”, *SAE paper 2011-01-2002*.

- [15] S. Verhelst, T. Wallner, "Hydrogen-Fueled Internal Combustion Engines", *Progress in Energy and Combustion Science*, 35 (2009), pp. 490-527.
- [16] C.M. White, "OH* chemiluminescence measurements in a direct injection hydrogen-fuelled internal combustion engine", *International Journal of Engine Research*, Vol. 8, Part 2, (2007); pp. 185-204.
- [17] B.R. Peterson, J.B. Gandhi, "Transient high-pressure hydrogen jet measurements", SAE paper 2006-01-0652.
- [18] J. B. Heywood, F. R. Vilchis, "Comparison of Flame Development in a Spark-Ignition Engine Fueled with Propane and Hydrogen". *Combustion Science and Technology* Vol. 38 (1984), pp 313-324.
- [19] F.P. Ricou, D.B. Spalding, "Measurement of entrainment by axisymmetrical turbulent jets", *Journal of Fluid Mechanics*, Vol. 11, (1961); pp. 21-32.
- [20] G. N. Abramovich, "The Theory of Turbulent Jets", M.I.T. Press, Massachusetts, (1963).
- [21] P. O. Witze, "The impulsively started incompressible turbulent jet," Sandia Laboratories Report, SAND80-8617.
- [22] N. Rajaratnam, "Turbulent Jets", Elsevier Scientific Publishing Company, Amsterdam, (1976)
- [23] J. Panda, R.G. Seasholts, "Measurement of shock structure and shock-vortex interaction in underexpanded jets using Rayleigh scattering", *Physics of Fluids*, Vol. 11, No. 12, (1999); pp. 3761-3777.
- [24] P. S. Cumber, M. Fairweather, S. A. E. G Falle, J.R. Giddings, "Predictions of the structure of turbulent highly underexpanded jets", *Journal of Fluids Engineering*, 117, (1995); pp. 599-604.
- [25] D. A. Anderson, J.C. Tannehill, R.H. Pletcher, "Computational Fluid Mechanics and Heat Transfer", (1985), McGraw-Hill.
- [26] G. N. Abramovich, "The Theory of Turbulent Jets", (1963), MIT press
- [27] J. O. Hinze, "Turbulence", 2nd Ed., (1975), McGraw-Hill
- [28] J. S. Turner, "The starting plume in neutral surroundings", *Journal of Fluid Mechanics*, Volume 13, (1962); pp.356-368.
- [29] T. W. Kuo, and F. V. Bracco, "On the Scaling of Transient Laminar, Turbulent and Spray Jets", SAE Paper 820038

- [30] M. Van Dyke, "An Album of Fluid Motion", Parabolic Press, Stanford, California, 1988
- [31] G.K. Batchelor, "An Introduction to Fluid Dynamics", Cambridge Press, 1967
- [32] S. Abramovich, A. Solan, "The initial development of a submerged laminar round jet", *Journal of Fluid Mechanics*, Volume 59, (1973); pp. 791-801
- [33] H. Sato, F. Sakao, An experimental investigation of the instability of a two-dimensional jet at low Reynolds numbers, *Journal of Fluid Mechanics*, Volume 20, (1964); pp. 337-352
- [34] M. Miyake, T. Biwa, Y. Endoh, M. Shimotsu, S. Murakami, T. Komoda, "The Development of High-Output, Highly Efficient Gas Burning Diesel Engines", CIMAC Paper D11.2, 1983
- [35] J.B. Heywood, "Internal Combustion Engine Fundamentals", McGraw-Hill Book Company, 1988
- [36] F. Zhao, M.C. Lai, D. L. Harrington, "Automotive Spark Ignited Direct-Injection Gasoline Engines," *Progress in Energy and Combustion Science*, Vol. 25 (1999), No. 5, pp. 437-562
- [37] U. Spicher, A. Kölmel, H. Kubach and G. Töpfer, "Combustion in Spark Ignition Engines with Direct Injection", SAE Paper 2000-01-0649.
- [38] S. Stefan, "Optical Diagnostics on FSI Transparent Engine", FISITA World Automotive Congress, Barcelona 23-27 May, Barcelona Spain, 2004.
- [39] R. Ortmann, S. Arndt, J. Raimann, R. Grzeszik and G. Würfel, "Methods and Analysis of Fuel Injection, Mixture Preparation and Charge Stratification in Different Direct Injected SI Engines", SAE Paper 2001-01-0970.
- [40] L. M. Das, "Hydrogen engines: a view of the past and a look into the future," *International Journal of Hydrogen Energy*, Vol. 15, No. 6(1990), pp. 425-443
- [41] X. Tang, D. M. Kabat, R. J. Natkin, W. F. Stockhausen, and J. Heffel, "Ford P2000 Hydrogen Engine Dynamometer Development", SAE Paper 2002-01-0242
- [42] C. A. MacCarley, "A study of factors influencing thermally induced backfiring in hydrogen fuelled engines, and methods for backfire control", 16th IECEC conference, Atlanta, USA, 1981
- [43] T. Kondo, S. Iio, M. Hiruma, "A study on the mechanism of backfire in external mixture formation hydrogen engines—about backfire occurred by the cause of the spark plug", SAE paper 971704

- [44] M. R. Swain, G.J. Schade , M.N. Swain, “Design and testing of a dedicated hydrogen-fueled engine”, SAE paper 961077
- [45] K. Koyanagi, M. Hiruma, and S. Furuhashi, “Study on mechanism of backfire in hydrogen engines”, SAE paper 942035
- [46] S. J. Lee, H. S. Yi and E.S. Kim, “Combustion characteristics of intake port injection type hydrogen fueled engine”, International Journal of Hydrogen Energy, Volume 20, 1995, pp. 317–322
- [47] M. Swain, M. Swain and R. Adt, “Consideration in the design of an inexpensive hydrogen-fueled engine”, SAE paper 881630
- [48] H. Li and G. A Karim, “Hydrogen fuelled spark ignition engines: predictive and experimental performance”, ASME Spring Technical Conference, Paper number ICES2003-548, Salzburg, Austria, 2003.
- [49] W. F. Stockhausen, R. J. Natkin, D. M. Kabat, L. Reams, X. Tang, S. Hashemi, S. J. Szwabowski, V. P. Zanardelli, “Ford P2000 hydrogen engine design and vehicle development program”, SAE Paper 2002-01-0240
- [50] B. LEWIS & G. VONELBE, “Combustion, Flames and Explosions of Gases”, 2nd Edition, Academic Press, New York
- [51] R. Sierens, S. Verhelst, “Experimental study of a hydrogen-fueled engine”, Journal of Engineering for Gas Turbines and Power, ASME, 123(2001), pp. 211-216
- [52] Y. Y. Kim, J. T. Lee and J. A. Caton, “The development of a dual-Injection hydrogen-fueled engine with high power and high efficiency”, Journal of Engineering for Gas Turbines and Power, ASME. 128(2006), pp. 203-212.
- [53] M. Berckmuller, H. Rottengruber, A. Eder, N. Brehm, G. Elsasser, G. Muller- Alander and C. Schwarz, “Potentials of a charged SI-hydrogen engine,” SAE Paper 2003-01-3210
- [54] S. Verhelst, R. Sierens and S. Verstraeten, “A Critical Review of Experimental Research on Hydrogen Fueled SI Engines”, SAE Paper No. 2006-01-0430
- [55] T. Wallner, A. Nande and J. Naber, “Study of Basic Injection Configurations Using a Direct-Injection Hydrogen Research Engine”, SAE Paper 2009-01-1418
- [56] E. Tomita, Y. Hamamoto, S. Yoshiyama, H. Toda, “Measurement of fuel concentration distribution of transient hydrogen jet and its flame using planar laser induced fluorescence method”, JSAE Review, 19 (1998), pp.329-335.
- [57] S. Kaiser, C. M. White, “PIV and PLIF to Evaluate Mixture Formation in a Direct-Injection Hydrogen-Fuelled Engine”, SAE paper 2008-01-1034.

- [58] T. Blotevogel, M. Hartmann, H. Rottengruber, A. Leipertz, "Tracer-based laser-induced fluorescence measurement technique for quantitative fuel/air-ratio measurements in a hydrogen internal combustion engine", *Applied Optics*, Volume 47 (2008), pp. 6488-6496.
- [59] F. Ferioli, P. V. Puzinauskas, S.G. Buckley, "Laser-Induced Breakdown Spectroscopy for On-Line Engine Equivalence Ratio Measurements", *Applied Spectroscopy*, Volume 57(2003), pp. 1183-1189.
- [60] T. X. Phuoc, "Laser-induced spark for simultaneous ignition and fuel-to-air ratio measurements", *Optics and Lasers in Engineering*, Volume 44 (2006), pp. 520-534.
- [61] T. Shudo, S. Oba, "Mixture distribution measurement using laser induced breakdown spectroscopy in hydrogen direct injection stratified charge", *International Journal of Hydrogen Energy*, 34 (2009), pp. 2488-2493.
- [62] N. Kawahara, E. Tomita, S. Takemoto, Y. Ikeda, "Fuel concentration measurement of premixed mixture using spark-induced breakdown spectroscopy", *Spectrochimica Acta Part B: Atomic Spectroscopy*, Volume 64 (2009), pp. 1085-1092.
- [63] K. Kuwahara, H. Ando, "Diagnostics of in-cylinder flow, mixing and combustion in gasoline engines", *Measurement Science and Technology*, 11 (2000) R95.
- [64] T. D. Fansler, B. Stojkovic, M. C. Drake, M.E. Rosalik, "Local fuel concentration measurements in internal combustion engines using spark-emission spectroscopy", *Applied Physics B: Lasers and Optics*, 75 (2002), pp. 577-590
- [65] R. M. Merer, J. S. Wallace, "Spark spectroscopy for spark ignition engine diagnostics," SAE 950164
- [66] M. Stano, S. Matejcik, J.D. Skalny, T. D. Mark, "Electron impact ionization of CH₄: ionization energies and temperature effects", *Journal of physics B: Atomic, Molecular and Optical Physics*, volume 36, (2003), pp. 261-271
- [67] T. D. Fansler, B. Stojkovic, M. C. Drake, & M. E. Rosalik, "Local fuel concentration measurements in internal combustion engines using spark-emission spectroscopy", *Applied Physics B*, pp. 577-590
- [68] F. A. Soldera, F. T. Mucklich, K. Hrastnik, T. Kaiser, "Description of the Discharge Process in Spark Plugs and its Correlation with Electrode Erosion Patterns", *IEEE Transactions on Vehicular Technology*, Vol. 53, No. 4, pp. 1257-1265

- [69] R. Maly, "Spark Ignition: Its Physics and Effects on the Internal Combustion Engine in Fuel Economy: Road Vehicles Powered by Spark Ignition Engines", Eds. J.C. Hilliard and G.S. Springer, Plenum, New York, 1984.
- [70] N. St. J. Brathwaite, "Introduction to gas discharge", Plasma sources science and technology, vol. 9, pp. 517-527
- [71] A. A. Kulikovshy, "Positive streamer between parallel plate electrodes in atmospheric pressure air", Journal of physics D: Applied physics, vol. 30, pp. 441-450
- [72] G. V. Naidis, "Simulation of streamer-to-spark transition in short non-uniform air gaps", Journal of physics D: Applied physics, vol. 32, pp. 2649-2654.
- [73] H. S. Uhm, "Properties of plasmas generated by electrical breakdown in flames", Physics of plasmas, vol. 6, no. 11. pp. 4366-4374.
- [74] W. D. Greason, Z. Kucеровsky, S. Bulach, W. Flatley, "Investigation of the optical and electrical characteristics of a spark gap." IEEE transactions on industry applications, vol. 33, no. 6, pp. 1519-1526.
- [75] A. Loeb, M. Loebenstein, A. Ludmirsky, S. Eliezer, S. Maman, Y. Gazit, "Point explosion simulation by fast spark discharges." Journal of applied physics, vol. 57, no. 7, pp. 2501-2506.
- [76] Y. P. Raizer, "Gas discharge physics. 2nd edition", Springer-Verlag, Germany. (1997).
- [77] W. T. Ashurst, "Turbulent Flame Motion in a Pancake Chamber via a Lagrangian, Two-Dimensional Vortex Dynamics Simulation", Combustion Science and Technology, 109(1-6), pp. 227-253
- [78] D. L. Reuss, T.W. Kuo, G. Silvas, V. Natarajan and V. Sick, "Experimental metrics for identifying origins of combustion variability during spark-assisted compression ignition", International Journal of Engine Research, Vol. 9 (2008) pp. 409-434.
- [79] J. Abraham and F. V. Bracco, "Comparisons of Computed and Measured Premixed Charge Engine Combustion", Combustion and Flame, Vol. 60 (1985), pp. 309-322.
- [80] R. Maly, M. Vogel, "Initiation and propagation of flame fronts in lean CH₄-air mixtures by the three modes of the ignition spark", Symposium (International) on Combustion, Volume 17(1), 1979, pp. 821-831
- [81] M. K. Roy, N. Kawahara, E. Tomita, T. Fujitani, "High-Pressure Hydrogen Jet and Combustion Characteristics in a Direct-Injection Hydrogen Engine", SAE International Journal of Fuels and Lubricants. 5(3): pp. 1414-1425

- [82] A. J. Yule, S. L. Mo, S. Y. Than, S. M. Aval, “ Diesel Spray Structure”, 3rd Int. Conf. on liquid atomization and spray system, London, ICLASS, 1985.
- [83] D. L. Siebers, “Recent Development on Diesel Fuel Jets under Quiescent Conditions.” Flow and Combustion in Reciprocating Engines, Springer-Verlag Berlin Heidelberg 2009, pp 257-308.
- [84] J. Fiene, T. Braithwaite, R. Boehm, Y. Baghzouz, “Development of a hydrogen engine for a hybrid electric bus”, SAE paper 2002-01-1085
- [85] M. Berckmüller, H. Rottengruber, A. Eder, N. Brehm, G. Elsässer, G. Müller-Alander, “Potentials of a charged SI-hydrogen engine”, SAE paper 2003
- [86] T. Kondo, S. Lio, M. Hiruma, “A study on the mechanism of backfire in external mixture formation hydrogen engines—about backfire occurred by cause of the spark plug”, SAE paper 971704
- [87] S. Furuhashi, K. Yamane, I. Yamaguchi, “Combustion improvement in a hydrogen fueled engine”, International Journal of Hydrogen Energy, Volume 2 (1977); pp.329–340.
- [88] H. S. Homan, P.C.T. DE Boer, W.J. McLean, “The effect of fuel injection on NOx emissions and undesirable combustion for hydrogen-fuelled piston engines”, International Journal of Hydrogen Energy, Volume 8 (1983) , pp. 131–146.
- [89] P. G. Hill, D. Zhang, “The effects of swirl and tumble on combustion in spark-ignition engines”, Progress in energy and combustion science, vol. 20, 1994, pp. 373-429
- [90] R. J. Tabaczynski, “Turbulence and turbulent combustion in spark-ignition engines”, Progress in energy and combustion science, vol. 2, 1976, pp. 143-165
- [91] P. A. Williams, M. H. Davy, D. D. Brehob, “Effects of injection timing on the exhaust emissions of a centrally injected four-valve direct injection spark-ignition engine”, SAE paper 982700.
- [92] T. Alger, M. Hall, R. Matthews, “Fuel spray dynamics and fuel vapour concentration near the spark plug in a direct-injected 4-valves SI engine”, SAE paper 1999-01-0497
- [93] S. Furuhashi, M. Hiruma, Y. Enomoto, “Development of a liquid hydrogen car”, International Journal of Hydrogen Energy, Volume 3, 1978, pp. 61–81.
- [94] H. Knorr, W. Held, W. Prümm, H. Rüdiger, “The MAN hydrogen propulsion system for city buses”, International Journal of Hydrogen Energy, Volume 23 (1997), pp. 201–208.
- [95] N. Kawahara, E. Tomita, “Visualization of auto-ignition and pressure wave during knocking in a hydrogen spark-ignition engine”, International Journal of Hydrogen Energy, 34 (2009), pp. 3156-3163

- [96] S. Verhelst, C.G.W. Sheppard, "Multi-zone thermodynamic modelling of spark-ignition engine combustion: an overview", *Energy Conversion and Management*, Volume 50 (2009), pp. 1326-1335.
- [97] D. A. Shirley, "High-Resolution X-Ray Photoemission Spectrum of the Valence Bands of Gold", *Physical Review B*, Volume 5(1972), pp. 4709-4714.
- [98] B. Lewis, G. von Elbe, "Combustion, flames, and explosion of gases", Orlando, FL: Academic Press (1987).
- [99] C. Fajardo, V. Sick, "Flow Field Assessment in a Fired Spray-Guided Spark-Ignition Direct-Injection Engine Based on UV Particle Image Velocimetry with Sub Crank Angle Resolution", *Proceedings of the Combustion Institute*, Volume 31 (2007), pp. 3023-3031
- [100] S. K. Kim, K. Ito, D. Yoshihara and T. Wakisaka, "Application of a Genetic Algorithm to the Optimization of Rate Constants in Chemical Kinetic Models for Combustion Simulation of HCCI Engines", *JSME International Journal, Ser.B, Vol.48, No.4*, pp.717-724
- [101] S. K. Kim, Y. Takada and T. Wakisaka, "Effects of Mixture Inhomogeneity and Gas Flow on Combustion in Premixed-charge Compression Ignition Engines—Three-dimensional Numerical Analysis of Combustion Process in Consideration of Chemical Kinetics", *Journal of the JIME*, Vol. 42, No.4, pp.125-132
- [102] T. Wakisaka, N. Kato, T.T. Nguyen, K. Okude, S. Takeuchi, and Y. Isshiki, "Numerical Prediction of Mixture Formation and Combustion Processes in Premixed Compression Ignition Engines", *Proceedings of COMODIA 2001*, pp.426-433
- [103] R. J. Kee, "CHEMKIN-II", Sandia Report, SAND89-8009B, (1989).
- [104] A. A. Amsden et al. , "KIVA", Los Alamos National Laboratory Report , LA-10245-MS, 1985.
- [105] N.L. Johnson, A.A. Amsden, J.D. Naber and D.L. Siebers, "Three-Dimensional Computer Modeling of Hydrogen Injection and Combustion," Los Alamos National Laboratory Report LA-UR-95-210, 1995.
- [106] D. A. Mather, and R. D. Reitz, "Modeling the Effects of Auxiliary Gas Injection on Diesel Engine Combustion and Emissions", *SAE Journal of Fuels & Lubricants*, Vol. 109, Section 4, pp. 443-458
- [107] P. Ouellette, P. G. Hill, "Turbulent Transient Gas Injections", *ASME Journal of Fluids Engineering*, Vol. 122, pp. 743-753.

- [108] J. Abraham “Entrainment Characteristics of Transient Gas Jets”, Numerical Heat Transfer, Part A, Vol. 30, pp. 347-364
- [109] J. Abraham, “What is Adequate Resolution in the Numerical Computations of Transient Jets?”, SAE Paper 970051
- [110] R. P. Hessel, S. M. Aceves, D. L. Flowers, “Gaseous Fuel Injection Modeling using a Gaseous Sphere Injection Methodology”, International Multidimensional Engine Modeling User's Group Meeting, Detroit, MI, United States , April 2, 2006 through April 6, 2006
- [111] T. W. Kuo, F. V. Bracco, “On the Scaling of Transient Laminar, Turbulent, and Spray Jets”, SAE Paper 820038.
- [112] H. Fujimoto, Y. Takada and T. Wakisaka, “Proposal of a Gas Parcel Method for Improving the Accuracy of Gas Jet Analysis in a Gas Fuel Injection Engine”, Journal of the JIME Vol.42, No.4 (2007)
- [113] J. K. Ducowicz, “A particle-fluid numerical model for liquid sprays”, Journal of Computational Physics, vol. 35, pp. 229-253.
- [114] A. D. Gosman, R.J.R. Johns, “Computer analysis of fuel-air mixing in direct injection engines”, SAE Paper 800091
- [115] R. D. Reitz, “Modelling atomisation processes in high-pressure vaporising sprays”, Atomisation and Spray Technology, Vol. 3, pp. 309-337
- [116] J. C. Dent, “A basis for comparison of various experimental methods for studying spray penetration”, SAE paper 710371